A Nuclear Magnetic Resonance Investigation of Brine Inclusions in Antarctic and Artificial Sea Ice

A thesis submitted in partial fulfilment of the requirements for the degree of Master of Science in Physics at Massey University

Suzanne Alice Furkert

2000

Acknowledgments

I would like to thank every body I have worked with over the last two years. I could not wish for a better group of people, so many of you have become great friends with whom I have had many laughs, good times and experiences. Your moral support and advise has made the last couple of years truly memorable.

Special thanks must firstly go to Paul Callaghan my supervisor. He gave me a wonderfully interesting project with unique opportunities I could only have dreamed of. I feel privileged to have worked with somebody with such undying energy, enthusiasm, patience, and brilliant ideas when I had none.

I cannot imagine having completed this Masters without Robin and Ethan. Not only have they given me unmeasurable help with my work, but they have also become my dearest friends. Thank you for sharing your knowledge, and for all the great times we have shared together.

I would like to thank Barry, Steve, and Noel, from the Mechanical Workshop who taught me so much, and without whose help my masters would have been impossible. Also Udo, Peter, and Keith, from the Electronics Workshop for their expertise and valuable discussions.

I would also like to thank my parents Annette and Rod, who have always offered great encouragement and support in many forms. Especially Dads' marathon proof reading effort.

Contents

Abstract

The aim of this thesis is to use Nuclear Magnetic Resonance (NMR) techniques to examine the brine pockets in sea ice. Both the movement of the brine pockets within the ice, and the movement of the brine within the brine pockets is examined. The experiments are carried out using Earth's field NMR on sea ice in situ in Antarctica, and high field NMR equipment on artificially grown sea ice in New Zealand. The field work involved probe design, construction, and use. Investigations were carried out on brine content, and brine diffusion rates. The laboratory work involved growing realistic artificial sea ice, designing and constructing a temperature control system for the high field NMR machine, and carrying out experiments on the artificial sea ice samples. The brine pockets' morphology and distribution was examined. The brine and brine pocket movements over time, with a controlled temperature gradient, were also investigated. The results from the field work clearly showed multiple diffusion rates in sea ice, both faster and slower than that of water. The lab work showed that realistic sea ice had been grown, and that there was a migration of brine pockets in the direction of the temperature gradient.

Preface

This thesis investigates the properties of brine inclusions in sea ice. It is comprised of two parts, one part involved field work using Earth's field Nuclear Magnetic Resonance (NMR), on in situ sea ice in Antarctica. The other part was laboratory work carried out on artificial sea ice with a high field NMR machine in New Zealand.

Previous work done in 1995 and 1997 indicated that there was a brine diffusion rate in the sea ice faster than that of free water, however, the ice sampled was significantly disturbed in the course of the experiment. The probe that was used in 1997 was placed over, and sampled, an ice core that was connected at the base to the ice sheet. However, a large amount of ice around the ice core had to be removed to allow for the probe's gradient coils to be placed over it. The field work component of this thesis involved improving the probe used in 1997 to incorporate the gradient coils into the probe head. This alleviated the need to remove extra ice from around the core being sampled, and therefore caused less sample disturbance and allowed more cores to be examined due to the reduction in time required to set up the equipment. In order to incorporate the gradient coils, the field profiles of the gradient coil and the sensitivity profile of the transmit/receive coil had to be determined. This enabled us to choose the best gradient coil, configuration, position, and number of turns, taking into account the physical constraints imposed by the pre-existing probe head and drilling equipment. Software had to be developed to compensate for the gradient field inhomogeneities caused by the proximity of the coils to the sample. Another probe was also constructed to further reduce the disturbance to the ice sampled. This probe sampled the undisturbed region outside the probe. In order to do this however, the signal from the ice had to be received from outside the coils, causing a reduction in signal strength.

The lab work was designed to complement and extend the field work. Much larger signals were obtainable with the high field NMR system, enabling precise imaging and diffusion measurements to be made. The lab work undertaken involved growing

realistic artificial sea ice, designing and constructing a temperature and temperature gradient control system for both the growing of the ice, and the NMR machine, and completing imaging and diffusion experiments. Three-dimensional images were taken of the entire sample to ensure that the artificial sea ice sample created was a realistic and accurate representation of naturally formed sea ice. A series of two-dimensional images were also taken over a period of time, to track the migration of the brine pockets. Diffusion weighted images were taken to enable the diffusion rates to be accurately correlated with brine pocket morphology and migration. Sea ice has a local co-ordinate system, caused by the individual ice crystal orientation within the ice sheet. The orientation of the NMR machine axes is not necessarily aligned with the local axes, and therefore software had to be written to enable the difference in axes' orientation to be detected, and compensated for, to examine the diffusion rates in the local co-ordinate system.

Chapter 1

SEA ICE

1.1 Antarctic sea ice

The annual sea ice of the southern ocean, and its associated snow cover, play a number of important roles in the ocean atmosphere climate system, in ocean circulation and in structuring the marine ecosystem. Sea ice, which is between 1 and 2 meters thick and covers an area of approximately 20 million square kilometers in winter, greatly reduces the exchange of heat, gas, and momentum between the ocean and the atmosphere [1].

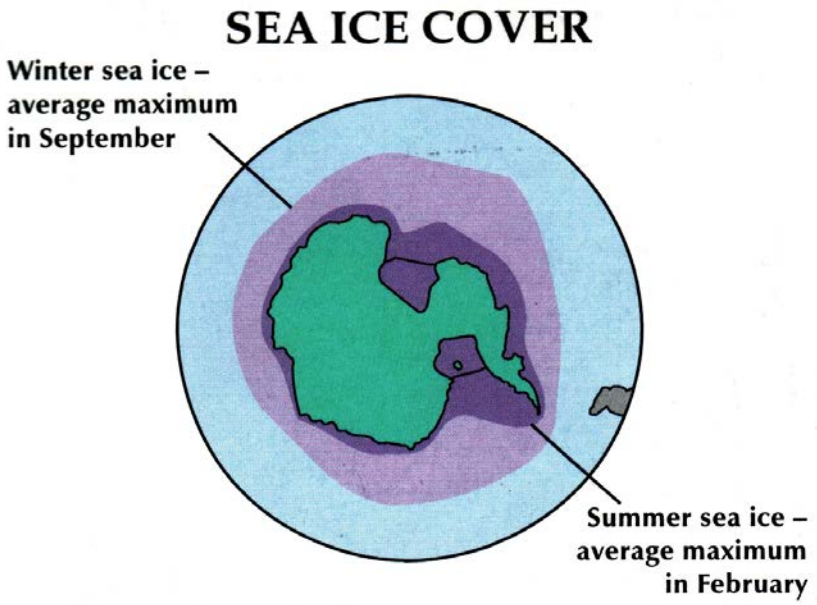

Figure 1 Antarctica, and it's seasonal ice cover.

Compared to open water, which reflects only 5% of sunlight, snow-covered ice reflects over 90% of short-wave radiation, and significantly reduces both the absorption of solar radiation at the surface, and the amount of light available for photosynthesis under the ice. The sea ice is a very effective insulator, greatly restricting the loss of heat from the relatively warm ocean (-1.9^{O}C) to the much colder polar atmosphere (which can be colder than -40^{O}C). During winter, the turbulent heat loss from leads (cracks in the sea ice that can be many kilometers long) can be two orders of magnitude greater than that from ice covered ocean [1]. In the carbon dioxide cycle, seasonal ice cover limits carbon dioxide exchange while subduction of surface water acts as a carbon dioxide sink [2]. The ice influences ocean structure and circulation, since during ice formation and growth the ice releases salt into the

underlying ocean, increasing density and inducing the formation of dense, cold, and saline Antarctic Bottom Water. This is transported northwards, setting up deep convection currents that contribute to the upwelling of nutrients and to the overall thermohaline circulation (water movement driven by salinity and temperature differences) of the global ocean. The movement of ice northwards during the summer further influences the meridional heat and freshwater transport. Melting of the sea ice releases freshwater and algae spores to the ocean, increasing stability and stimulating phytoplancton growth [2].

1.2 Sea ice crystal formation

The crystal structure of sea ice is controlled by many natural causes. For one-year-old ice, the most important of these are the conditions of ice formation, i.e. the temperature, salinity, and wind-induced mixing of water during the formation and growth of the ice.

The crystals formed by the freezing of sea water are in general more or less uniform platelets of pure ice. This is due to the water molecules forming layers of hexagonal rings upon freezing. The most important characteristic of the lattice is that there is only one principal hexagonal axis of symmetry (c-axis), which is the optic axis of the ice crystal [3]. The optic axis is perpendicular to the plane of hexagonal rings, which is called the basal plane, (see figure 2). A ray of light incident on the crystal parallel to the c-axis passes through it in the usual way, with oblique incidence birefringence taking place, which is an important factor in determining the optical and reflective properties of ice.

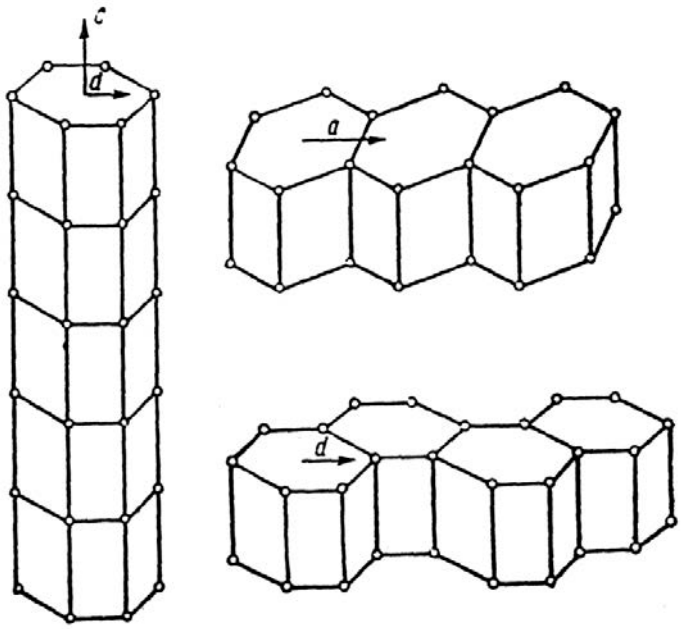

Figure 2 Formation of ice needles and plates with growth of ice crystals along different axes [3].

In the plane it is possible to distinguish two directions: the a-axis passing through the middle of one side of the hexagon and the direction inclined by 30^{O} to the a-axis, called the d-axis. The difference between the properties of ice along these two directions is small, so in the basal plane the ice is nearly isotropic. The growth of ice crystals follows the direction of these axes, if the crystal grows in the direction of the c-axis, needles are formed, if it grows in the a- or d-axis thin layers are formed. With simultaneous growth in the direction of the c- and a-axes, ice plates are formed [3]. The principal direction of growth of crystals is determined by the anisotropy of the surface energy of different faces of the ice crystal. The surface energy of the lateral faces (growth along the a- and d-axes) is substantially less than the surface energy of the tight packed plane (growth in the direction of the c-axis). Therefore the growth of the ice crystal mainly follows directions parallel to the basal plane. Crystals growing at the lower surface of the ice are deprived of one degree of freedom of growth (lateral) and further increases in size are determined by the law of geometrical selections. With vertical growth therefore, there will be a majority of crystals whose basal planes are oriented vertically and optic axis horizontally. Crystals with a disadvantageously oriented optic axis will be rapidly absorbed by their growing neighbours and cut off from the water, this is called individual suppression of cells.

In the case of lateral growth, a crystal with its basal plane disposed horizontally will prevail [4].

The chief characteristic of the crystal structure of sea ice, as compared to fresh-water ice, is the small size of the crystals. This is explained by the fact that the ions of all the salts in sea water reduce the range of action of the crystallisation nuclei so that the nuclei concentration is higher [3]. The presence of liquid and solid layers between the grains hinders and retards the growth of crystals once formed, which also leads to a decrease in size. The micro-crystalline structure of sea ice substantially influences the deformation and strength of the ice cover.

Sea ice cover consists of individual grains that are formed from more-or-less uniformly orientated plates of pure ice (elemental plates) with an average thickness of 0.5-0.6 mm, separated from each other by layers containing cells with brine. The distance between neighbouring rows of cells in the crystal, measured in the c-axis direction, is called the cell spacing [3]. The macroscopic crystals of ice therefore possess a “platy” substructure which substantially influences their physio-chemical properties. Foreign inclusions and brine are mainly displaced to the inter granular boundary. However, a considerable part of the brine remains in cells between the plates but within the grains [1]. These cells have an average diameter of 0.05 mm and their lengths vary widely.

1.3 Sea ice structure

The initial freezing occurs near the surface of the seawater to produce a soup of frazil crystals [5] which freeze together to produce flat sheet nilas, or in the presence of waves, solid ice pancakes, (see figure 3). These pancakes may consolidate to produce a continuous ice sheet [6].

Figure 3 Pancake ice at the edge of the ice sheet in November 1999.

This frazil ice is formed from grains that have randomly orientated optical axes due to the turbulent mixing during formation. Once the initial layer of ice prevents the turbulent mixing of the water due to wind and waves, the overwhelming majority of crystals will have nearly horizontal optical axes (c-axis) [7]. In this case, below the transition layer the ice becomes columnar (filamentary) in structure and the crystals are considerably elongated in the direction of the heat flux. The mean grain diameter 'd' increases in proportion to the increase in distance 'z' from the top of the ice (figure 4).

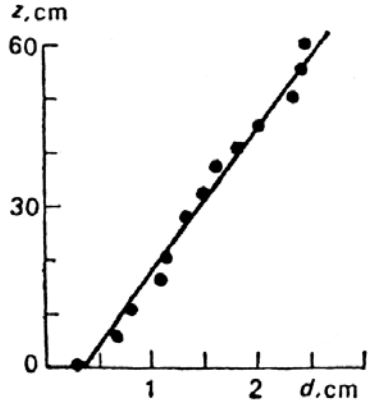

Figure 4 Mean grain size d vs distance z to upper surface of ice [3].

With the growth of the ice, the heat insulation of the zone of crystallization, i.e. the underneath of the ice, increases. The temperature gradient in that zone is therefore reduced, and so the growth of crystals is retarded but individual crystals are larger.

The cell spacing (distance between pure ice plates within the crystal) increases when the growth rate declines. Therefore, in general, the distance between the layers of cells with brine increases in proportion to any increase in the thickness of ice. The crystal structure of the ice under conditions of permanent low temperatures is very stable. The original dimensions, form and orientation of the crystals are preserved for a very long time, metamorphosis of the ice being slight. Transformations take place along the inter-crystalline surfaces and are mainly associated with the migration of brine [1].

1.4 Migration of brine

The amount of brine in sea ice depends not only on the salinity and temperature, but also on migration. Ice crystals contain very little salt, most salts are found in the space between ice crystals either in the solid or liquid state, the proportion determined by the temperature. The brine is contained in the inter crystalline layers, in capillaries and in the form of closed cells of varying form. The migration of brine takes place under the influence of a number of factors. The major factors are believed to be: the temperature gradient in the ice, affecting the concentration of brine in the cell along the direction of this gradient; the effect of gravity, facilitating the downward drainage of brine; the effect of hydrostatic pressure, squeezing out the brine from the cells; and surface tension on the brine inclusions [3].

Much of the brine that initially leaves the sea ice upon ice formation in autumn, migrates through brine channels or capillaries [8]. These can extend for many cm through the ice sheet and cause extended filamentary structures beneath the ice sheet, see figure 5. These filamentary channels are due to the brine, which has been cooled by the atmosphere, freezing the seawater around it.

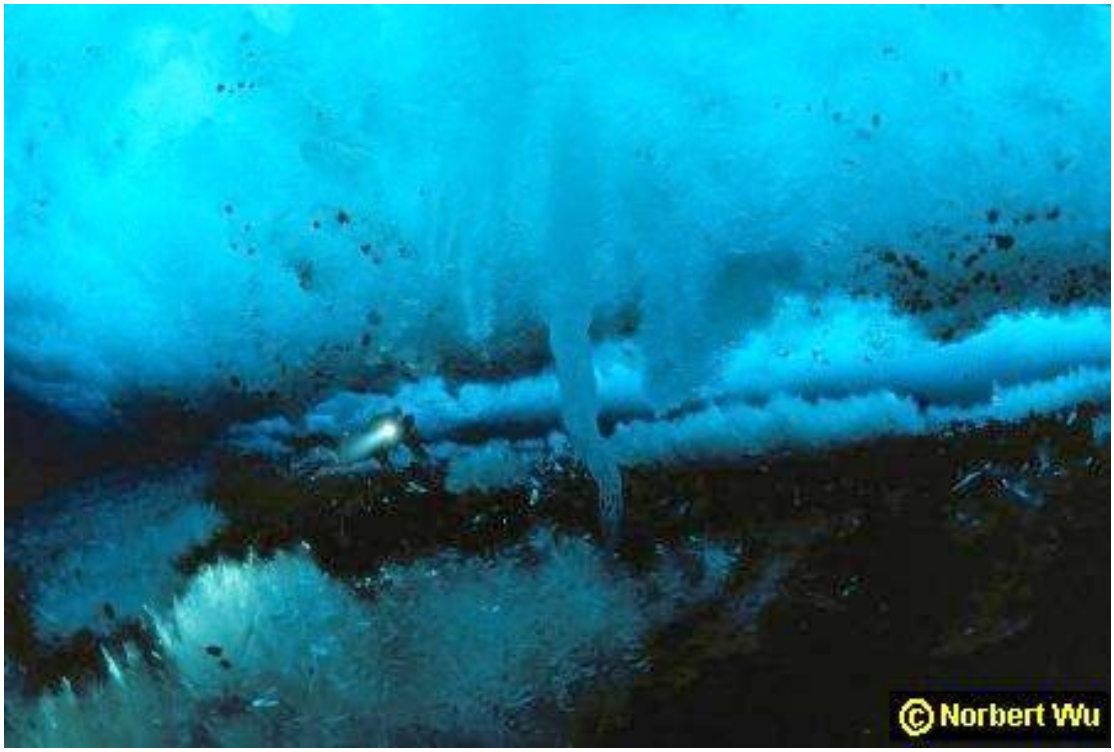

Figure 5 Brine channels extending out through the base of the ice sheet [9].

In the cold part of the year, as a result of the freezing of brine, most of the capillaries are transformed into closed cells, separated by necks of ice. Under the action of the temperature gradient these cells are displaced toward the higher temperature, in this case the ocean underneath. Since the brine in the cells is in thermodynamic equilibrium, in the zone of higher temperature (the bottom of the cell) the brine concentration is weaker than in the zone of lower temperature, (the top of the cell). As the more highly concentrated brine at the top of the cell is denser and therefore heavier, it sinks to the bottom of the cell causing the diffusion of salts within the cell [10]. This process is called Raleigh convection, (see figure 6).

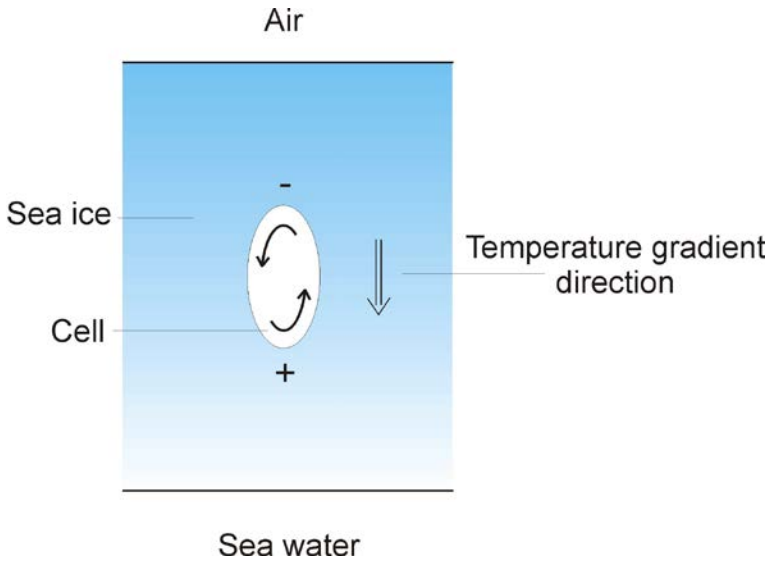

Figure 6 Raleigh convection caused by temperature gradients and gravity.

During Raleigh convection equalisation of brine concentration takes place and the temperature concentration equilibrium is disturbed. Restoration of this equilibrium requires melting of ice and dilution of brine in the part of the cell where the temperature is higher and freezing out of brine with the formation of pure ice in the zone of lower temperature. The melting of ice in the warmer part of the cell and freezing in the colder part gradually displaces the brine from the cold layers into the warmer ones until it is discharged into the water (see figure 5). The migration of the cell depends not only on the value of the temperature gradient but also on the intensity of the diffusion of salts, forces of surface tension caused by phase transitions, gravity and a number of other factors [11]. When the cells are smaller than a critical size of

40μm the surface tension is great enough to prevent Raleigh convection [12], but the diffusion of the salts will still cause migration, albeit at a reduced rate. Coalescence of individual inclusions and absorption of small inclusions by large ones also take place [13]. These transformations occur in such a way that the total surface area of the inclusions, and consequently the surface energy decreases.

For a given salinity, the amount of brine in the ice at any one time depends on the temperature. The experimental data below (figure 7) shows the decrease in brine with lowering temperature. This data is valid only when there is no migration of brine.

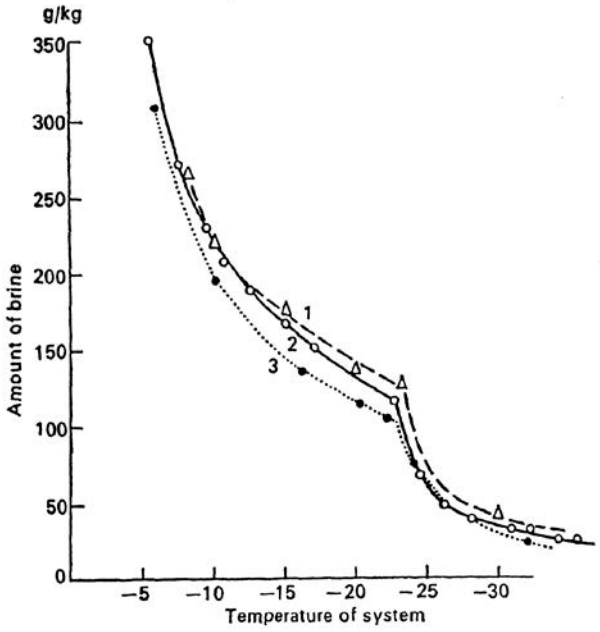

Figure 7 The mass of brine in 1kg of sea ice at different temperatures [3].
1. According to Ringer with salinity of 35.05ppt
2. According to Gitterman with salinity of 33.10ppt
3. According to Assur with salinity of 34.32ppt

The nature of the variation in the salinity of ice with time is shown in figure 8. Here both the temperature effect and the effect of drainage are represented. It can be seen that directly after the formation of ice, its salinity is reduced by almost 1/2 in two months, in winter it changes comparatively little. The transition from the winter regime of salinity to the summer regime takes place very rapidly i.e. in the course of 1-2 months.

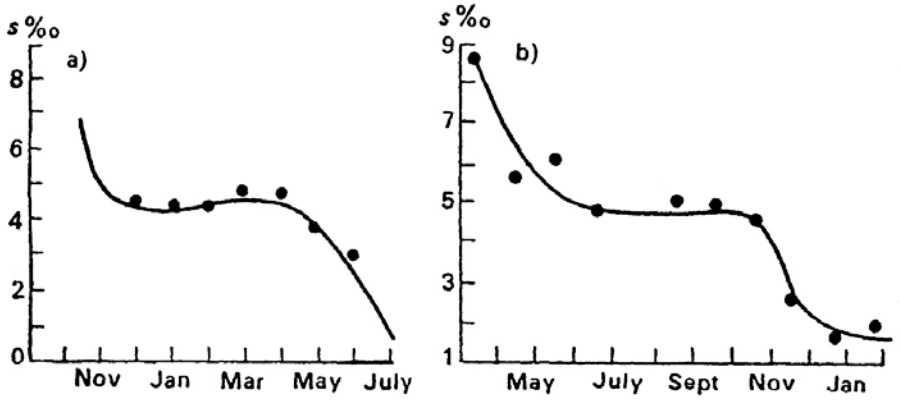

Figure 8 The change in salinity of sea ice over the winter [3].
a) In the Arctic. b) In Antarctica

After the snow cover vanishes, intense radiation melting takes place, causing pronounced structural transformations of the upper layer of the ice. Melting occurs mainly along the inter-granular layers because the brine there intensively absorbs radiant energy. When the brine freezes again a rapid growth of crystals of complex form takes place. The thickness of this intensely metamorphised layer in one-year-old ice is usually not more that 20 to 30 cm [3].

There exist a number of important differences between Antarctic and Arctic one-year-old ice. In particular, one-year-old Antarctic ice is considerably thicker at similar latitudes, than Arctic ice [14]. In the Antarctic, much of the ice consists of randomly oriented crystals characteristic of frazil ice [15, 16]. This is a result of the turbulence of the southern ocean in which pancakes are jumbled and rafted. Deep within the pack however, the open water areas become filled with ice in the Arctic manner, with ordered columnar ice forming a few centimeters below the surface [17]. It is this latter type of ice sheet which we have examined in the McMurdo Sound area. Jeffries *et al* have reported on similar structural characteristics in Arctic sea ice from the Beaufort Sea [18].

Chapter 2

NUCLEAR MAGNETIC RESONANCE

Nuclear magnetic resonance (NMR) is used in both the field, and lab work, done in this thesis. Earth's field NMR research has been done by Massey University in the past in Antarctica, this thesis carries on that work and complements it with high field NMR lab work completed in New Zealand.

2.1 Nuclear magnetic resonance theory

Nuclear Magnetic Resonance (NMR) is a technique that allows non-invasive analysis of the physical and chemical properties of materials. Nuclei of all atoms are charged and most have an intrinsic spin or angular momentum resulting in a nuclear magnetic moment. When these nuclei are placed in a magnetic field ($\boldsymbol{B}_0$), the nuclear magnetic moments will start to precess about the field, like spinning tops (figure 9) [19].

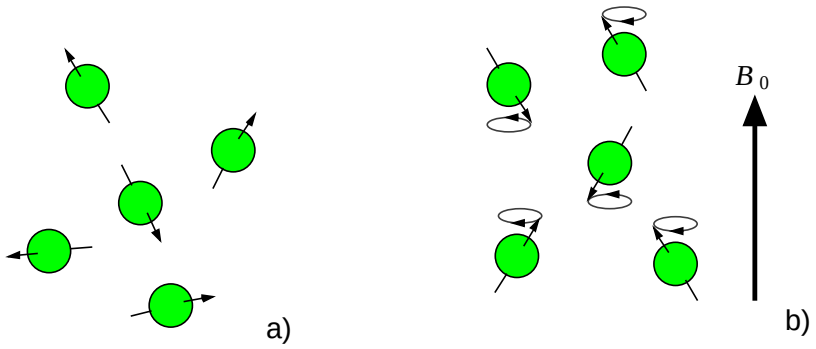

Figure 9 Nuclear magnetic moments before (a) and after (b) the application of a magnetic field.

The frequency (f) of this precession (called the Larmor frequency) depends on the type of nucleus, and the strength of the applied magnetic field $\boldsymbol{B}_0$. The equation for this relationship is:

$$f = \gamma B_0 / 2\pi \tag{1}$$

γ is the gyromagnetic ratio. For Hydrogen nuclei it is relatively high, and gives a precession frequency of 42.8 MHz/Tesla [20]. The higher the gyromagnetic ratio the better, as it allows greater signal to noise due to the increased coupling between the spinning magnetic moments and a pick up coil. The hydrogen nucleus can have two states in a magnetic field, one with its magnetic moment aligned with the field direction, and the other aligned opposite to the field direction (anti-aligned). At room temperatures there is a greater number of aligned nuclei than anti-aligned and the sum

of all the nuclear magnetic moments results in a small net magnetisation component ***M***, in the direction of the applied field, (see figure 10). The magnetisation is proportional to the applied field and sample volume.

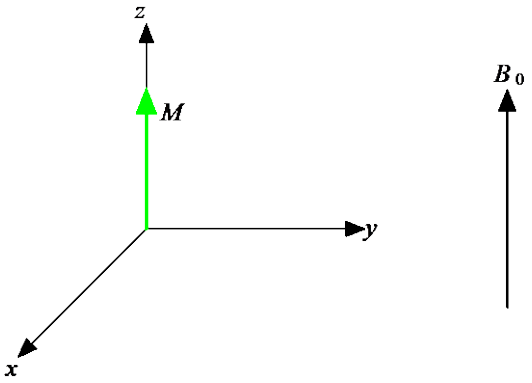

Figure 10 Net magnetisation component ***M*** aligned with the applied field $\boldsymbol{B}_0$.

In order to flip the magnetisation into the x-y plane a rotating magnetic field $\boldsymbol{B}_1$ is applied, (see figure 11). This is done using an oscillating linearly-polarised field. The oscillating field can be viewed as two counter-rotating fields, one rotating at the Larmor frequency and the other rotating in the opposite direction at the same frequency. In a frame of reference rotating with the magnetisation, the component of the $\boldsymbol{B}_1$ field rotating at the same rate will dominate and the magnetisation will follow it, rotating down into the x-y plane [19].

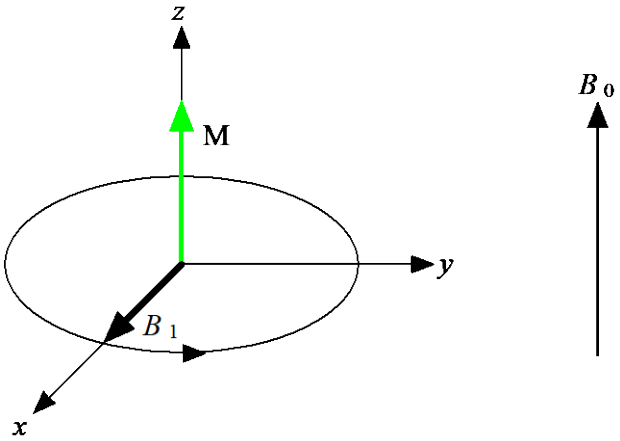

Figure 11 Rotating $\boldsymbol{B}_1$ vector produced by oscillating field.

The torque applied by the rotating field $\boldsymbol{B}_1$ causes the magnetisation vector $\boldsymbol{M}$ to spiral down around the z-axis, (see figure 12). When it reaches the x-y plane the oscillating field is removed, the precessing magnetisation can then observed as an induced EMF in the coil surrounding the sample.

The pulse needed to flip the spins is known as a 90-degree pulse [21]. The coil used to apply this pulse is often used to receive the induced signal.

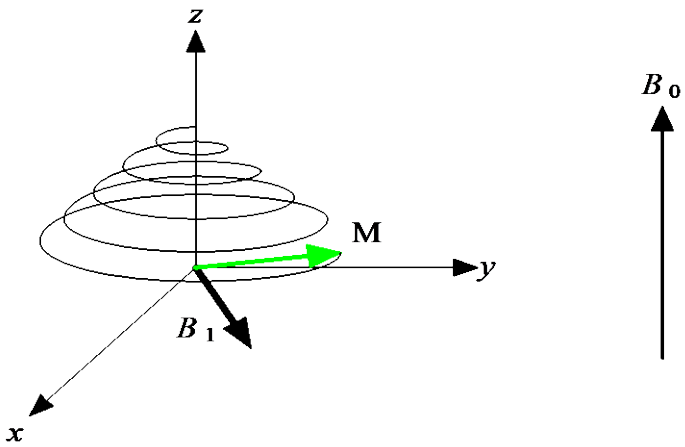

Figure 12 Magnetisation vector $\boldsymbol{M}$ spirals down into the x-y plane due to applied $\boldsymbol{B}_1$ pulse.

The induced signal does not last forever as relaxation processes will cause the magnetisation to return to it's equilibrium position, while inhomogeneities in the $\boldsymbol{B}_0$ field will cause the magnetisation to dephase (see figure 13), as not all the components will precess at the same frequency. The resultant signal is the free induction decay (FID) and consists of a superposition of decaying sinusoids, the frequency of which depend on the $\boldsymbol{B}_0$ field strength. The $\boldsymbol{B}_0$ inhomogeneities are caused by an inhomogeneous applied $\boldsymbol{B}_0$ reference field and also by the localised magnetic effects of other surrounding nuclei. The effect of the surrounding nuclei is much greater in solids than in liquids, thus enabling us to distinguish between the two phases of ice and liquid water. The signal from the ice only lasts a few microseconds whereas the signal from the liquid water can last up to a second [19].

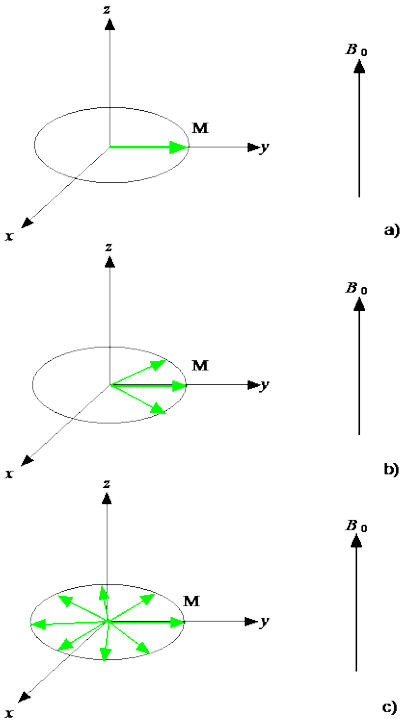

Figure 13 Dephasing of the magnetisation due to variations in the $\boldsymbol{B}_0$ field. a) is at t=0, b) and c) are after progressively longer periods of time.

The strength of the induced signal tells us about the number of nuclei present in the sample and is proportional to the sample volume. The emission spectrum tells us about the magnetic environment of the nuclei. The molecular electron orbital surrounding the Hydrogen nucleus will affect the $\boldsymbol{B}_0$ field felt by that nucleus and so its resonant frequency. This forms the basis for NMR chemical spectroscopy where the spectrum can provide information about the type of nuclei and their bonding arrangements, and therefore tell us something about the makeup of a chemical sample (see an example of a spectra, figure 14).

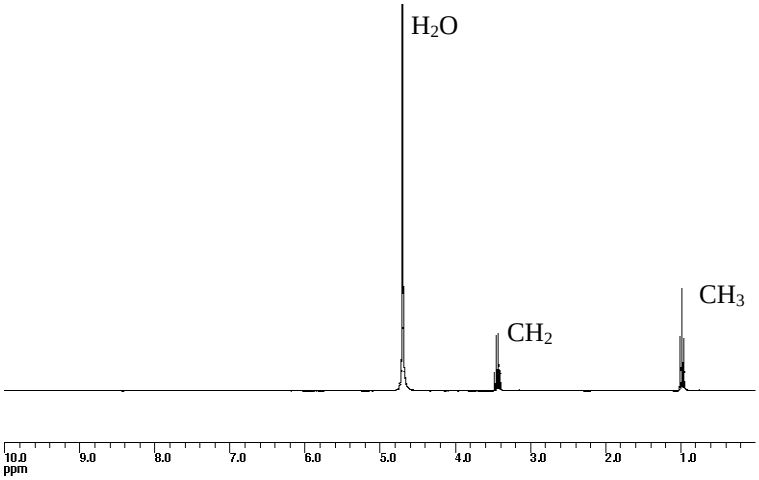

Figure 14 Spectra for a Tequila sample [22].

2.2 Determination of water content

To calculate sea ice water content, a simple experimental sequence (figure 15), consisting of a single 90-degree pulse and the observed FID is all that is required. The amplitude of the FID tells us how much liquid water is in the sample volume (see figure16).

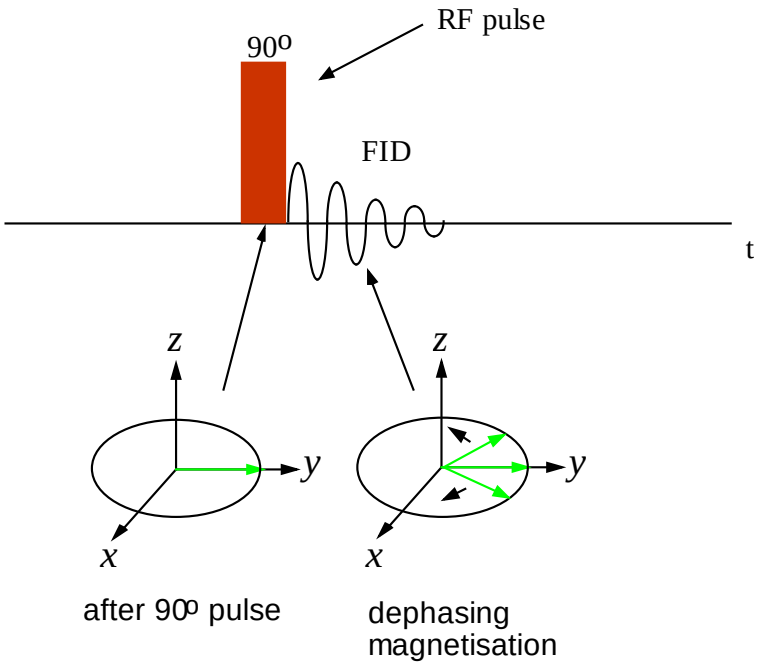

Figure 15 Simple 90 degree pulse sequence.

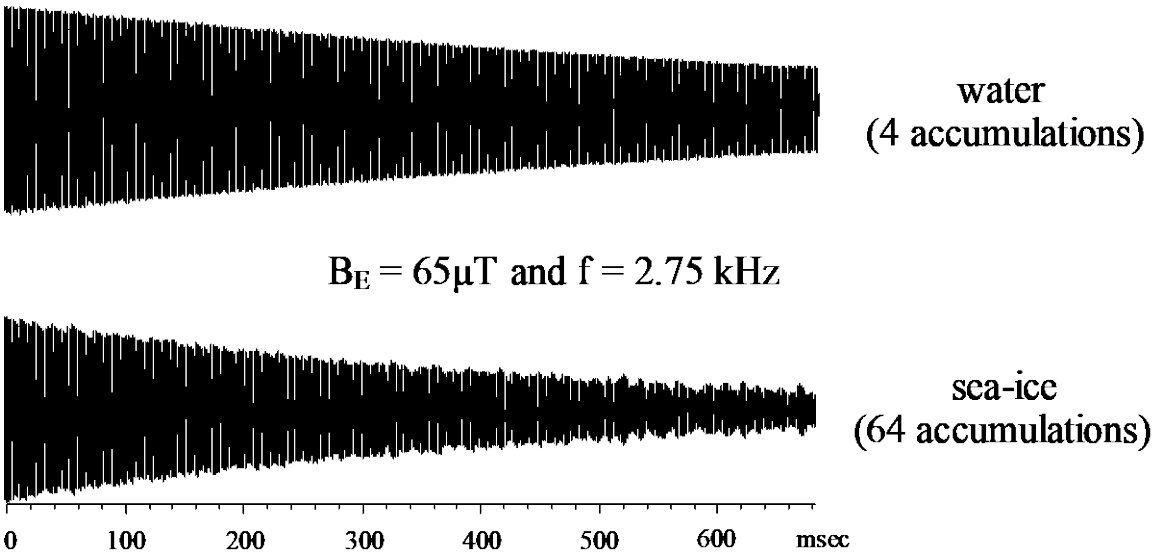

Figure 16 FID for water and ice [23].

2.3 Diffusion measurements

For the sea ice diffusion experiments, a more complicated sequence [12] is required which is based on a "spin echo" technique. In an NMR experiment the FID decay is largely due to the dephasing of the magnetisation, caused by the nuclei precessing at slightly different rates. If another RF pulse is applied a short time after the FID, so that the magnetization components are flipped over by 180 degrees, a "spin echo" will form due to the rephasing of the magnetisation (see figure17).

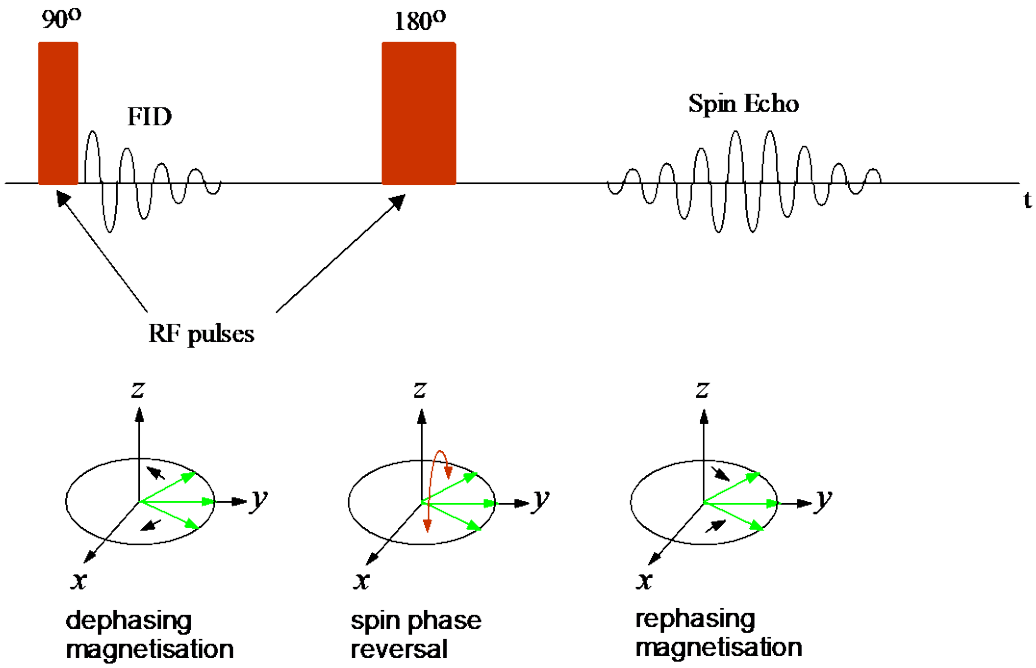

Figure 17 Spin echo formation due to the rephasing of the magnetisation.

Not all of the spins will refocus perfectly as some will experience slight changes in their magnetic environment ($\boldsymbol{B}_0$), during the time between the 90° pulse and the spin echo formation. The main cause of this reduction of the signal upon refocussing is the movement of the nuclei to different positions in an inhomogeneous $\boldsymbol{B}_0$ field and hence a change in their magnetic environment. This leads to a slight attenuation of the spin echo that is proportional to the motion of the nuclei. We can utilise and enhance this effect by applying additional magnetic field gradients which cause the spins to dephase/rephase more rapidly, and so the spin echo to show much greater attenuation with movement of the nuclei. This forms the basis for the diffusion measurements.

The experiment used to determine the diffusion coefficient is called "Pulsed Gradient Spin Echo" (PGSE) [12], and consists of the standard spin echo sequence with two additional matched gradient pulses, one on either side of the 180° RF pulse (see figure 18).

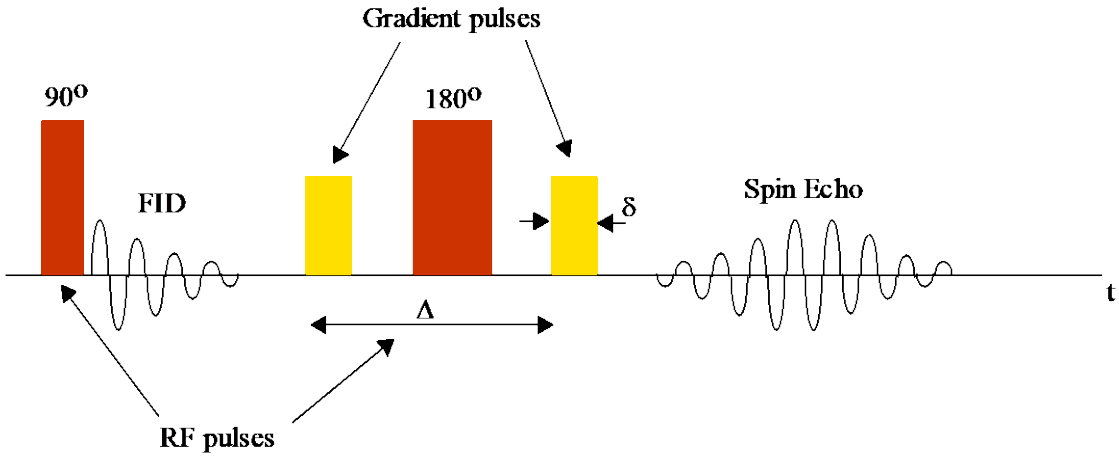

Figure 18 Diffusion measurement using pulsed gradients.

The equation which describes the relationship between the normalised spin echo amplitude, E, and the diffusion coefficient, D, is [20]:

$$E = e^{-\mathbf{g}\underline{\underline{D}}\mathbf{g}\gamma^2\delta^2\left(\Delta-\frac{1}{2}\delta\right)} \qquad (2)$$

Where Δ is the separation between two gradient pulses of duration δ and amplitude $\mathbf{g}$.

A series of experiments are performed with different gradient pulse lengths δ and a corresponding series of spin echo attenuations are obtained. The diffusion coefficient (D) is the slope of the graph of ln(E) versus $\gamma^2 g^2 \delta^2 (\Delta - \delta/2)$ (figure 19 where $g = |\mathbf{g}|$).

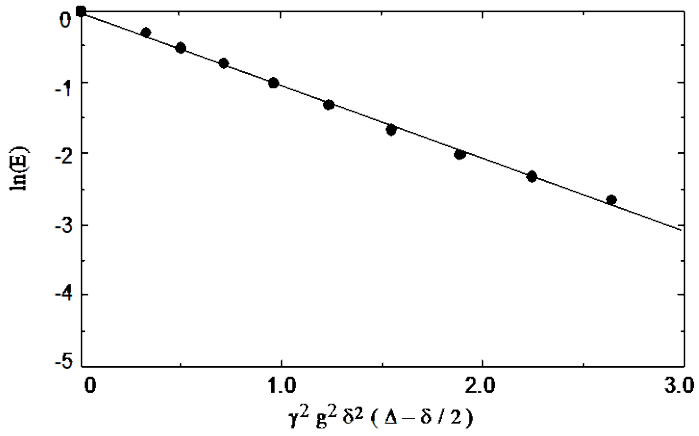

Figure 19 PGSE echo attenuation plot.

2.4 Imaging

Varying $\boldsymbol{B}_0$ with position is also used to enable images of the sample to be made. If there is a $\boldsymbol{B}_0$ field gradient then nuclei will have different Larmor frequencies and so will show up in different positions on the frequency spectrum (see figure 20) This forms the basis of NMR imaging [19]. When a combination of gradients in the x-, y-, and z-directions is used, a two- or three-dimensional image can be produced.

Reference

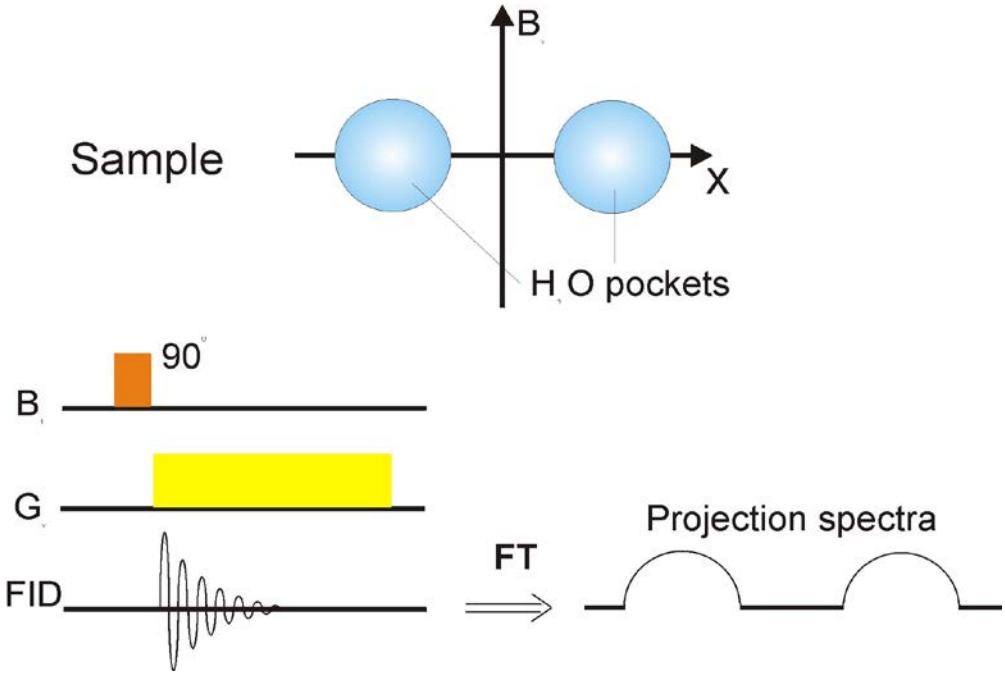

Figure 20 Example of a 1D-image.

2.5 Earth's field NMR

Nuclear magnetic resonance can also be done using the earth's magnetic field as the $\boldsymbol{B}_0$ field. The earth's magnetic field is very weak (65 μT in Antarctica [24]) and so results in a Larmor frequency of 2.76 kHz. The low magnetic field results in a very weak magnetisation, as not many of the spins will be aligned with the field. To improve the bulk magnetisation, a polarising coil is used to align the spins. This does not have to be in the same direction as the $\boldsymbol{B}_0$ field, if, when the polarising current is turned off slowly enough, the magnetisation will re-align to the $\boldsymbol{B}_0$ field direction.

Chapter 3

FIELD WORK

3.1 Advantages of field work compared to laboratory studies

An earth's field NMR system cannot achieve the precision that a laboratory-based superconducting magnet NMR system is capable of. This disadvantage is outweighed however, by the unreproducible improvement in sample quality. As sea ice is such a complex and dynamic medium, taking months to form, it is extremely difficult to reproduce accurately in a laboratory. As the structure of the ice will rapidly and irreversibly change with small changes in environmental conditions, it is also very difficult to remove, transport and store naturally formed sea ice for laboratory investigation. Due to these difficulties it has been found that earth's field NMR is a viable option. The earth's field NMR measurements can be repeated with the laboratory based high field systems using an artificial sea ice sample (for a comparative analysis) as a standard to confirm that the laboratory grown ice has similar properties to naturally grown ice. More detailed experiments can then be completed with the higher magnetic field machines.

3.1.1 The experiment site

The location where the experiments were undertaken was in McMurdo Sound in the Ross Sea. An area was chosen in the region of the Dellbridge islands. This location was chosen as it was relatively sheltered from the weather by the four surrounding islands. Being in the lee of an island prevented blowing snow which would otherwise make it impossible to work in windy conditions, we were however, more than 500m from the nearest land to avoid structural changes in the ice due to the proximity of land. The location was a sufficient distance from Scott Base and McMurdo Station to avoid electrical interference and possible ice pollution, and it was close to the flagged route out to Cape Royds, thus making for ease of access. The ice-core experiments were conducted at the field camp as done in earlier years. The inside-out NMR probe had a greater sensitivity to external electrical noise and so a position removed from the region of the electrical interference of the camp's generator had to be chosen.

The experiment positions were:

1999 Not measured, but within 1km of the 1995 camp

1995 S 77º 33.668' E 166º 22.931'

1997 S 77º 40.744' E 166º 27.069'

1999 S 77^0 40.685’ E 166^0 26.829’

Inside out probe

1999 S77^0 40.124’ E 166^0 30.067’

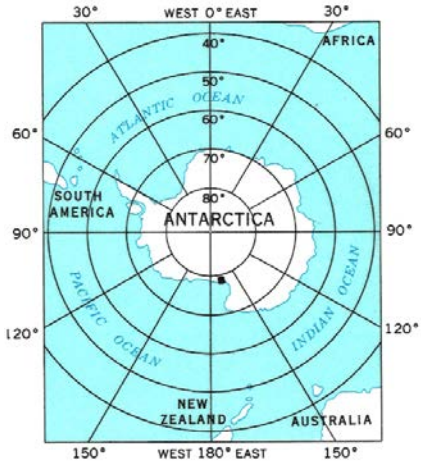

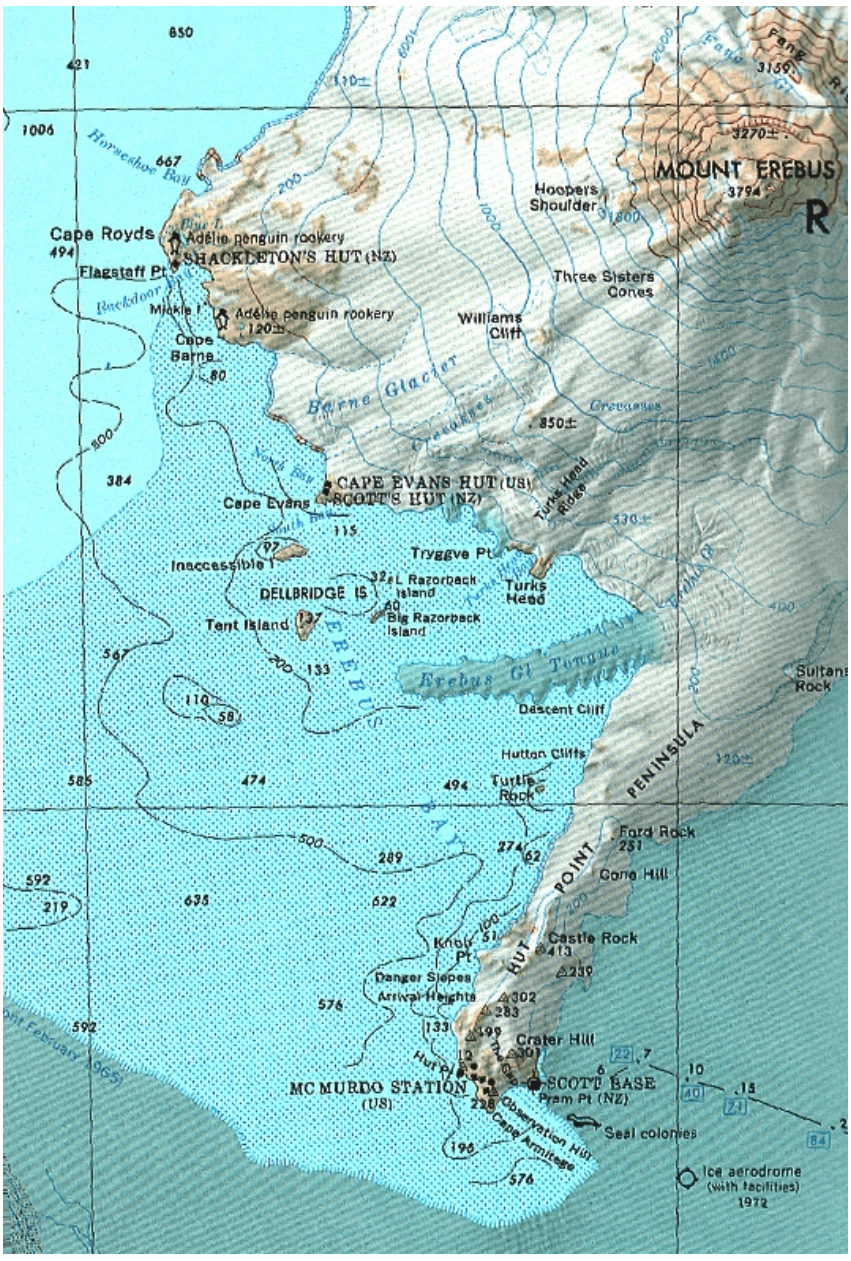

Figure 21 The position of the field camp [23]

a) Antarctica b) Erebus bay

3.1.2 Background to 1999 field work

1994 was the first year that the Massey University group went to Antarctica to carry out preliminary earth's field NMR experiments. The original system did not involve gradient coils, and was used to investigate the brine content of the sea ice, so verifying the measured brine content profile by comparison with directly measured salinity. This work also determined that the brine proton relaxation times were many milliseconds long, thus enabling future PGSE measurements of diffusion [24]. The apparatus was situated on the surface of the ice sheet and measurements were conducted on extracted ice cores (see figure 22). The B_1 excitation coil was solenoidal, thereby necessitating the measurements to be made with the ice cores extracted and placed horizontally in the NMR apparatus, to enable the B_1 field to be transverse to the Earth's magnetic field (B_0). Vertical sections could be examined, but as the bore of the probe had to remain horizontal, the extracted cores had to be sliced into 5cm-thick slices to fit vertically into the horizontal bore.

In 1995 gradient coils were incorporated into the apparatus, to enable diffusion measurements to be made. With the vertically oriented cores all the diffusion measurements exhibited bi-exponential behaviour, characteristic of at least two diffusion rates, one much faster and one slower than equilibrium Brownian motion . The data obtained from the horizontally orientated cores was much more variable, with the echo attenuations varying from mono-exponential behaviour to strongly bi-exponential behaviour similar to the vertically oriented core [25].

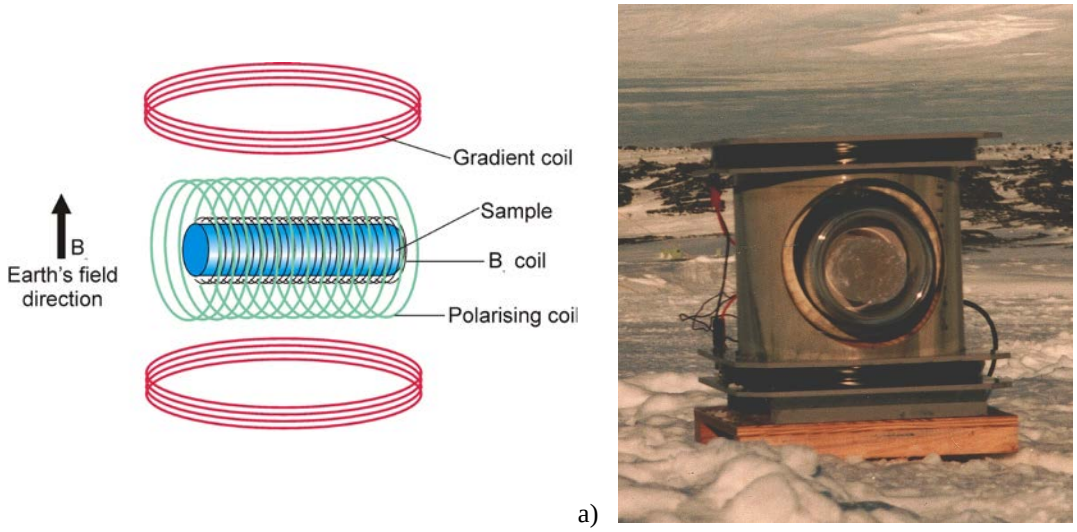

a) b)

Figure 22 The extracted core NMR probe.
a) A schematic. b) The actual appearance of the probe

There was a fundamental drawback to the above methodology. Although a good signal to noise ratio was obtained, this methodology was very structurally invasive to the sea ice sample. The ice sample changed temperature by 1 – 2^{O}C over the time taken to complete the measurements. This was due to the difference between atmospheric temperature and the temperature of the ice sheet. This could be a possible cause of the observed brine motion. In the case of the horizontal core measurements the reorientation of the core sample away from its natural alignment may disturb the hydrostatic equilibrium.

In 1997 a new system was developed to try and minimise some of these sample disturbances. The new NMR probe was designed to make measurements on in situ ice cores. A saddle coil was used for the B_1 field enabling the core to be vertically oriented in the probe, (see figure23).

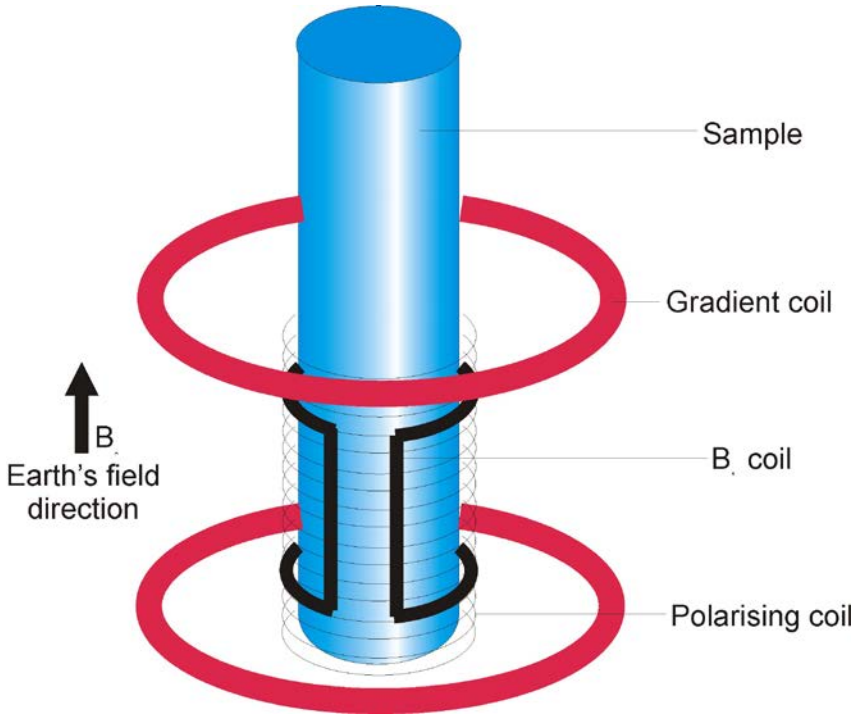

Figure 23 A schematic diagram of the 1997 probehead.

A cylindrical hole was cut down into the ice sheet, leaving an exposed core still connected to the ice sheet at the base. The probe head was placed over the ice core while it was still attached to the ice sheet. The ice surrounding the core had to be removed to create room for the gradient coils, (see figure 24). This was a major operation requiring chainsaws and ice screws to remove the unwanted sea ice, taking approximately 20 minutes per core. This meant that although the base of the core was being held at a constant temperature by the ice sheet the area that was being sampled was exposed to the atmosphere, and so losing it's original temperature gradient, for a long period of time. The time required to set up the equipment limited the number of cores examinable, and restricted the measurements to one depth that was close to the surface (the depth being the length of the chainsaw blade used). Bi-exponential decay was observed but not at values consistent with the 1995 data [12]. A possible explanation for this was the much smaller temperature gradient in the 1997 ice sheet, compared with the 1995 ice sheet.

Figure 24 The 1997 probe apparatus in use.

3.2 Changes to the 1997 probe

In 1999, the latest trip to Antarctica, the vertical bore probe used in 1997 was adapted to minimise the disturbance to the ice sample. The gradient coils, instead of being large to ensure that there was a uniform gradient over the sample volume, were reduced in size to eliminate the need for the surrounding ice to be removed with a chainsaw (see figure 25).

The advantages of this were that the time required to set up the apparatus for each experiment was greatly reduced. This enabled us to do many more experiments, and at varying depths. The disturbance to the sample was also much reduced and the surrounding ice sheet was much closer to the sample, eliminating airflow that would increase the rate of temperature change due to atmospheric cooling. Also the time that the sample was exposed to the atmosphere for, was greatly reduced.

The disadvantage of having smaller gradient coils was that the magnetic field gradient was not uniform over the sample volume. This meant that sophisticated software had to be developed to analyse the experimental results.


a)

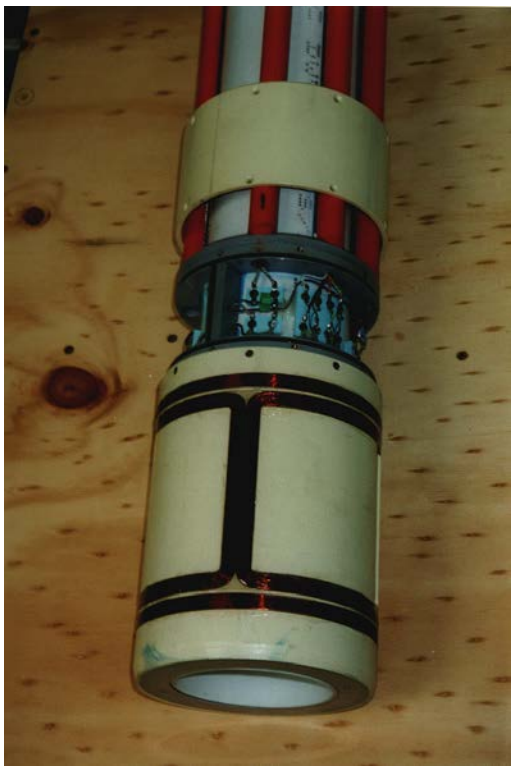
b)

Figure 25 a)The old gradient coils. b)The new gradient coils.

3.2.1 Inhomogeneous gradient field compensation

If the gradient field was homogeneous, when using a water sample we would obtain a mono-exponential decay of the NMR signal. This would produce a single diffusion peak corresponding to the diffusion rate of free water. If the gradient field is inhomogeneous the decay will be multi-exponential (faster decay from areas of high field gradient, and slower decay rates from areas where there is lower field gradient magnitude). This would result in multiple diffusion rates with the standard (homogeneous gradient field) data analysis. If however, it is known that there is only one diffusion rate (for example when using a water sample), the gradient profile can be obtained with inversion algorithms from the multi exponential decay data. This gradient profile can then be used to compensate for the field inhomogeneities and so obtain the true diffusion rates.

It is assumed that the experimental data obtained is of the form

$$\text{signal}(\delta_i) = \sum_k \mathrm{P}(D_k) \sum_j \mathrm{P}(g_j)\, e^{-\gamma^2 \delta_i^2 g_j^2 D_k (\Delta - \delta_i)} + \varepsilon_i \qquad (3)$$

Where P(D_k) are the diffusion rates and their probabilities that we wish to obtain, P(g_j) is the gradient distribution over the sample volume and ε_i is the random error (noise) of the *i*th datum.

We have a solution set Ω of diffusion rates that will fit the data closely. This set is defined by

$$\sum_i \left(\text{fit}(\delta_i) - \text{signal}(\delta_i)\right)^2 < \sum_i \varepsilon_i^2 \qquad (4)$$

Where fit(δ_i) is a curve defined by a spectrum in the set Ω.

The non-negative least squares (NNLS) algorithm [26] picks the solution set in Ω that minimises $\sum_i \left(\text{fit}(\delta_i) - \text{signal}(\delta_i)\right)^2$ and satisfies condition 1 below.

Condition 1. Non-negative condition: $\mathrm{P}(D_k) \geq 0$ for all k.

Condition 1 is to ensure that the physical condition that there are no negative diffusion rates, is met.

Used on it's own the NNLS algorithm will produce a spectrum that tends to be composed of a few isolated delta functions. The solution is strongly influenced by random error, and broad features tend to be broken into separate peaks [27] making any continuous spectrum impossible to interpret using just NNLS.

More sophisticated algorithms choose solution spectra from a reduced set Ω'. The spectra in Ω' satisfy conditions 1 and 2.

Condition 2. Expected error condition: $\sum_i \left(\text{fit}(\delta_i) - \text{signal}(\delta_i)\right)^2 \cong \sum_i \varepsilon_i^2$

The value for can by predicted from the experimental noise level.

The use of condition 2 is justified by the principle of parsimony, which states that we should chose the solution which reveals the least amount of detail that was not already known or expected. Use of this condition helps us choose a solution that has not included random noise in the signal, thus reducing artefacts and misleading bumps. The process of choosing the best solution in the set Ω' is called regularisation. There are programs developed [28 & 29] to find the smoothest of all solutions in the Ω' set. This is called regularisation with curvature constraint. These programs were used unmodified with values of regularisation parameters chosen for convenience, to give a smooth fit.

3.2.2 Coil design issues

A simple Maxwell pair [30] was used for the z (vertical) gradient and a bi-polar coil was used for the transverse gradient. The design of these coils needed to be optimised. In doing so it was necessary to consider the role of the B_1 saddle coil used to excite the spins and receive the NMR signal, since the characteristics of this coil would determine what weighting would be given to each part of the sample. To do this I needed to write computer modelling programs, that would determine the gradient magnitude and direction as a function of position within the sample, and the sensitivity of the B_1 saddle coil as a function of position [31]. The change in sensitivity of the B_1 saddle coil over the sample volume will determine the effect of the gradient field inhomogeneities (see figure 26). For example, if the signal was only observed from a small region in the centre of the sample where there was a linear gradient field the effect of the nonlinearities near the edge of the sample would be insignificant.

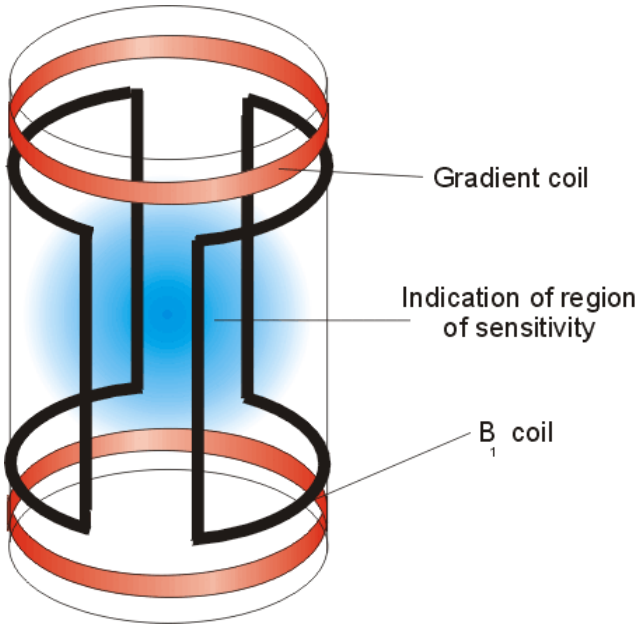

Figure 26 The region of sensitivity due to the B_1 saddle coil.

Sensitivity – B_1 saddle coil analysis

The induced signal in the coil, is the sum over the sample, of the tipped magnetisation multiplied by the B_1 field at each point. The tipped magnetisation depends on the B_1 field as it is not homogenous over the entire sample volume. The magnetisation will be reduced due to variations in initial tip angle (ie not 90^O at all points), and different phases across the sample [32] (see figure 27).

$$\begin{aligned} emf &= \sum_{sample} (\mathbf{B}_1 \bullet \mathbf{M}) \\ &= \sum_{sample} (\mathbf{B}_1 \bullet \mathbf{M}(\mathbf{B}_1)) \end{aligned} \tag{5}$$

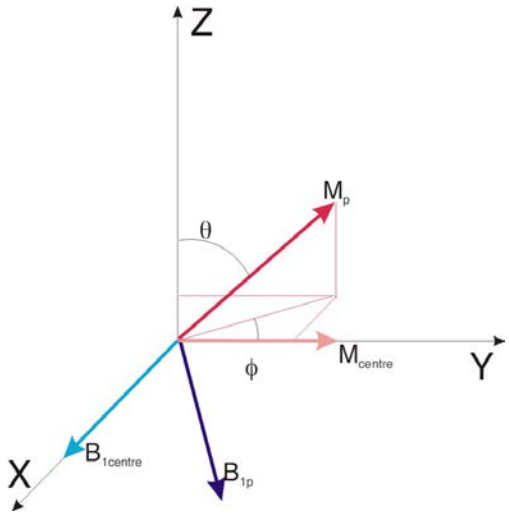

Figure 27 The resulting magnetisation (M_p) from the B_1 field at a point p.

The magnetisation of the sample precesses at a rate of $\omega = \gamma B_O$, in the earth's magnetic field (B_O). The B_1 field, which is an oscillatory field applied transverse to the B_O field, rotates the magnetisation in a vertical plane at a rate of $\omega = \gamma B_1$. As we only want the magnetisation tipped by 90^O we only leave the B_1 field on for a period of time such that in the centre of the sample the dipoles are flipped exactly 90^O.

$$\begin{aligned} \sin\left(\gamma B_1 t_{\text{for } 90^o}\right) &= 1 \qquad \text{at centre} \\ \text{Flippedness} &= \sin\left(\frac{B_1}{B_{1\text{centre}}} \times 90^o\right) \qquad \text{at any point in the sample} \\ \Rightarrow \theta &= \left(\frac{\sqrt{B_{1x}^2 + B_{1y}^2}}{B_{1\text{centre}}} 90^o\right) \qquad \text{for any point} \end{aligned} \tag{6}$$

Thus the reduction in sensitivity due to tip angle (θ) at any point within the sample volume, is sin θ (see figure 27).

B_1 inhomogeneities cause a reduction in the bulk magnetisation [19]. This is a consequence of the direction of the position on the x-y plane (ie the phase) that the magnetisation will be flipped to. If we assume that the B_1 field is totally in the x direction in the centre of the sample volume (the coordinate system is chosen to ensure this), the magnetisation in the centre of the sample will be purely in the y direction. If at other points in the sample there is a y component of the B_1 field then the magnetisation in the y direction will be reduced, and there will be a x component of magnetisation. On average, over the whole sample the x components will cancel out.

The angle on the x-y plane that the magnetisation is rotated by is given by ϕ (see figure 27).

$$\phi = \tan^{-1}\left(\frac{B_{1y}}{B_{1x}}\right) \tag{7}$$

Therefore the reduction in sensitivity due to ϕ is $\cos\phi$ at any point in the sample.

The magnetisation at any point in the sample is therefore:

$$\mathrm{M} = \left|\mathbf{M}_O\right| \times \sin\theta \times \cos\phi \tag{8}$$

The normalised field at any point within the sample is:

$$\frac{\sqrt{B_{1x}^2 + B_{1y}^2}}{B_{1centre}} \tag{9}$$

This leads to the induced emf being:

$$emf = \sum_{sample} \left(\frac{\sqrt{B_{1x}^2 + B_{1y}^2}}{B_{1centre}} \times \left|\mathbf{M}_O\right| \times \sin\theta \times \cos\phi \right) \tag{11}$$

Maxwell Pair – Z gradient analysis

A Maxwell pair is a coil configuration designed to give a uniform gradient field over the largest possible volume [33]. It is formed by two coils oriented as shown below in figure 28.

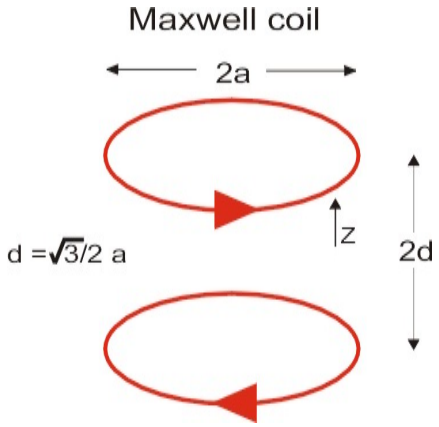

Figure 28 A Maxwell pair and its relative dimensions.

The old gradient coils had a diameter of 0.352m, and a magnetic field gradient in the centre of 5 x 10^{-3} T/m.

The magnetic field along the centre of a Maxwell pair is given by [30]:

$$B_z = \frac{\mu_o I R^2}{2\left(R^2 + (Z-\mathrm{d})^2\right)^{3/2}} - \frac{\mu_o I R^2}{2\left(R^2 + (Z+\mathrm{d})^2\right)^{3/2}} \qquad (11)$$

where B_z = the field in the centre of the coil along the z-axis.

Z = the distance vertically from the centre of the coil.

The new smaller gradient coils had a diameter of 0.14m (the diameter of the probe head) and so a height of 0.12m. To determine the number of ampere turns required to create the same gradient in the centre as the original gradient coils, we let the B_z field equal 5x10^{-2}mT at z=1cm above the centre (giving a field gradient of 5 x 10^{-3} T/m). Substituting the values for height and diameter of the new coil, we used the above equation to determine that there needed to be 61.4 ampere turns in the coil.

3.2.3 Computer B_1 and Z-gradient field modelling

The B_1 saddle coil

This coil was modelled in eight sections, (the four vertical wires and the four curves connecting them) The effect from each wire was determined at all points in the sample volume, and then the results were combined to deduce the magnitude and direction of the B_1 field at all points in the sample from the entire saddle coil.

Each section of wire was split into many smaller parts and the Bio-Savart law was used to determine the effect from each part within the sample volume. The Bio-Savart law is [34]:

$$\mathbf{dB} = \frac{\mu_o I}{4\pi} \frac{\mathbf{dl} \wedge \mathbf{r}}{|\underline{r}|^2}$$
$$\Rightarrow \mathbf{dB} = \frac{\mu_o I}{4\pi} \sum_{sample} \frac{\mathbf{dl} \wedge \mathbf{r}}{|\underline{r}|^2} \qquad (12)$$

Where dl is the element of wire being investigated, **r** is the vector between the element of wire and the point in the sample being examined and $|\underline{r}|$ is the magnitude of the **r** vector.

The sample volume was described in three dimensions with the centre of the sample being the origin, see figure 29.

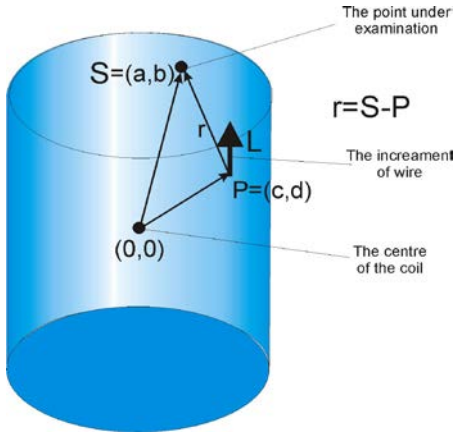

Figure 29 Where vector 'r' comes from.

A program called crossprod takes the cross product between L (the vector describing the wire element) and r (see figure 29 above). This is used in a program called Bplane, which determines the B_1 field in the x, y, and z directions, at all points in a x–y plane for a given wire element (see figure 30). This information is saved in matrices B_x, B_y, and B_z. This is repeated for every wire element (n) of the sample, the B_x etc, matrices are added together and saved into matrices BX, BY, and BZ respectively. This is then repeated for every increment of height (m). The results from each value of m are stored in matrices called BXm, BYm, and BZm, which consist of the BX, BY, BZ matrices that describe the x–y plane stacked on top of each other.

For example:

$$BXm = \begin{bmatrix} [BX_{ij}]_{(n=1)} \\ [BX_{ij}]_{(n=2)} \\ \vdots \\ [BX_{ij}]_{(n=n)} \end{bmatrix} \qquad (13)$$

The BXm, BYm, and BZm matrices for the eight different parts of the coil were combined and the resultant matrices were called BXM, BYM, and BZM.

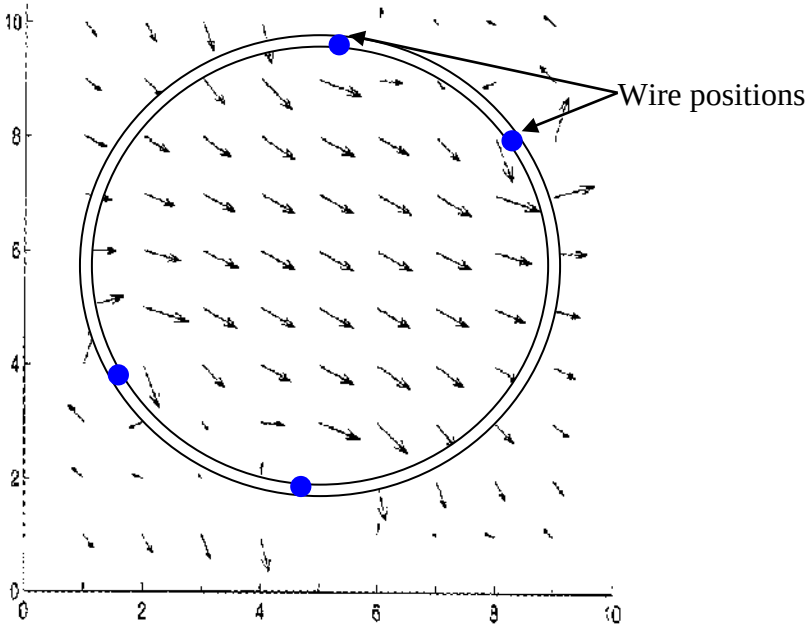

Figure 30 An example of a quiver plot, showing field direction and magnitude in the x–y plane in the B_1 saddle coil, through the centre of the sample volume.

The field at the points where the wires were, and outside the coil, were made to be equal to zero as there would be no sample there. The final part of this program was called recsignal and, using the BXM, BYM, and BZM matrices and the earlier formula for sensitivity reduction, determined the amount of received signal from every part of the sample.

The Maxwell gradient coil

The program written to model the gradient coils was just a simpler version of the B_1 coil program. Instead of having eight parts it just had two parts, the top and bottom of the coil.

The gradient field multiplied by the sensitivity at all points produced the gradient profile needed to compensate for the gradient field inhomogeneities (see figure 31).

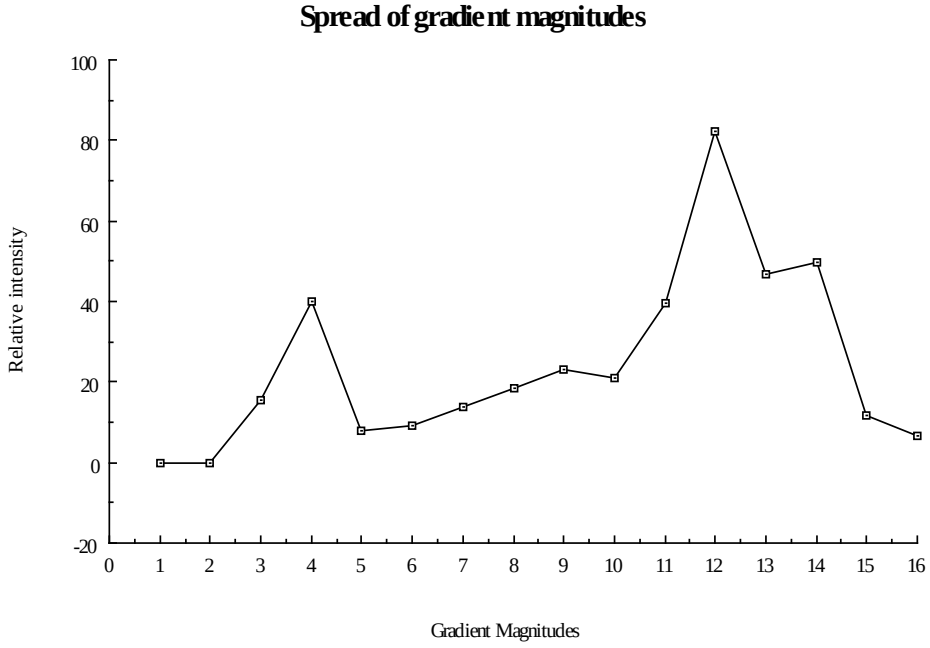

Figure 31 The spread of gradient magnitudes multiplied by the sensitivity, over the sample volume.

The actual Matlab [35] programs written for the B_1 saddle coil and the gradient Maxwell coil, are in Appendix 1.

3.2.4 Transverse-gradient coil configurations

The original gradient coils that were used in 1995 and 1997 were not physically connected to the probehead, and could simply be rotated 90^{O} to convert from vertical-gradient to transverse-gradient coils. The new compact vertical-gradient coils are however, wound directly onto the probehead itself and so cannot be rotated for a transverse gradient.

Transverse-gradient coils therefore needed to be wound separately from the vertical-gradient coils, onto the probehead. In order to determine the best possible configuration for the transverse-gradient coils I used computer modelling of several different coil configurations to determine the configuration with the best gradient field.

The coil configurations that I modelled are as shown in figure 32 (the Maxwell coil is for comparison):

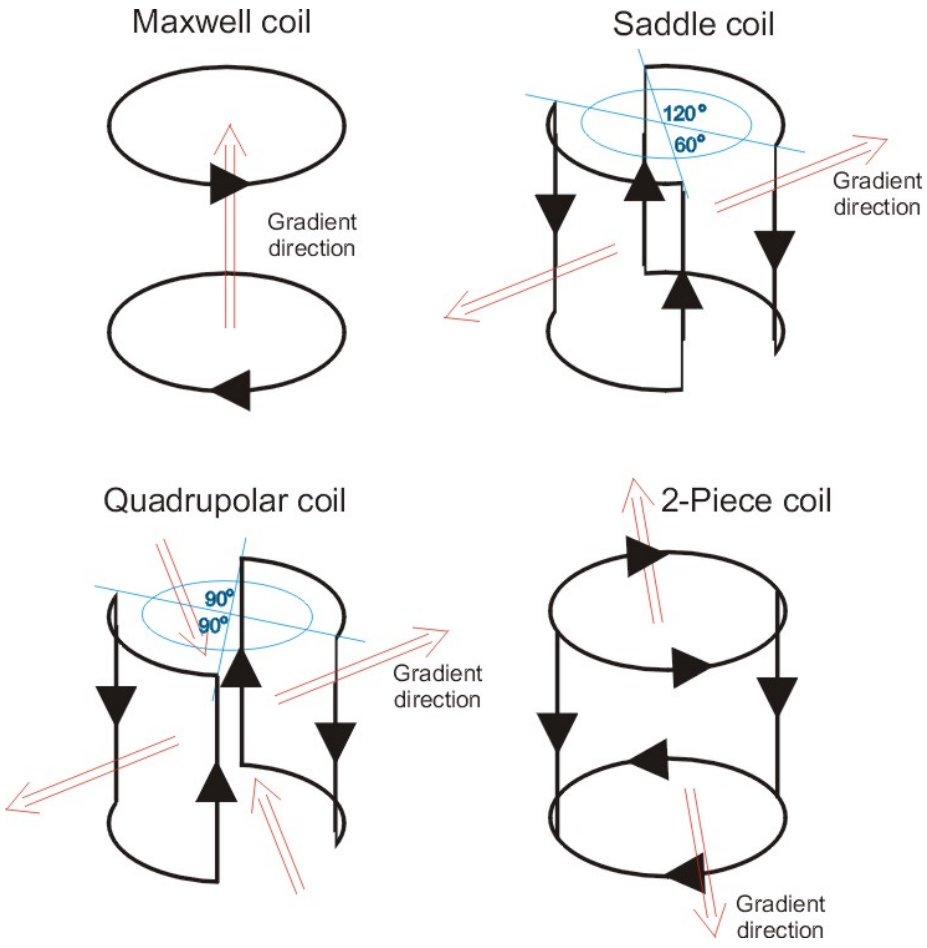

Figure 32 The modelled coil configurations

The computer modelling for these coils was very similar to the method described above in section 3.2.2 except that, in order to evaluate them comparatively, I summed the values for the sensitivity determined for the B_1 coil, multiplied by the magnetic field gradient at all points, to obtain a overall indication of each coil's effectiveness. The result of this summation was proportional to the average gradient $\overline{Gx}$ etc. The optimal coil was the one with the largest x-direction gradient, and the smallest z- and y-direction gradients.

The results I obtained at one ampere turn for the coils are given below:

Maxwell pair

$\overline{Gx} \propto 1.5 \times 10^{-2}$

$\overline{Gy} \propto 1.7 \times 10^{-2}$

$\overline{Gz} \propto 7.9 \times 10^{-2}$

Saddle coil

$\overline{Gx} \propto 1.3 \times 10^{-2}$

$\overline{Gy} \propto 2.0 \times 10^{-2}$

$\overline{Gz} \propto 5.7 \times 10^{-2}$

Quadrupolar coil

$\overline{Gx} \propto 1.8 \times 10^{-2}$

$\overline{Gy} \propto 1.3 \times 10^{-2}$

$\overline{Gz} \propto 3.6 \times 10^{-2}$

2-piece coil

$\overline{Gx} \propto 1.3 \times 10^{-2}$

$\overline{Gy} \propto 3.5 \times 10^{-2}$

$\overline{Gz} \propto 3.4 \times 10^{-2}$

From these results it was clear that the 2-piece coil was the best coil configuration modelled, having the largest x-gradient and the smallest z-gradients.

3.3 ‘Inside out’ NMR probe

The probe system with the compact gradient coils greatly improved the sample quality, optimising the core sampling system. The overall design of the probe however, having an ice core as a sample, will always have the sample separated to a large degree from the ice sheet, causing temperature perturbations and the associated structural changes. To avoid this problem I designed a probe head that would sample the ice sheet around the probe rather than the ice inside the probe, this was called an inside-out NMR probe (see figure 33). As the ice being sampled was never disturbed and was continuous with the ice sheet the quality of the sample would be near perfect. The signal received from the ice however, would be greatly reduced, as the ice would be outside the coil rather than inside as in the core based systems, and so in a much less sensitive region of the coil. The larger sample volume would make up in a small way for this reduced sensitivity.

Figure 33 The inside-out probe in use in Antarctica.

3.3.1 Considerations

The inside out probe consisted of two separate legs, each containing 1/2 the coil assembly. Thus the area of sea ice where the probe had greatest sensitivity, would be between and on either side of the legs, see figure 34.

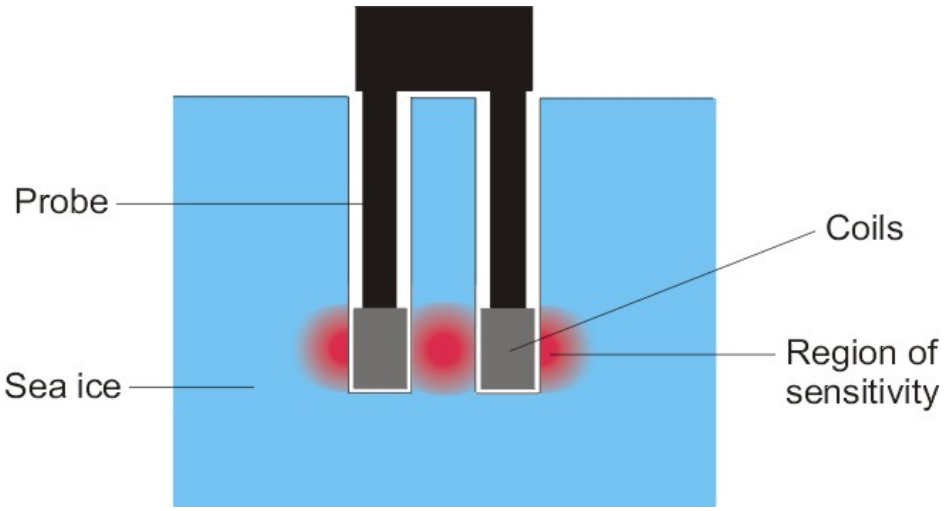

Figure 34 The region of sensitivity of the probe

The two legs had to be sufficiently far apart so that they did not affect the ice, yet as close as possible to obtain maximum sensitivity. I guessed that the optimum separation that would satisfy these conditions would be to have the legs the diameter of one leg apart.

To enable the ice to be sampled at different depths the probe had to be able to be moved vertically within the ice sheet with the individual legs retaining their original orientation and rigidity.

The external diameter of each leg was determined by the available core-boring device. The B_1 coil was the maximum size that would fit inside an outer cover of that diameter. As the sample region would be on both sides of the legs there would have been no benefit in moving the coils closer together, and so reducing their size.
The most efficient B_1 coil design is solenoidal, thus resulting in a field direction perpendicular to B_O. The polarising coils, solenoidal for maximum strength, were wound so that the field direction was in the same direction as the B_1 field, and perpendicular to the B_O field (see figure35). This coil orientation was as a result of

the field between two end-on coils being much greater than the field between two coils vertically side by side. These coils were wound inside the B_1 coils and were as large as possible. The number of turns was determined by the power available and the size constraints of the probe.

The gradient coils were in a saddle coil formation, with half the saddle in each probe leg. This design was chosen to have a resulting field gradient in the vertical direction, as the increased diffusion rate that we were hoping to observe was in the vertical direction.

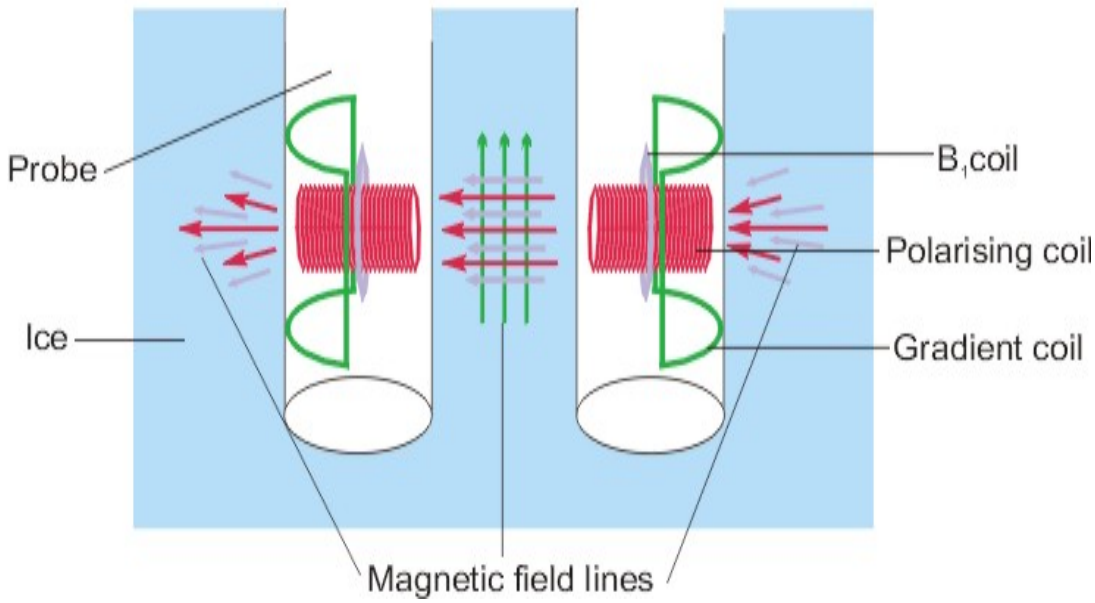

Figure 35 Coil positions and the resulting field lines

3.3.2 Coil modelling and design

The computer programs used for modelling the coil configurations and determining the resulting magnetic field strengths and directions, and so signal magnitudes, were the same format, and used the same methodology, as the modelling programs for the old probe described in section 3.2.2. All the modelling done was for one ampere turn. The area modelled was much larger for the inside out probe, both the area between the legs and the area around and between the legs was modelled and compared to the results for the old probe, see figure 36.

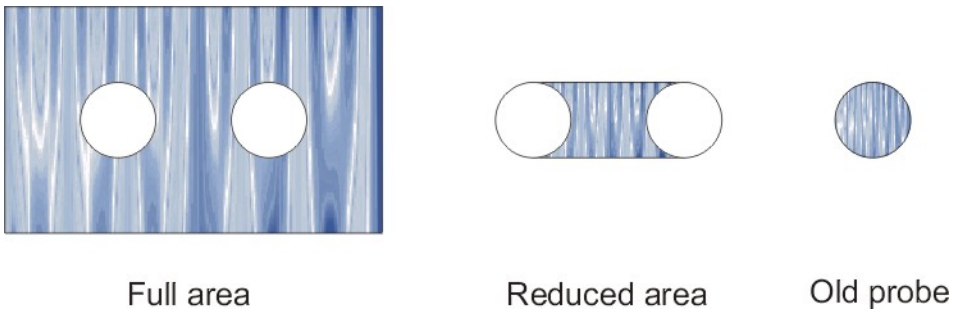

Figure 36 The area of sea ice in which the coils effects were determined.

The polarising coils were not modelled for either probe. The polarising coils were wound around the B_1 saddle coil in the old probe, and were significantly long so that the reduction in field strength towards the ends of the coil would not be in the region of sensitivity. Thus there was no need to model them as they would only add a constant value to the sensitivity at all points. The increase in signal strength due to the polarising coils in the inside out probe will not be constant as all the sample volume will be outside the coil. The task of modelling these coils would be extremely difficult as the magnetic field from a volume of coil would have to be modelled rather than the field from a segment of wire. Due to the physical constraints imposed by the size of the probe legs there was only one possible coil design, so I decided that to model the polarising coils would not be a worthwhile time investment (If I had modelled them I would not have had time to make the probe before we went to Antarctica). The predicted sensitivity compared to the old probe, with more ideal polarising coils, will therefore be reduced.

The actual modelling programs written for this probe are included in Appendix 2.

3.3.3 Construction

Probe construction

The probe has to be adjustable in height, rigid in position and orientation, and relatively waterproof.

To enable the height to be adjusted, the coils were mounted on PVC pipes that were long enough to enable the coil assembly to be lowered 1.2m into the sea ice. The tops of these pipes were glued into a bracket thus preventing relative rotation of the legs, and providing a mounting position for the coil power supplies.

To hold the probe at a fixed height in the ice sheet an adjustable plate was constructed (see figure 37). This was a rigid plate with a hole for each leg and a screw that would lock the plate to the leg. The plate could be shifted to any height along the legs, thus determining the depth that the probe would be at, and also keeping the legs' positions rigid.

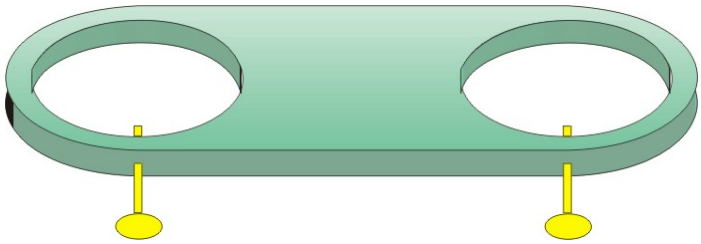

Figure 37 The adjustable plate

To seal the probe against water or saline contamination, O rings were used at the top and bottom of the sheath where it connected to the legs (see figure 38 & 40). There was also an O-ring seal around the entrance to the brace at the top of the probe that also enclosed the top of the PVC pipes.

In order to prevent heating of the ice by the energy dissipated within the coils, cold air was pumped from the top bracket through the legs and directly on to the top of the coils. The air then escaped through a valve on the top of the probe in which the air release could be controlled to create a positive pressure within the probe to further discourage water entry.

Figure 38 The inside out probe

Coil construction

Due to power supply constraints the maximum currents and voltages available were:

B_1 coil	10mA	at	10V
Gradient coil	8A	at	12V
Polarising coil	6A	at	12V

The larger the number turns there is in the B_1 coil, the greater its sensitivity will be. As resistance was not a problem I used the finest possible wire to maximise the available space. The maximum diameter of the coil was determined by the inner diameter of the probe's outer sleeve and was 100mm. The largest practical volume for the coil was $12mm^3$, the benefits of having a larger volume, and thus more turns, would be outweighed by the reduction in signal, due to then having to make the gradient and polarising coils smaller.

The gradient in the centre of the coil was calculated to be 2.25×10^{-6} T/m per ampere turn. To obtain a gradient similar to the old probes' (5×10^{-3}T/m [32]), with a current of 4A we would therefore need 543 turns. Each turn would have a length of $2\pi r + 4r$ = 0.51m (the height of the coil is 2r so 4r is 2x the height of the coil). The maximum dimension that each part of the coil can be is $15mm^2$. To fit 543 turns in this volume I would need 0.65mm diameter wire. This would then give a resistance of 14.6Ω [33]. As the available voltage is only 12V, the maximum resistance is 4.5Ω if the two sides of the coil are wired in parallel. With these resistance and volume constraints the best compromise between wire diameter and number of turns was 300 turns of 0.8mm diameter wire.

The coils were wound (see figure 39) on PVC pipe that had an external diameter of 75mm. This was the pipe that formed the legs of the probe. A nylon former was then attached to the outside of this. The former had an external diameter of 99mm and had o-rings in the top and bottom to ensure a watertight seal with the outer cover. The area between the top and bottom of the coil was removed to facilitate the placement of the B_1 and polarising coils. The windings were individually superglued on each corner then potted in crystal araldite.

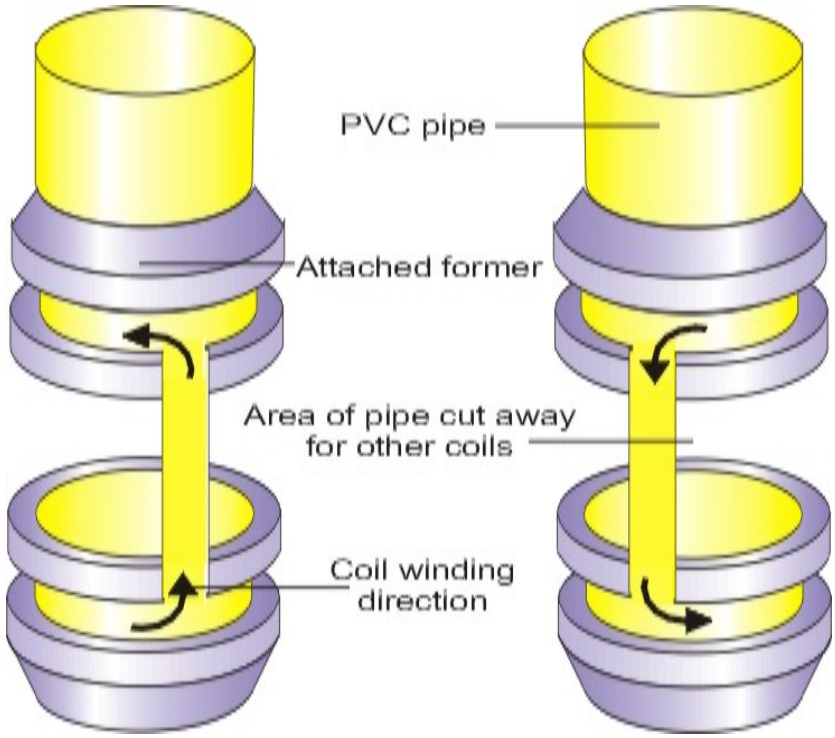

Figure 39 The former used for winding the gradient coil

The maximum dimensions for the polarising coil were a height of 60mm (the inside diameter of the B_1 coil former) and a length of 100mm. This was only the length in the centre of the coil however, as the coil had to fit into a cylinder. For coil winding purposes a cylindrical coil was necessary. The dimensions chosen were a length of 80mm and a height of 60mm. To achieve the largest possible polarising field I had to have the maximum number of turns of wire within the allowed dimensions. The number of turns possible within the above dimensions was limited by the wire resistance. Determining the length of wire, the number of turns and resistance for different thicknesses on wire, showed 1.1mm diameter wire to be the ideal choice. I wound these coils using a lathe and gluing each layer as it was wound. The ends of the former were then screwed into the outer sleeve of the probe.

Figure 40 The coils in the probe head.

3.3.4 B_1 coil sensitivity and tuning

A coil will have capacitance (C) (due to the proximity of the turns of wire) as well as resistance (R) and inductance (L), and therefore behaves as a resonant circuit [19] (see figure 41). This is called self resonance. The circuit will resonate at a frequency given by [36]:

$$f_{res} = \frac{1}{2\pi\sqrt{LC}} \tag{14}$$

The resonant frequency of the coil can be decreased by adding capacitance to the circuit. If the resonant frequency of the coil is at the Larmor frequency of the sample it will increase the signal received from the sample and reduce noise due to a reduction in bandwidth. Therefore when a coil is constructed we need to ensure that the self resonant frequency is higher than the Larmor frequency, as we can only reduce the resonant frequency.

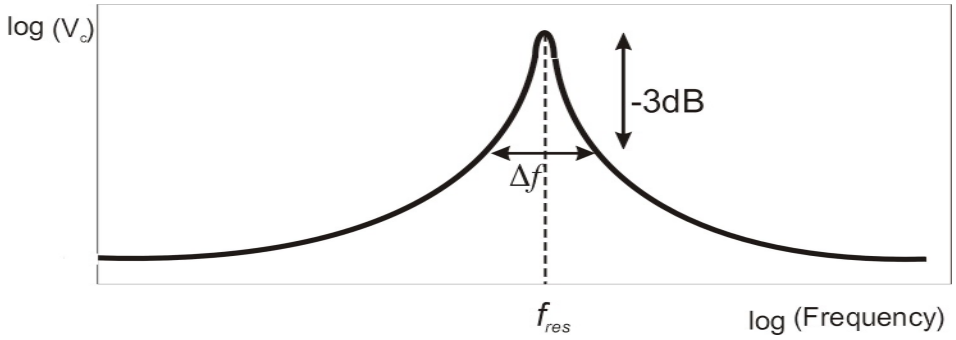

Figure 41 A typical frequency vs voltage plot for a resonant circuit.

The amount that the coil resonance will increase the signal magnitude and reduce the noise bandwidth is determined by the quality factor, Q, of the coil. The quality factor of the coil determines the width and height of the resonant frequency peak [19], and is given by:

$$Q = \frac{\omega L}{R} = \frac{f}{\Delta f} \tag{15}$$

Where Δf is the width at the –3dB points on either side of the peak.

As L is proportional to the square of the number of turns in the coil and the resistance is only proportional to the number of turns, the greater the number of turns in the coil the higher the Q factor will be.

The Q factor should no be too high however, or there might be a chance of attenuating part of the signal that is not close enough to the coil's resonant frequency. The Q factor for both probes B_1 coils however, was not high enough for this to be a problem.

The measured Q factor was 9.6 for the ice core probe and 5.4 for the inside-out probe.

In order to determine the ideal pulse length (t_{90}) for the inside-out probe we needed to determine the difference in field strength between the probes, and change the pulse length by the appropriate time.

With the ice core probe we could see the change in the signal strength from scan to scan and so could visually determine that a pulse time of 3ms was ideal. The signal from the inside-out probe was not great enough to determine the 90^0 pulse duration experimentally and so the following analysis was needed.

For the ice core probe:

Where θ = the tip angle and $\gamma = 2.675 \times 10^8$.

$$\theta = \gamma B_1 t \qquad (16)$$

When; $\theta = 90^0$

$t = 3ms$

$I = 0.19mA$

$\Rightarrow \quad B_1 = 1.96\ \mu T$

$\Rightarrow \quad B_1 = 10.5\ mT/A$

For the inside-out probe:

Wire diameter = 0.2mm

R / m = 0.549Ω

Wire length / turn = 0.298m

As coil R = 546Ω $\Rightarrow$ 1830 turns

The calculated field / turn = 2.25 μT/A $\Rightarrow B_1 = 4.12\ mT/A$

$$\Rightarrow B_{1(ice\text{-}core)} = 2.6\ B_{1(inside\text{-}out)} \qquad (17)$$

Experimental comparison:

Using a small coil driven with 0.8V peak to peak in the centre of the probes produced an output of 40mV from the ice-core probe and 15mV from the inside-out probe.

$$\Rightarrow B_{1(ice\text{-}core)} = 2.7\ B_{1(inside\text{-}out)} \qquad (18)$$

This result confirmed the calculations.

To determine the 90^0 pulse duration for the inside-out probe, we need to determine the current in the probe, and then increase the pulse duration, by the amount that the resultant field strength is less than the ice-core probe's field strength.

The same voltage was used in both probes. The value of this can be determined using Ohm's law. The Q factor of the coil must be taken into account however, as the resistance of the coil, and the current within the coil, will increase due to self resonance [39] (see figure 42).

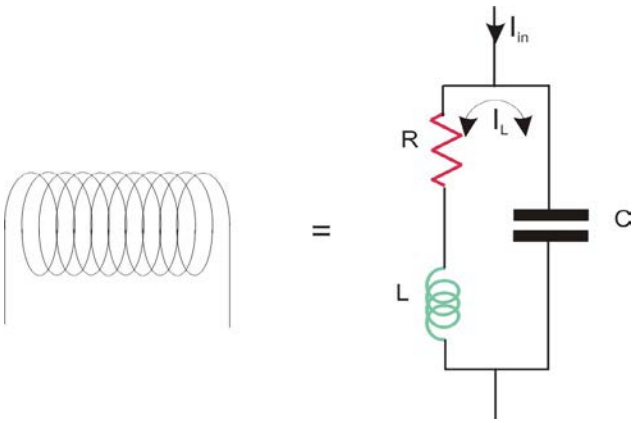

Figure 42 A resonant circuit.

The resistance of the coil at its resonant frequency (R_{res}) is:

$$R_{res} = Q^2 R \qquad (17)$$

The current within the coil (I_L) at it's resonant frequency is:

$$I_L = Q\, I_{in} \qquad (18)$$

Therefore for the ice-core probe $R_{res} = 35.9\ K\Omega$

$I_{in} = 19.4\ \mu A$

$\Rightarrow \quad V = 0.73\ V$

In the inside-out probe $R_{res} = 15.9\ K\Omega$

$\Rightarrow \quad I_{in} = 36.8\ \mu A$

$\Rightarrow \quad I_L = 0.24\ mA$

$\Rightarrow \quad B_1 = 0.97\ \mu T$

This is two times less than B_1 for the ice-core probe so the inside-out probe's 90^0 pulse duration needs to be twice as long.

$\Rightarrow \quad t_{90} = 6\ ms$

3.3.5 Alterations

Initial field trials in Antarctica did not show the expected noise reduction when the experimental site was away from the camp generator, and so the expected signal to noise ratio was not as high as had been anticipated (or hoped for).

To reduce the noise we wrapped the probe's legs in tinfoil. This was designed to reduce the capacitive coupling between the conductive ice sheet and the probe [40], the tin foil sharing a common ground with the probe.

To increase the signal strength I decided to try external polarising coils (adapted from the 1997 gradient coils). I tried two different configurations of polarising coils, one had the coils lying on top of the sea ice and the probe 200mm deep (as high as possible while still being beneath the frazil ice[6]), see figure 43b). The other having the external polarising coils vertically oriented in slots beside the probe (see figure 43a)).


a)


b)

Figure 43 The two alternative polarising coil orientations, a)with the coils vertically orientated and b) with the coils on top of the ice.

Due to unforeseen time constraints we were unable to test the probe fully in Antarctica, and as the only measurements taken were FID's, there was no chance to test the gradient coils. Further testing was carried out back in New Zealand. The site in New Zealand was at the end of Kahuterawa road in Palmerston North. This site was chosen as it was away from buildings and other sources of metal, it had no nearby power or phone lines, and it was around the bend in a small valley and so was shielded from external interference sources. The effect of nearby metallic objects disturbing the Earth's magnetic field homogeneity, can be clearly seen in figure 44, where the length of the FID is markedly reduced when a motorbike was parked nearby.

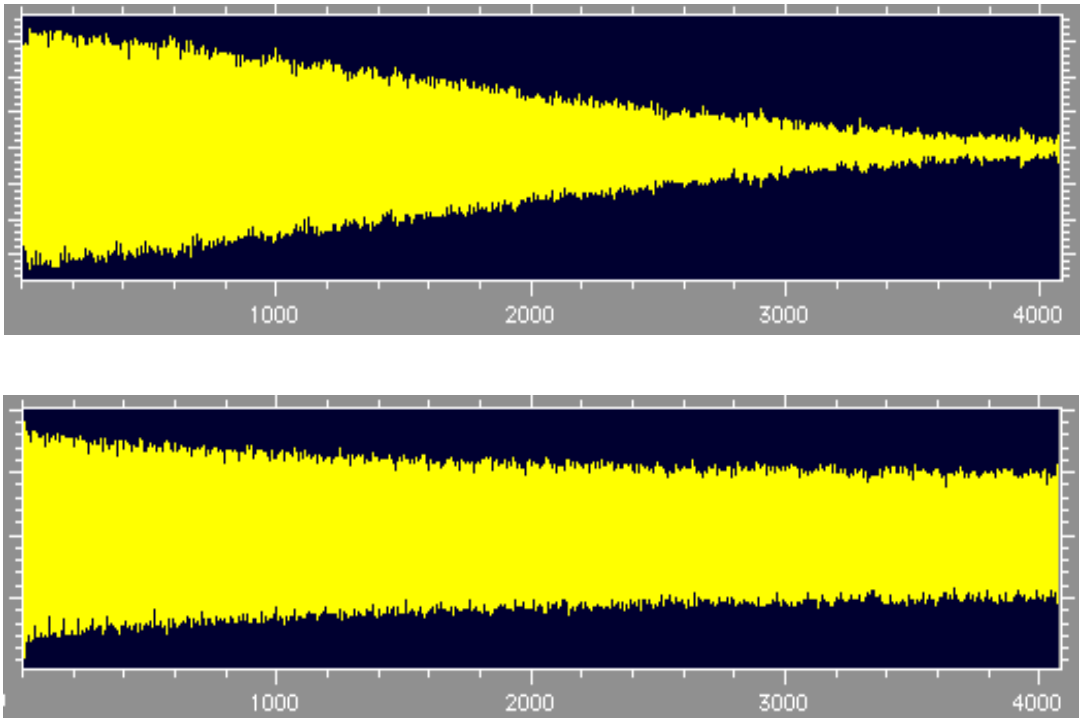

Figure 44 a) FID produced with a motorbike nearby. b) Normal FID obtained at the same site.

Tests were carried out on noise levels and on water samples using the three different polarising coil configurations that were tried in Antarctica. Tests were also carried out on the ice-core probe at the same site for comparative purposes. These results were compared with the results obtained in Antarctica.

3.4 Earth's field NMR system

The Earth's field NMR system is very similar to a conventional lab system but operates at audio frequency instead of hundreds of MHz. Very little power therefore is needed for the B_1 excitation enabling portable batteries to be a feasible power source.

For sea ice research the equipment needs to be portable and robust, to enable it to be transported by Skidoo. It also must be battery powered to allow sampling in a wide range of sites. Figure 46 shows a schematic of the system used, figure 47 shows the equipment in use and the Skidoo used for transportation.

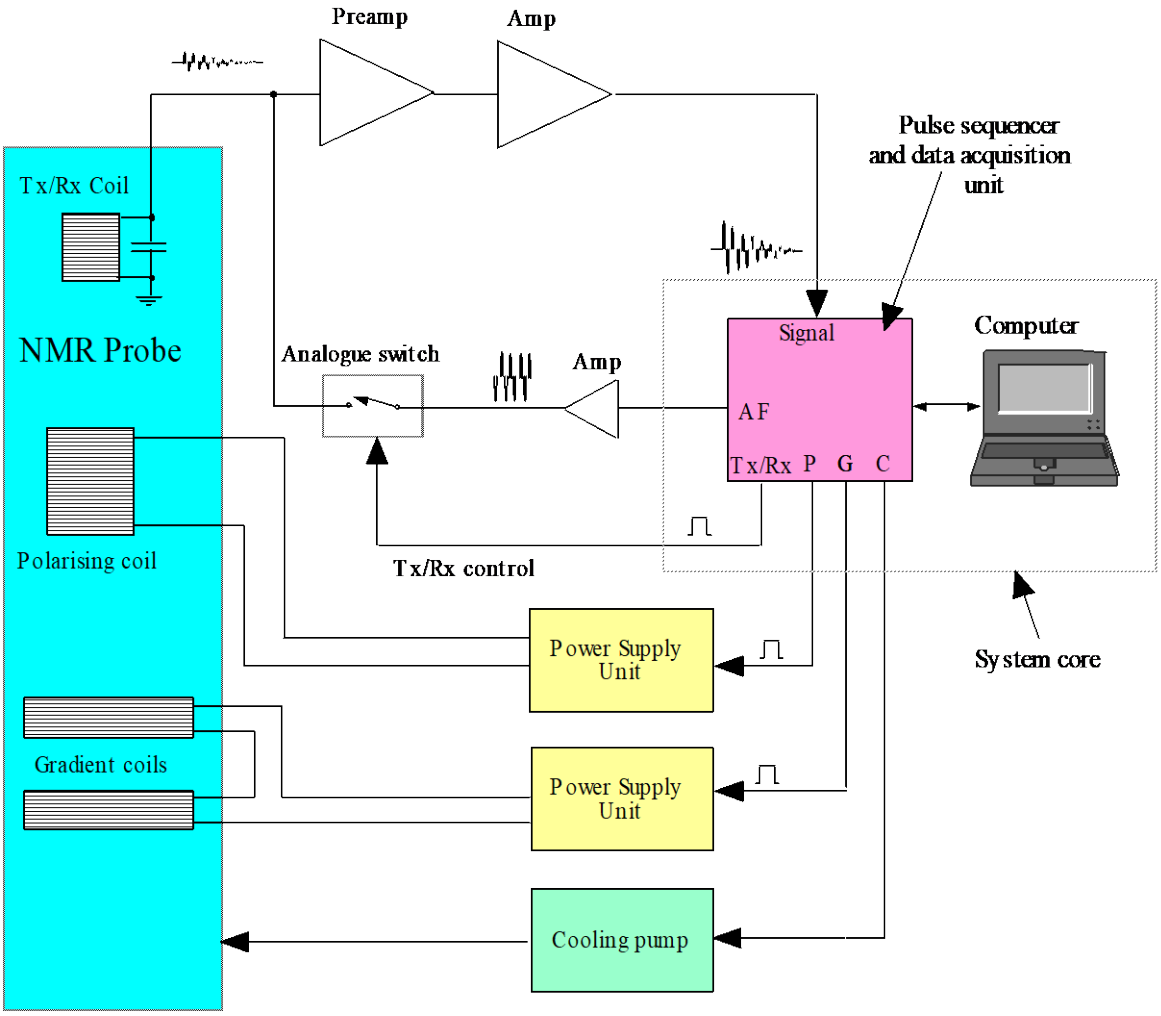

Figure 46 Earth's field NMR system schematic.

The system operating at audio frequency mean that standard OP amps and other audio components can be used in the transmit and receive sections. The received signal can also be digitised directly without the need for intermediate stages.

The main core of the system is the pulse sequencer and data acquisition and host computer. Other components are two variable10A constant current power supplies for driving the polarisation and gradient coils, an analog switch and a low noise OP amp for driving the B_1 or transmit coil, and an air circulating pump to cool the polarising coil between acquisitions.

The whole system runs off a single 24V DC power supply.

Figure 47 Earth's field NMR equipment.

Chapter 4

LAB WORK

4.1 Making artificial sea ice

4.1.1 Constraints on artificial ice formation

The major consideration when making sea ice is how it is originally frozen [3].
The following factors have an important influence:

Movement of saline solution - in natural sea ice there is a large amount of turbulent mixing during the initial freezing, due to wave and wind action, this creates frazil ice [1]. This ice effectively removes external sources of turbulence so the columnar ice that we are investigating is grown in a very calm environment [18]. Thus we must ensure that fan-induced wind in the freezers is kept to a minimum.

Directionality of cooling – While the columnar ice is forming it is kept at –4.5^{O}C on the underside by the seawater, which cannot be cooler without crystallising. The only cooling is from above, from the cold polar winter atmosphere. This dictates the direction of growth and so axis of the ice crystals [3]. Therefore the ice grown in the lab must be insulated on all sides, cooled only from the top and kept at -4.5^{O}C on the underneath.

Direction of growth – crystal growth is only in the vertical direction, due to the spatial constrictions imposed by neighboring ice crystals in the ice sheet [3]. Thus the horizontal dimensions of the ice-growth container are not critical as long as they are significantly larger that the size of individual ice crystals.

Rate of cooling – it has been shown [3] that the ice crystal and inclusion (both brine and air) sizes are directly related to the temperature gradient during formation; the larger the temperature gradient, the smaller the individual crystal and inclusion sizes. Therefore, as in the laboratory we have no frazil ice to insulate the columnar ice, we should not make the freezers as cold as the polar atmosphere at the time when the ice was formed.

Brine concentration fluctuations – as the sea water freezes it ejects concentrated brine out the bottom of the ice [41]. As the volume of sea water is large in comparison to the volume of concentrated brine rejected, this has no appreciable effect on the concentration of the seawater that the ice is formed from. Thus in the laboratory the volume of saline solution that the ice is formed from, must be large enough to not change in concentration significantly with the formation of ice [42].

4.1.2 Ice growth apparatus

The maximum dimensions of the ice sample to be imaged, is a cylinder 50mm tall with a diameter of 12mm. This is imposed by the size constraints of the bore of the 300mHz AMX Bruker spectrometer that we were using for our measurements. The sample fitted inside a glass cylinder, internal diameter 12mm, external diameter 14mm. It was decided that in order to prevent damaging the ice sample by cutting it to shape (by heating during cutting or otherwise), the ice sample would be grown in the sample tube. Figure 48 shows the apparatus developed to do this.

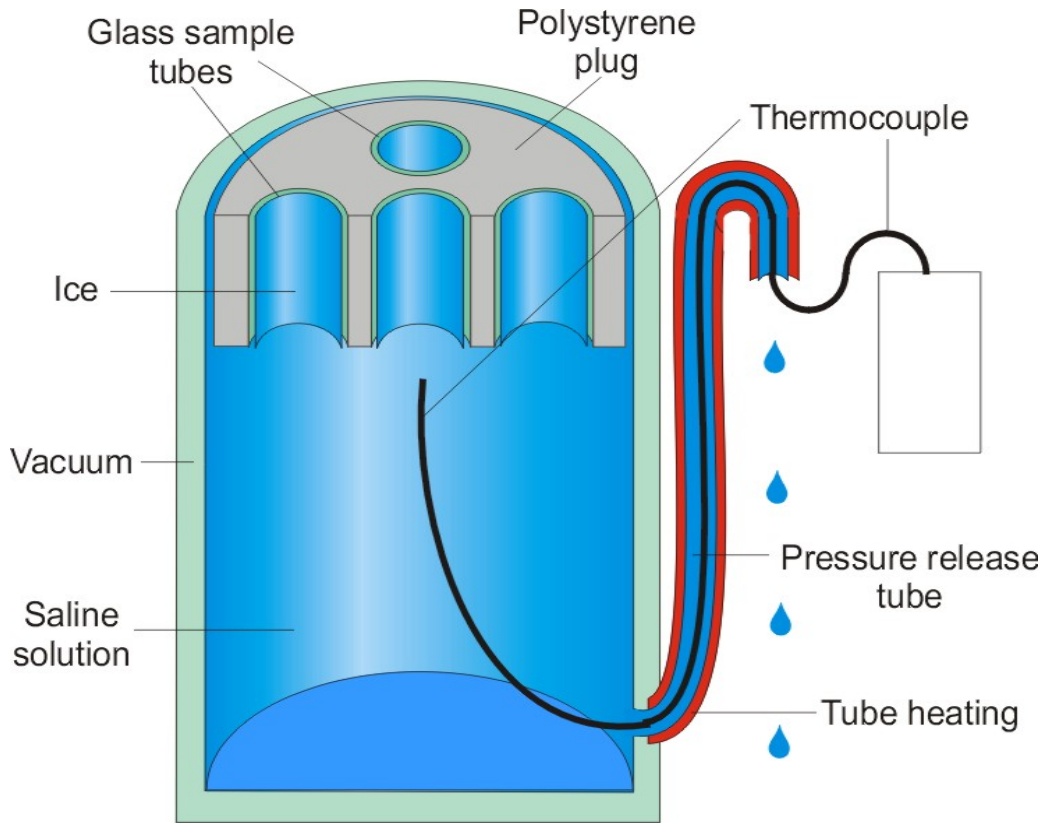

Figure 48 a cross section of the equipment designed to grow artificial sea ice.

The main vessel was double walled, with a vacuum between the two walls to insulate the ice on all sides except the upper surface. As the water in the tubes at the surface freezes it expands, a tube from the bottom of the vessel was needed to relieve the pressure this caused. This pressure-release tube is heated to prevent the liquid in it freezing. It also serves the purpose of keeping the saline solution beneath the sample tubes liquid and at approximately -4.5^{O}C. The temperature of the solution is monitored by means of a thermocouple inserted through the pressure release tube. The main glass vessel is of such a size that even if all the salt drained out of the ice in the sample tubes the concentration of salt in the reservoir would not change significantly. In the top of the double-walled glass vessel there is a cylinder 50mm high (the same height as the sample tubes) made of polystyrene. This has the sample tubes inserted into it and fits snugly into the top of the glass vessel, (see figure 49).

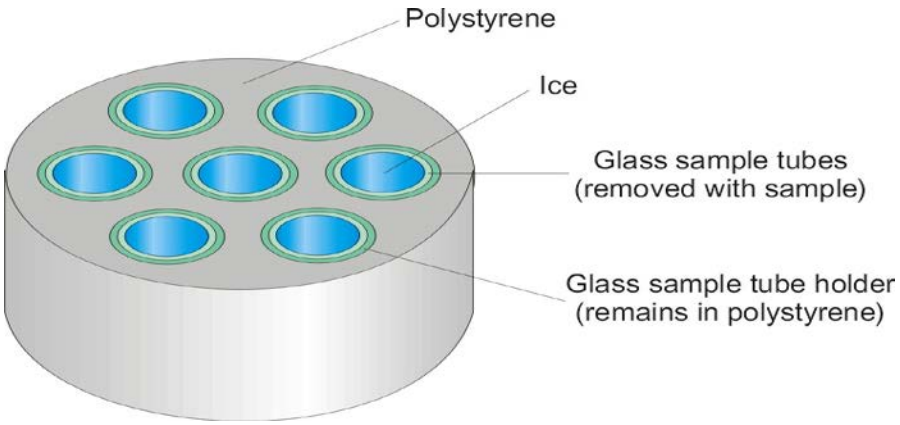

Figure 49 The polystyrene plug that holds the glass sample tubes, and ice samples, while the ice forms.

Polystyrene was used because of its highly insulative properties, its stiffness and machineability, and its ability to deform to provide a snug fit. In order to prevent the plug getting damaged, glass sample tubes were inserted into it. These tubes had an inner diameter 0.5mm larger than the outer diameter of the sample tubes. A piece of teflon tape was wrapped around the lower end of the sample tube to hold it snugly into the larger tubes. A 100mm glass tube of the same diameter as the sample tube was used to remove the sample tubes. There were four lines of string around the plug to aid extraction from the glass vessel. The bottom of the plug was flush with the ends of the sample tubes, in order to enable me to use a hot wire to remove any ice growth below the sample tubes which would otherwise prevent their removal.

This whole apparatus was placed in a freezer at –10^{O}C so as to cool the saline solution slowly.

4.2 Temperature gradient control within the spectrometer

4.2.1 Constraints due to machine design

The microimaging probe of the AMX 300MHz Bruker spectrometer has an inside bore diameter of 42mm, and a bore height of 103mm. The RF coil and sample must fit into this space.

The cooling system that is incorporated into the Bruker probe involves cooling the sample from the bottom, using cold nitrogen gas which is subsequently heated to a desired temperature. The volume of gas flow is manually determined and the amount of heating of the gas is controlled automatically to create the desired temperature at the base of the coil at any given gas flow. The temperature is monitored by a thermocouple at the base of the RF coil. To determine the temperature difference between the top and bottom of the sample (and so the temperature gradient), further thermocouples were placed on the top, and on the bottom of the sample. The amplified voltage was then calibrated to calculate the temperature difference.

This arrangement, when used with a standard RF coil, creates a temperature gradient of 2.2^{O}C/cm (the top of the sample being hotter) with a gas flow of 30% and the bottom held at -10^{O}C. An increase in gas flow would decrease the temperature gradient, but to avoid the excessive nitrogen consumption 30% was the practical maximum. This temperature gradient was unsatisfactory, as the top of the sample would melt at the required bottom temperature, and the brine pockets were moving at more than 6 mm/hr and so rapidly fell out of the sample. Also, to mimic Antarctic sea ice, the temperature gradient should be less than 1^{O}C/cm, and cooler at the top than the bottom.

Thermocouple data

N-type thermocouples were used as they are non-magnetic over their entire working range, and have a large operating temperature range of –50 to +250^{O}C, where they will give a constant voltage difference per ^{O}C [43 & 44].

They were connected in series, with the positive wires connected to each other, and copper wires soldered to the negative wires of each junction (see figure 50). The amplified current was then measured to determine the temperature difference between the ends of the sample.

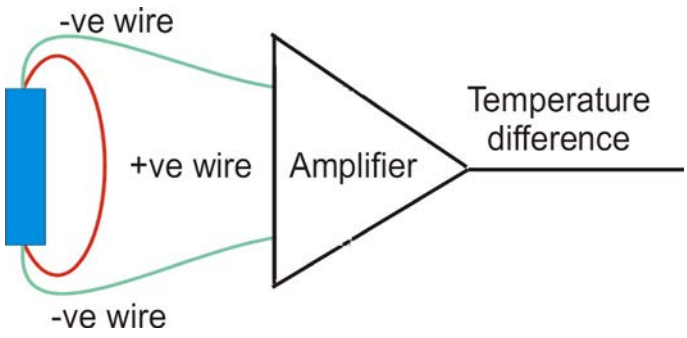

Figure 50 The thermocouples connected in series.

To determine the emf per ^{O}C of the thermocouples wired in series, I used two calibrated water baths at different temperatures. I plotted the voltage vs temperature difference and found the emf to be very stable and 27μV/^{O}C, (figure 51).

Figure 51 The temperature vs emf calibration curve

4.2.2 Different temperature gradient control devices

To modify and control the temperature gradient within the sample, several different methods were tried before a satisfactory control device was constructed.

In all cases MACOR (machinable glass ceramic [45]) plugs were used at the top and bottom of the sample, (see figure 52). MACOR is an excellent thermal conductor, an electrical insulator, and chemically unreactive. The glass sample tubes fitted into the plugs so the nitrogen did not cause evaporation of the samples. Small holes were drilled into the plugs to within 1mm of where the sample sat. The thermocouples were placed in these holes to be as close as possible to the sample ends without actually being in direct contact, and so risking corrosion and unrealistic results due to electrical conduction of the saline solution.

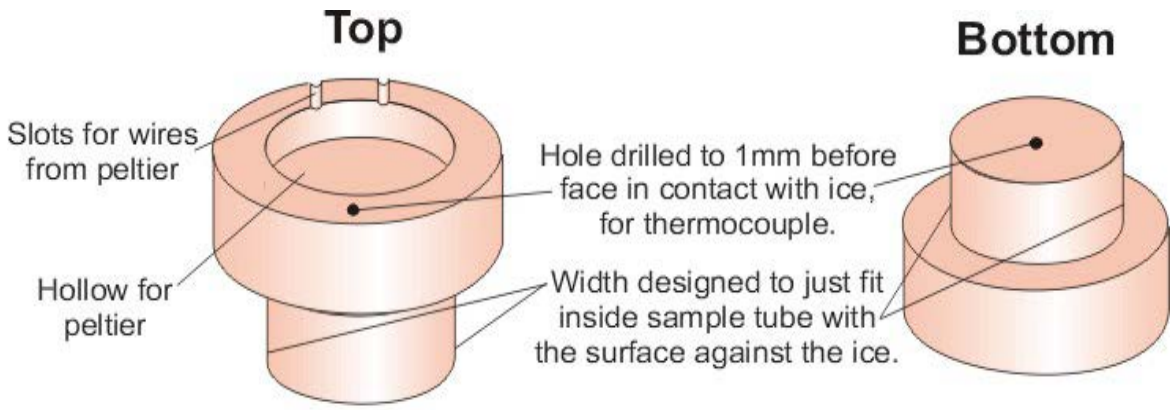

Figure 52 The MACOR plugs used at the top and bottom of the sample.

Method 1: Pumping cool nitrogen directly on top of the sample.

The first attempt made to obtain the desired temperature gradient, involved pumping unheated nitrogen directly on top of the sample, (see figure 53).

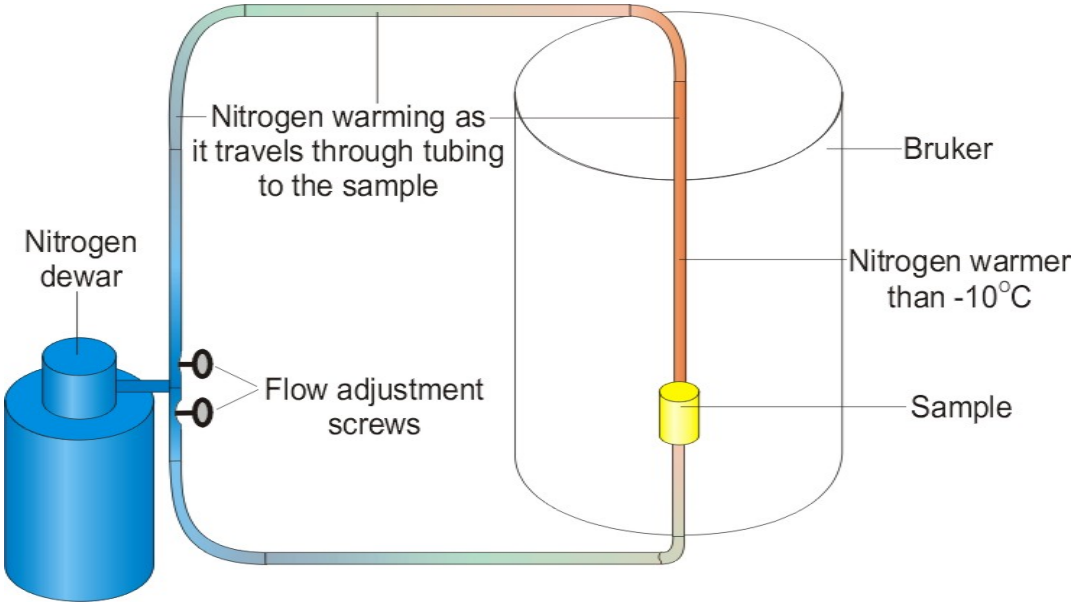

Figure 53 Direct nitrogen on top of the sample setup.

The nitrogen gas after it came out of the dewar (the rate of which is controlled from the Bruker interface) was split. One portion was directed into the magnet, directly on top of the sample, the other portion being directed to the base of the magnet and heated in the usual way. The relative amount of gas flow to the top and bottom of the sample was controlled by adjustable clamps on the pipes (see figure 53).

Unfortunately, the distance the nitrogen had to travel to the top of the sample was much greater than the conventional path to the base. This meant that by the time the nitrogen reached the top of the sample there had been so much external heating from the environment that the top could not be cooled as much as the bottom, and so another method had to be devised.

Method 2: Diverting nitrogen to the top of the sample.

Allowing for the nitrogen to come up through the base of the probe as usual and then diverting it to the top of the sample before the bottom was the basis of the next attempt.

The sample had to be insulated from the incoming air at the base, and insulated on the sides, to maintain a realistic and uniform temperature gradient. The RF coil with the largest internal diameter (26 mm) was used to allow for maximum insulation thickness. The equipment, as shown in figure 54, consisted of a polystyrene plug at the base to block the cold air from the base of the sample. This plug had pipes going through it to allow the cool air up to a cavity at the top of the sample. There were pipes leading down from this upper cavity to an air cavity between the bottom plug and the bottom of the sample, and there were further pipes leading from this lower cavity out through the upper cavity to the air above. The side insulation had to be between the nitrogen-directing pipes and the sample. Four pipes, equally spaced around the sample, were used for each direction of nitrogen flow, to ensure that the cooling was horizontally uniform. The nitrogen increased in temperature with time spent in the magnet (due to atmospheric heating), and so the temperature gradient within the sample could be determined by the rate of air flow.

Although the temperature control from this device was a vast improvement (I was able to maintain the top and bottom of the ice at the same temperature), it was not good enough. I needed the top to be cooler than the bottom, to mimic Antarctic conditions. I believe that the spatial constraints imposed by the internal diameter of the RF coil was the main performance limiting factor, as there was simply not enough room for sufficient insulation of the sample.

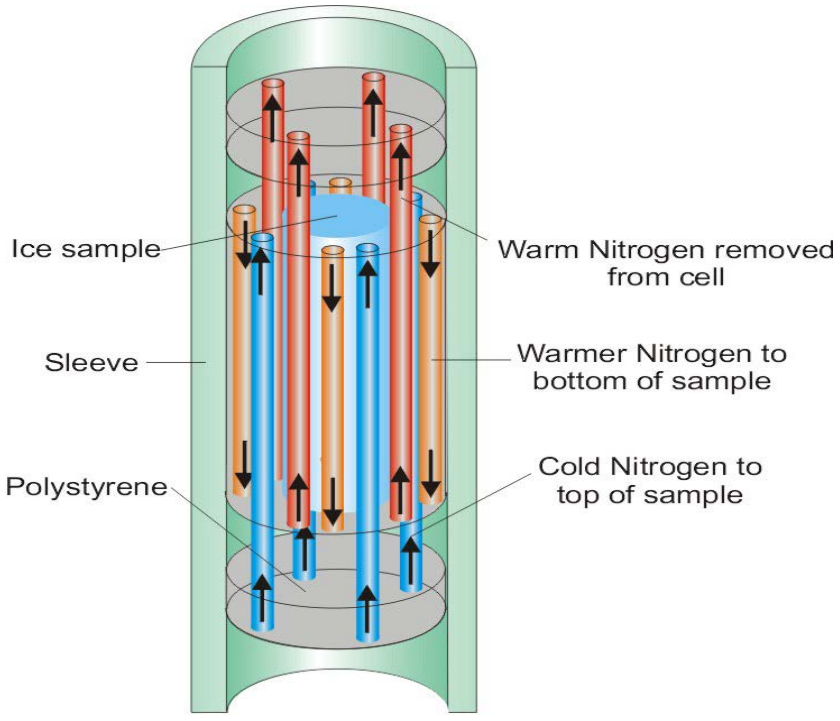

Figure 54 Polystyrene tube dodacky

Method 3: Incorporating a peltier device.

I decided a new approach was needed. Instead of redirecting the nitrogen, I would cool the top of the sample independently of the bottom. For this I used a peltier device on the top of the sample.

Peltier devices.

A semiconductor junction, as shown in figure 55, will absorb energy (heat) when electrons are driven from a low energy level in the p-type material to a higher energy level in the n-type material [46]. This is called a cold junction. The reverse situation occurs when electrons go from the n-type material to the p-type, and energy is expelled in the form of heat.

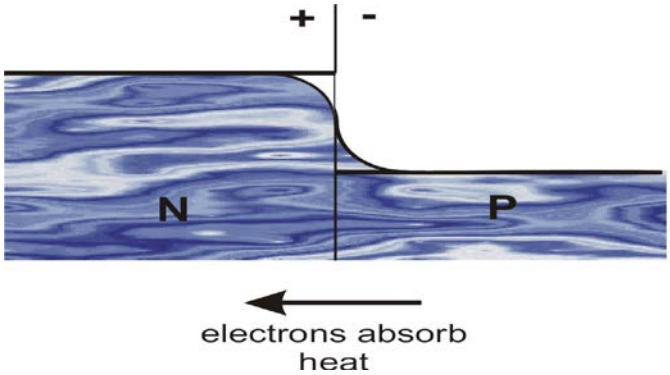

Figure 55 A semiconductor junction

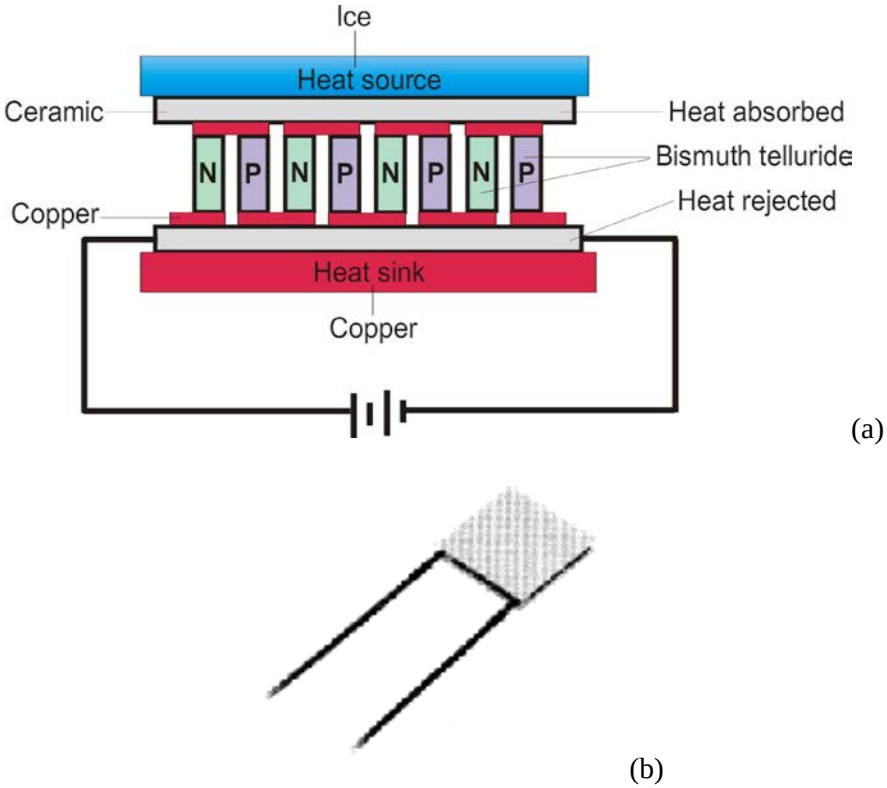

Figure 56 A peltier device
a) A schematic diagram. b) The actual appearance of the device [42].

A peltier device [42 & 47] is a series of many semiconductor junctions, usually heavily doped Bismuth Telluride, joined electrically in series and thermally in parallel. (See figure 56.) The p-type and n-type elements are soldered to copper connecting strips which are bonded to ceramic face plates. These electrically insulate the connecting strips from external surfaces. Heat absorbed at the cold junction is pumped to the hot junction at a rate proportional to current passing through the circuit and the number of junctions. The heat delivered to the hot side of the peltier includes the pumped heat as well as the electrical power dissipated by the device. This heat must be dissipated in some way, if it is not, the hot side of the device will heat up to the point where it will stop functioning as a cooling device and actually heat the cold surface.

The peltier device that I used was the smallest available, due to RF coil size constraints. It had a maximum power consumption of 1.4W, a maximum current of 3A, and a maximum voltage of 0.85V.

Automatic temperature control circuit

I developed a proportional temperature control circuit to maintain the temperature gradient automatically [48]. This used the amplified voltage from the thermocouples compared to a reference, and the amplified error voltage used to drive the peltier.
See figures 57 and 58.

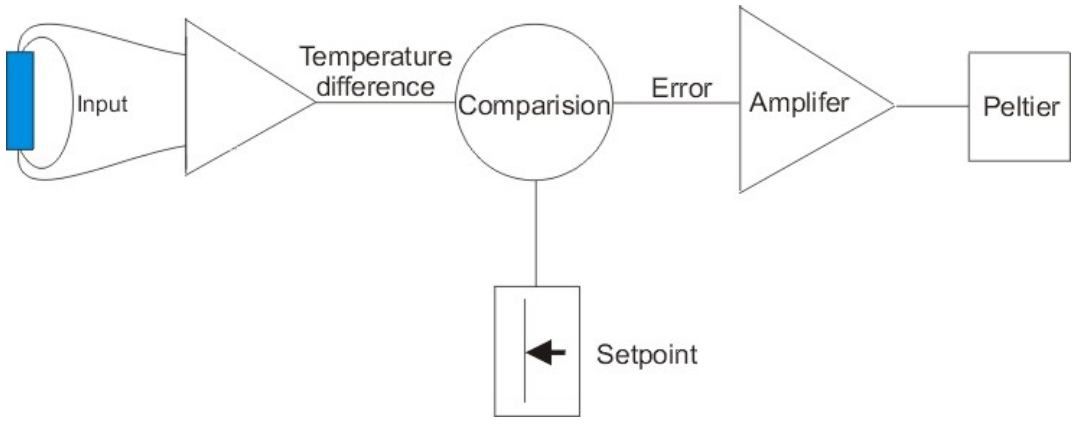

Figure 57 A schematic diagram of the thermocouple – peltier proportional temperature controller circuit.

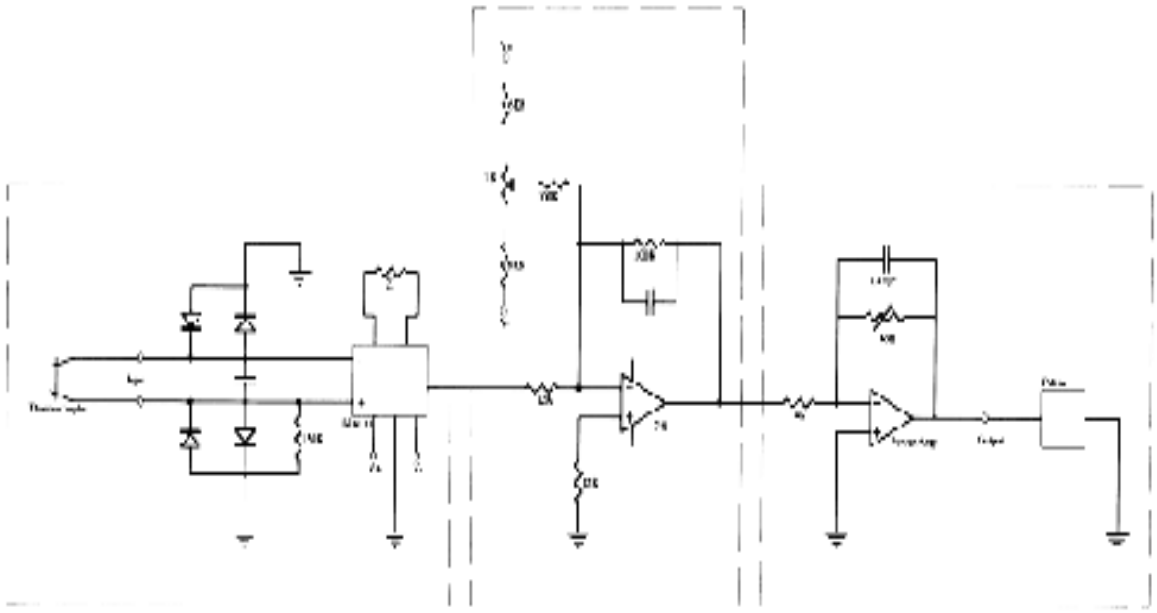

Part 1 Part 2 Part3

Figure 58 The actual circuit used.

Part 1. The induced emf from the thermocouples is 27μV per ^{O}C temperature difference. This is the input to the differential amplifier. The diodes are to protect the amplifier by limiting the input voltages to plus or minus 0.6V. The capacitor is there to help remove the high-frequency interference from the RF and gradient pulses. The 150KΩ resistor provides a ground path for the input bias current from the amplifier and prevents the input voltage from floating too high. The 22Ω resistor sets the gain of the amplifier to approximately 2000.

Part 2. The 6800Ω resistors were used to limit the adjustment range of the offset control and the current through the offset pot. The offset control 100KΩ resistor is to keep the gain of the offset equal to 1. The 12KΩ and 100KΩ resistors set the gain of the amplifier to 8.3. If the resistors were too small, too much current would be pulled from the differential amplifier, if they were too large they would be too noisy - the values were chosen to idealise this compromise. The 12KΩ resistor to ground is to compensate and ground the input bias current. 12KΩ is used to keep the impedence on the inputs approximately matched. The capacitor acts as a low-pass filter to limit the bandwidth, and so reduce noise.

Part 3. The power amplifier has an adjustable resistor to enable the gain to be increased slowly initially, to avoid temperature oscillations. The capacitor is to reduce high-frequency gain of the amplifier, therefore minimising the effect of high-frequency fluctuations caused by circuit interference, and the possibility of oscillation.

The nitrogen that was used to cool the base of the sample was afterwards directed onto the top of the peltier to reduce the temperature difference between the upper and lower peltier plates.

This temperature control circuit worked beautifully at room temperature. I was able to create and maintain a temperature gradient that was cooler on the top of the sample and had a magnitude of my choice.
Unfortunately however, it did not work with the base held at $-10^{O}C$, this was due to insufficient cooling of the upper surface of the peltier. In order to determine that insufficient cooling was the limiting factor, I dripped Acetone onto the upper surface of the peltier to induce rapid heat loss due to evaporative cooling (water and alcohol were tested before acetone, they improved the cooling albeit not sufficiently). Acetone was not considered as a permanent solution however, due to its corrosive properties.

Method 4: A peltier stack.

My first attempt to rectify the problem was to make a peltier stack, see figure 59. This greatly decreases the temperature difference between sides of the peltier. This markedly improved the performance of the overall device, but not sufficiently. Next I added a copper heat sink to the top of the upper peltier. This created further improvement, but still not enough.

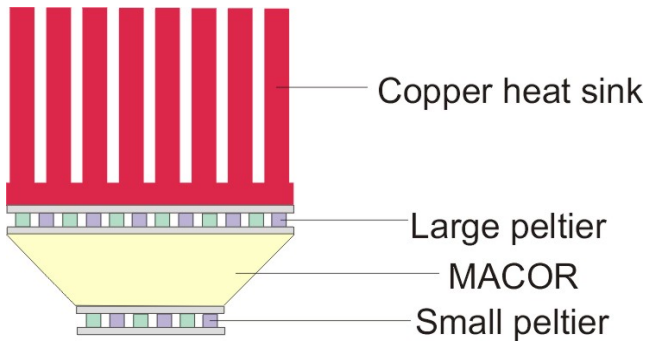

Figure 59 The peltier stack with a Copper heat sink on top.

I came to the conclusion that given the inability to remove sufficient heat from the upper surface of the peltier, I required a larger initial peltier.

The final method: Larger peltier, new RF coil.

Given the size constraints of the RF coil I was using, it was impossible to use a larger peltier. I decided I would be able to utilise the available bore space more constructively, and so use a larger peltier, if I constructed my own RF coil.

A saddle RF coil

A saddle coil, even though it will not give a field as homogenous as a solenoidal coil, is necessary to allow for ease of sample placement and extraction. The coil should be placed as close as possible to the sample, as the sensitivity varies with radius^{-1} [20]. The ideal configuration for a RF saddle coil is to have the upright wires at 60^{O}, 120^{O}, 240^{O}, and 300^{O}, all with equal amplitude current, and a current null at 0^{O} and 180^{O} [30]. The relative field lines and current direction are shown in figure 60.

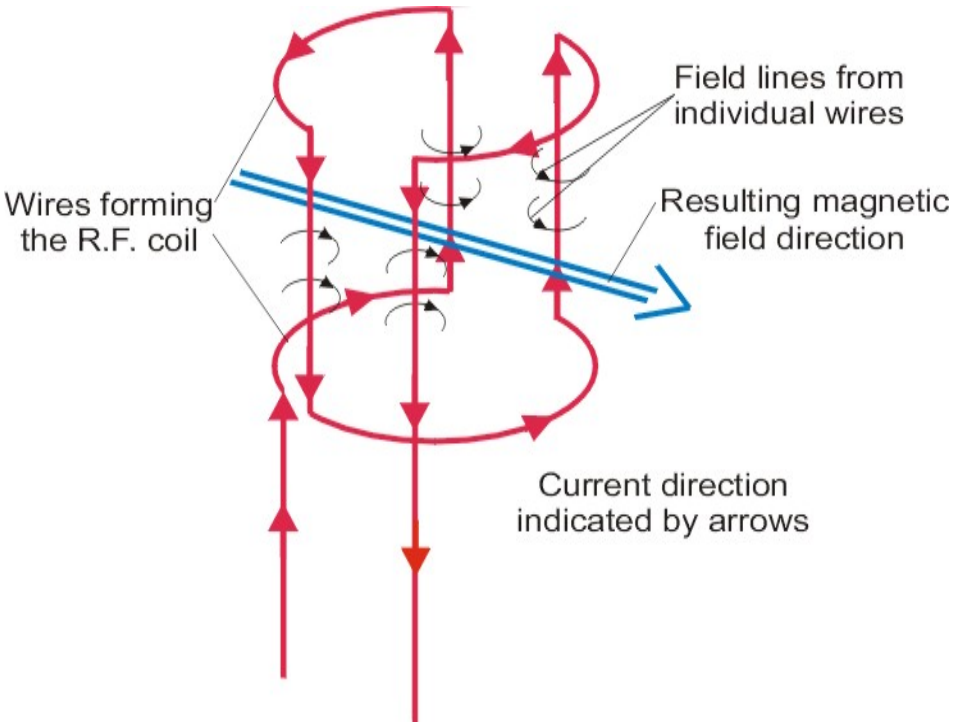

Figure 60 The RF saddle coil configuration.

To construct this coil as close to the sample as possible I designed it as a stand alone structure that would fit snugly around the sample tube. The optimum height for the saddle coil is four times the radius [49]. The coil was created flat, by bending the wire around nails (see figure 61), to enable the thickest possible wire to be used, thus giving maximum structural integrity. It was then bent to shape around a sample tube.

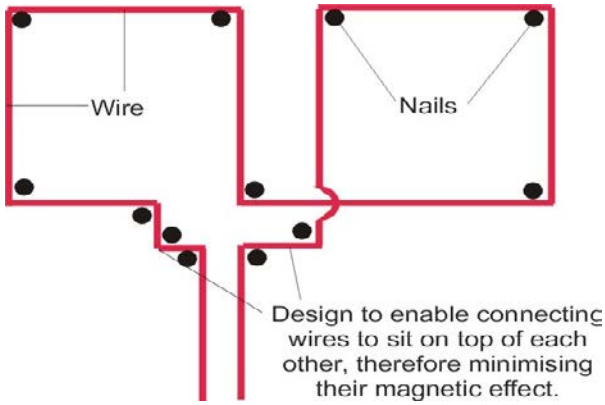

Figure 61 The RF saddle coil construction configuration.

The RF coil was wrapped in a layer of cork that sealed around the MACOR plug at the base of the sample. Outside this layer of cork was an air gap to allow the nitrogen up to cool the top of the peltier after cooling the lower MACOR plug. The cork around the RF coil insulated the sample from this nitrogen. Outside the air gap was a glass cylinder, for structural reasons, wrapped again in cork to reduce heating of the nitrogen from the gradient coils. The upper MACOR plug, which had the larger peltier on top of it, had its sides wrapped in cork before being inserted into a copper cooling cap that extended down into the air gap for maximum cooling. The copper cooling cap had the maximum dimensions allowed by the bore diameter. The outer cork and glass layer slotted into the cap, forcing all the nitrogen to escape through holes bored through the copper cap. There were slots cut in the glass and cork layer and in the outside of the copper cooling cap to allow the wires for the peltier and thermocouple to go out the top of the magnet.

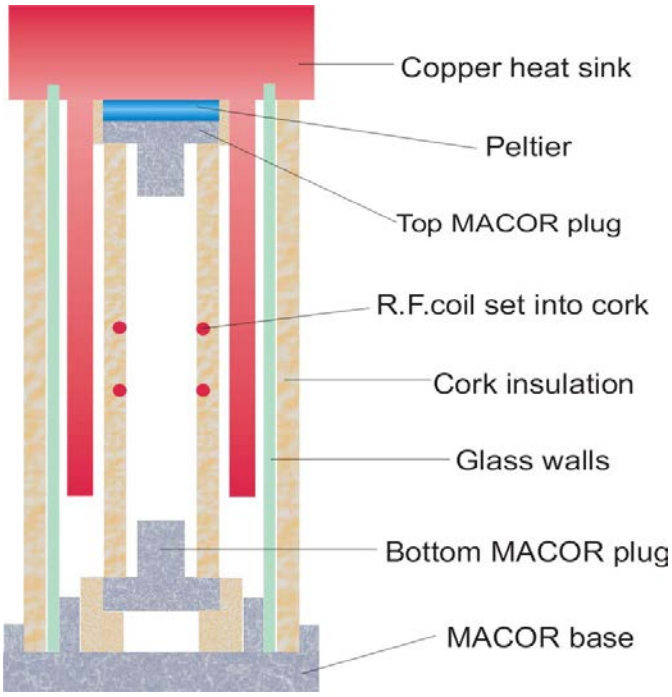

Figure 62 The final RF coil and temperature control design.

4.3 Single brine pocket construction

A single brine pocket was made in a pure ice crystal [11 & 50] to enable imaging results to be accurately correlated with optical measurements (the traditional method for examining sea ice).

4.3.1 Creating the brine pocket

There were six steps to creating a single brine pocket in the center of an ice crystal:

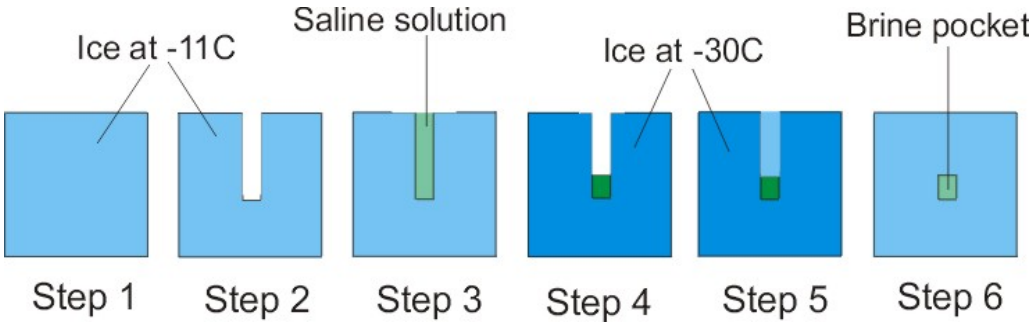

Figure 63 Six steps in the creation of a brine pocket

Step 1. De-ionised water was boiled to remove the gas component. The water was frozen in a layer 30mm deep, removed from the container, and cut into blocks to fit the RF coil. The crystal boundaries were clearly visible as lines in the ice sheet, but were avoided, as the brine would drain out of the sample along the crystal boundary. An –ll^{O}C freezer was used to avoid excessively small crystals, as crystal size decreases with lowering external temperatures.

Step 2. Holes with a width of 0.7mm were drilled 16mm deep into the ice sample.

Step 3. Saline solution that is concentrated enough to be liquid at –ll^{O}C, was injected into the holes. The samples were then placed in a –30^{O}C freezer, to freeze the saline solution.

Step 4. The holes were re-drilled to a depth of 14mm.

Step 5. Fresh de-ionised water was injected into the hole and frozen.

Step 6. The sample was transferred back into the –ll^{O}C freezer and the saline ice melted leaving a pocket of saline solution in the center of the sample.

4.3.2 Imaging

The sample containing the single brine pocket was wrapped in tissue paper and placed inside a sample tube in the spectrometer. A typical image is shown in figure 64.

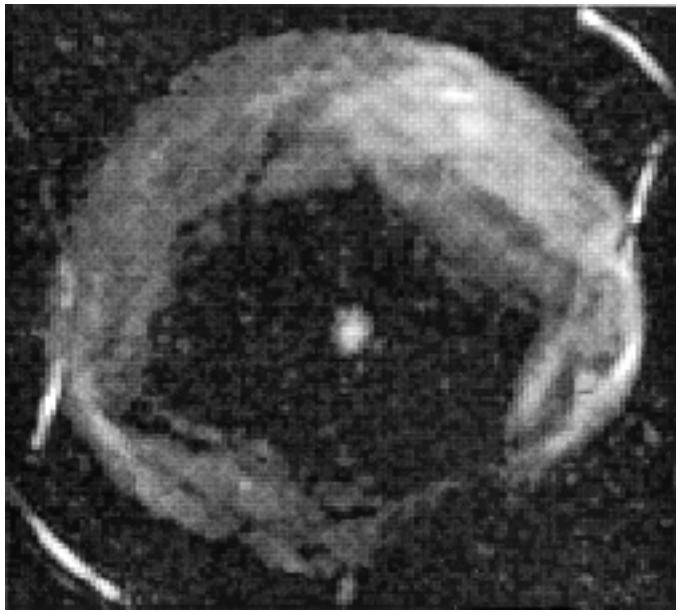

Figure 64 A 1cm thick slice through the sample. The spot in the middle is the brine pocket, the dark area around it is the ice, and the signal around that is from the moist tissue paper. The bright curved line on the perimeter of the image is the result of condensation on the outside of the sample tube. The fact that it curves in on the side is due to the image folding back where it exceeded the field of view.

This imaging was done with the cooling just from the base of the sample, before the temperature gradient control systems were in place. The large temperature gradient resulted in a very rapid migration of the brine pockets. Twenty minutes after I took the above image the brine pocket had shifted down by more than 1cm and so was impossible to image. Due to the length of time it takes to make diffusion and imaging measurements this rate of migration rendered the experiments impossible without further temperature control.

A problem I encountered was the brine pocket becoming split into smaller fractions. This was due to the temperature of the sample warming slightly while being transferred from the freezer to the spectrometer. This caused the brine pocket to expand, melting the surrounding ice to maintain the saline equilibrium concentration for the higher temperature. When the sample was cooled again, the concentration was raised by water crystalising out, usually in the form of thin plates throughout the pocket cavity, thus splitting the original brine pocket into many smaller fractions so

creating many small brine pockets. These plates were clearly observable when the sample was removed from the spectrometer.

After the temperature gradient control was set up, I found that it stabilised the sample sufficiently that I could make easily definable and consistently traceable brine pockets by simply freezing saline solution. This meant that the creation of a single pocket was unnecessary.

4.4 Bruker experiments

There were four different experiments carried out on the temperature gradient controlled ice sample in the AMX 300MHz Bruker spectrometer. These were as follows;

Image – This experiment looked at a vertical slice through the center of the sample. The image was of an area of $15mm^2$, and had 128^2 data points.
The images were used to ensure a wide range realistic of brine pocket sizes were being examined, and also to track the movement of individual brine pockets over time.
An image was taken once the sample had come to equilibrium with a desired temperature gradient, and then again two hours later, to determine the shift of brine pockets over time with various temperature gradients.

Diffusion – This was a Pulsed Gradient Spin Echo (PGSE) experiment used to determine the average diffusion rate over the whole sample. This experiment was done using various combinations of gradient directions and magnitudes to determine the diffusion rate of the sample in different directions.
This experiment was done to enable the overall diffusion rates in different directions to be determined. It was done at different temperature gradients, to determine how the samples' overall diffusion rates change, with a change in temperature gradient.

Diffusion weighted image – This experiment is very similar to the diffusion experiment except that it examines the diffusion rate at each point in the sample slice, rather than over the sample. In this case the area of the sample being examined was the same as in the image experiment. This was to enable the diffusion rates of the brine pockets to be correlated with their dimensions.

3D Image – This experiment obtains a three-dimensional, cubic image of the sample volume. The dimension of the image was $15mm^3$ and it consisted of 128^3 data points.
This experiment was done to ensure I had a realistic sea ice sample with a normal number and range of brine pocket sizes.

4.5 Anisotropic diffusion analysis

4.5.1 Diffusion tensor theory

As sea ice is anisotropic (ie, the structure varies depending on viewing orientation) the diffusion rate in one direction, may be very different from that in other directions. For example, there may be much faster diffusion along a local axis at some point in the sample than in directions transverse to that axis. We call the local fast diffusion axis Z and the transverse axes X and Y. Our measurement frame is determined by the laboratory fixed axis of our magnetic field gradient, (x, y, z). It is possible, using various combinations of gradients in the x, y, z frame, to create a matrix for each point within the sample that will describe the diffusion rates in the local X, Y, and Z directions [51 & 52].

The local anisotropy, caused by crystal growth direction, can vary throughout the sample, and so will present a variety of orientations with respect to the applied gradient fields. To determine the diffusion in the local coordinate system, we must find a rotation matrix to translate between the local coordinate system and the applied coordinate system. This enables us to examine the diffusion rates parallel and perpendicular to the crystal growth direction, (see figure 64).

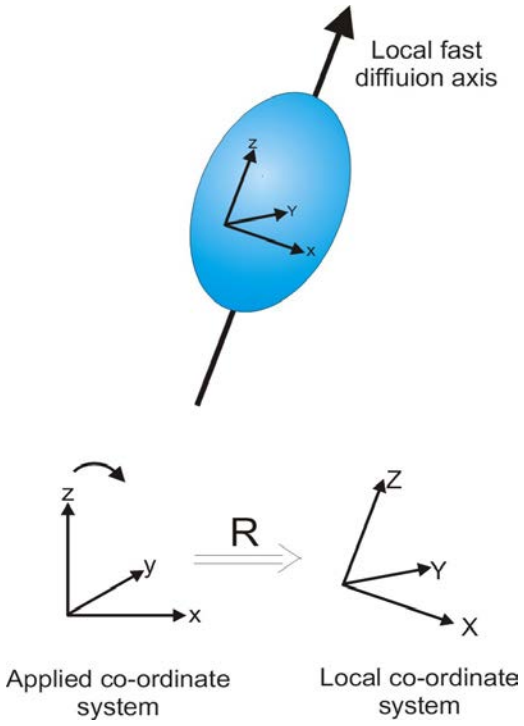

Figure 64 Translation between local and laboratory systems

The echo magnitude from a PGSE experiment is given by [12]:

$$E = e^{-\underline{g}\,\underline{\underline{D}}\,\underline{g}\gamma^2\delta^2\left(\Delta-\frac{1}{2}\delta\right)} \tag{21}$$

Where the diffusion tensor $\underline{\underline{D}}$ is defined by $\underline{\underline{D}} = R^{-1}\underline{\underline{D_l}}R$, where the local diffusion matrix is $\underline{\underline{D_l}} = \begin{bmatrix} D_{XX} & 0 & 0 \\ 0 & D_{YY} & 0 \\ 0 & 0 & D_{ZZ} \end{bmatrix}$ *and* $\underline{\underline{D}} = \begin{bmatrix} D_{xx} & D_{xy} & D_{xz} \\ D_{yx} & D_{yy} & D_{yz} \\ D_{zx} & D_{zy} & D_{zz} \end{bmatrix}$ (22)

R is the rotation matrix which transfers the x, y, z, laboratory frame to the local X, Y, Z, frame.

The gradient vector is denoted by $\underline{g} = \left(g_x,\ g_y,\ g_z\right)$. We will use 7 combinations of gradient directions:

$$\begin{aligned} g = \quad & g(1 \quad 0 \quad 0) \\ & g(0 \quad 1 \quad 0) \\ & g(0 \quad 0 \quad 1) \\ & \tfrac{1}{\sqrt{2}}\, g(1 \quad 1 \quad 0) \\ & \tfrac{1}{\sqrt{2}}\, g(1 \quad 0 \quad 1) \\ & \tfrac{1}{\sqrt{2}}\, g(0 \quad 1 \quad 1) \\ & \tfrac{1}{\sqrt{3}}\, g(1 \quad 1 \quad 1) \end{aligned} \tag{23}$$

With each of these gradient direction combinations, a series of 10 different gradient magnitudes were used.

The slope of the line obtained by plotting the natural log of the echo magnitude vs the gradient magnitude squared (figure 65) will be:

$$\gamma^2 g^2 \delta^2 \left(\Delta - \tfrac{1}{2}\delta\right) \sum_{ij} (e)_i D_{ij} \left(e^t\right)_j \tag{24}$$

where e is the gradient direction unit vector (e_x, e_y, e_z) combination, e^t is the transpose of e, and D_{ij} is the rate of diffusion in the ij direction.

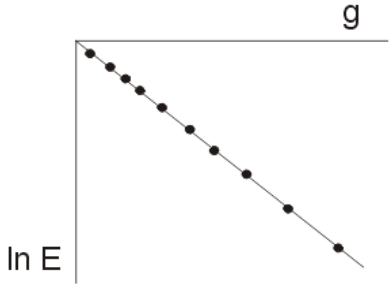

Figure 65 ln E vs g^2 for a given e vector, yielding from the slope, a particular matrix element D_{ij}

If for example, a gradient in just the x-direction is used $\sum_{ij}(e)_i D_{ij}\left(e^t\right)_j$ can be written:

$$\begin{bmatrix}1 & 0 & 0\end{bmatrix}\begin{bmatrix}D_{xx} & D_{xy} & D_{xz}\\ D_{yx} & D_{yy} & D_{yz}\\ D_{zx} & D_{zy} & D_{zz}\end{bmatrix}\begin{bmatrix}1\\0\\0\end{bmatrix} = D_{xx} \tag{25}$$

Therefore the following gradient direction combinations, and their corresponding e-vectors will lead to the following diffusion coefficients:

$$\begin{aligned}
&[1,0,0] \Rightarrow D_{xx}\\
&[0,1,0] \Rightarrow D_{yy}\\
&[0,0,1] \Rightarrow D_{zz}\\
&1/\sqrt{2}\,[1,1,0] \Rightarrow \tfrac{1}{2}\left(D_{xx}+D_{xy}+D_{yx}+D_{yy}\right)\\
&1/\sqrt{2}\,[1,0,1] \Rightarrow \tfrac{1}{2}\left(D_{xx}+D_{xz}+D_{zx}+D_{zz}\right)\\
&1/\sqrt{2}\,[0,1,1] \Rightarrow \tfrac{1}{2}\left(D_{yy}+D_{yz}+D_{zy}+D_{zz}\right)\\
&1/\sqrt{3}\,[1,1,1] \Rightarrow \tfrac{1}{3}\left(D_{xx}+D_{yy}+D_{zz}+2\left(D_{xy}+D_{yz}+D_{zx}\right)\right)
\end{aligned} \tag{26}$$

As $D_{ij} = D_{ji}$, we can, using the seven gradient direction combinations above, create seven simultaneous equations that can be solved to enable us to determine the six diffusion coefficients given below:

$$\begin{bmatrix}D_{xx} & D_{xy} & D_{xz}\\ D_{yx} & D_{yy} & D_{yz}\\ D_{zx} & D_{zy} & D_{zz}\end{bmatrix} \tag{27}$$

A rotation matrix (R) can then be found to diagonalise the above matrix

$$\begin{bmatrix}D_{xx} & D_{xy} & D_{xz}\\ D_{yx} & D_{yy} & D_{yz}\\ D_{zx} & D_{zy} & D_{zz}\end{bmatrix} = R^{-1}\begin{bmatrix}D_{XX} & 0 & 0\\ 0 & D_{YY} & 0\\ 0 & 0 & D_{ZZ}\end{bmatrix}R \tag{28}$$

Thus giving us the values for diffusion in the X, Y, and Z-directions as well as the orientation of the local axes with respect to the laboratory axes. This was done for every pixel in the image.

4.5.2 Diffusion tensor Matlab and C program

The programs written to determine these diffusion tensors are given in Appendix 3. Initially the program was written in Matlab. It was then converted to C to enable it to be incorporated into Prospa, the software package that we use to analyse our experimental results [53].

The program consists of 5 parts:

Part 1. There are seven combinations of gradient directions, labelled (a) through (g). For each one of these there are 10 different gradient magnitudes, g1 through g10. Therefore the inputs are 7 x 10 (128 x 128) matrices, these are labelled Ea1(i,j), Ea2(i,j), Ea3(i,j),……Eg9(i,j), Eg10(i,j).
There are also the seven related constants γ_a, γ_b, etc. that are the values of $\gamma^2 g^2 \delta^2 \left(\Delta - \frac{1}{2}\delta\right)$ for each gradient direction combination.

Part 2. The same position (i,j) in each of the Ea's (Ea1 through Ea10), are combined and simultaneous equations (see below) are used to find the slope (m), of the line between them.

$$\begin{bmatrix} g1^2 & 1 \\ g2^2 & 1 \\ g3^2 & 1 \\ \vdots & \vdots \\ g9^2 & 1 \\ g10^2 & 1 \end{bmatrix} \begin{bmatrix} m \\ c \end{bmatrix} = \begin{bmatrix} Ea1(i,j) \\ Ea2(i,j) \\ Ea3(i,j) \\ \vdots \\ Ea9(i,j) \\ Ea10(i,j) \end{bmatrix} \tag{29}$$

Where g1 through g10 are the different gradient magnitudes.
The same is done for the Eb's through Eg's, thus resulting in 7 (128 x 128) matrices, Ma through Mg.

Part 3. The matrices Ma through Mg are multiplied by the constants γ_a through γ_b, and called Da through Dg.

Part 4. Simultaneous equations are then used to find D_{xx}…. D_{zz}

$$\begin{bmatrix} 1 & 0 & 0 & 0 & 0 & 0 \\ 0 & 1 & 0 & 0 & 0 & 0 \\ 0 & 0 & 1 & 0 & 0 & 0 \\ \frac{1}{2} & \frac{1}{2} & 0 & 1 & 0 & 0 \\ \frac{1}{2} & 0 & \frac{1}{2} & 0 & 1 & 0 \\ 0 & \frac{1}{2} & \frac{1}{2} & 0 & 0 & 1 \\ \frac{1}{3} & \frac{1}{3} & \frac{1}{3} & \frac{2}{3} & \frac{2}{3} & \frac{2}{3} \end{bmatrix} \begin{bmatrix} D_{xx} \\ D_{yy} \\ D_{zz} \\ D_{xy} \\ D_{xz} \\ D_{yz} \end{bmatrix} = \begin{bmatrix} D_a \\ D_b \\ D_c \\ D_d \\ D_e \\ D_f \\ D_g \end{bmatrix} \tag{30}$$

$$B \qquad D_v \qquad A$$

This is solved to find D_v, which is then put into a matrix D

$$D_v = \begin{bmatrix} D_{xx} \\ D_{yy} \\ D_{zz} \\ D_{xy} \\ D_{xz} \\ D_{yz} \end{bmatrix} \quad \Rightarrow \quad D = \begin{bmatrix} D_{xx} & D_{xy} & D_{xz} \\ D_{yx} & D_{yy} & D_{yz} \\ D_{zx} & D_{zy} & D_{zz} \end{bmatrix} \tag{31}$$

Part 5. The matrix D is then diagonalized by finding the eigenvalues (rotation matrices) and the eigenvectors (diffusion tensor) [52]. These are stored in (128 x 3 by 128 x 3) matrices called RM and DT respectively.

4.5.3 Diffusion tensor program test

Starting with a diffusion tensor with arbitrary values, I then worked backwards manually, to find the input matrices. Putting these into the computer program should yield the original diffusion tensor. For the purposes of the test I let the constants γ_a, through γ_g, all equal 1, and decided that there would only be 3 gradient magnitudes used (the greater number of points (gradient magnitudes) on the graph, the better the accuracy, so this will not make the results unrealistically accurate).

The chosen diffusion tensor was:

$$DT = \begin{bmatrix} D_{XX} & & \\ & D_{YY} & \\ & & D_{ZZ} \end{bmatrix} = \begin{bmatrix} 1 & & \\ & 2 & \\ & & 3 \end{bmatrix} \tag{32}$$

This was rotated around the z-axis.

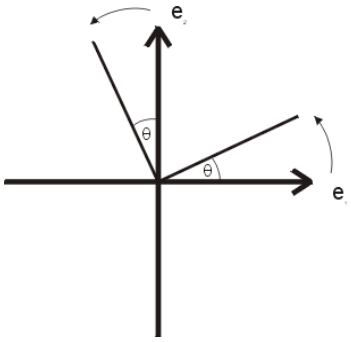

$$\begin{aligned} e_1 &\rightarrow \cos e_1 + \sin e_2 \\ e_2 &\rightarrow -\sin e_1 + \cos e_2 \end{aligned} \Rightarrow \begin{bmatrix} \cos\theta & \sin\theta & 0 \\ -\sin\theta & \cos\theta & 0 \\ 0 & 0 & 1 \end{bmatrix} = R_z(\theta) \tag{33}$$

Letting $\theta = 45^O$ resulted in:

$$R_z(45^o) = \begin{bmatrix} .707 & -.707 & 0 \\ .707 & .707 & 0 \\ 0 & 0 & 1 \end{bmatrix} \qquad R_z^{-1}(45^o) = \begin{bmatrix} .707 & .707 & 0 \\ -.707 & .707 & 0 \\ 0 & 0 & 1 \end{bmatrix} \tag{34}$$

Therefore the rotated matrix was:

$$D = R_z^{-1}(45^o)\, DT\, R_z(45^o) = \begin{bmatrix} 1.5 & 0.5 & 0 \\ 0.5 & 1.5 & 0 \\ 0 & 0 & 3 \end{bmatrix} \tag{35}$$

Using this, the solutions to the simultaneous equations can be found:

$$\begin{aligned} D_a &= 1.5 \\ D_b &= 1.5 \\ D_c &= 3 \\ D_d &= \tfrac{1}{2}(1.5+1.5+2\times 0.5) = 2 \\ D_e &= \tfrac{1}{2}(1.5+3+2\times 0) = 2.25 \\ D_f &= \tfrac{1}{2}(1.5+3+2\times 0) = 2.25 \\ D_g &= \tfrac{1}{3}(1.5+1.5+3+2\times 0.5) = 2.33 \end{aligned} \tag{36}$$

These are the gradients of the seven lnE vs g^2 graphs, so knowing the values of g to be 1, 2, and 3, we can deduce the values of the input matrices (which will be 1 by 1 matrices in this case).

Therefore the input matrices are:

Ea1 = [1.5]	Eb1 = [2.5]	Ec1 = [3]	Ed1 = [2]	Ee1 = [2.25]
Ea2 = [6]	Eb2 = [7]	Ec2 = [12]	Ed2 = [8]	Ee2 = [9]
Ea3 = [13.5]	Eb3 = [14.5]	Ec3 = [27]	Ed3 = [18]	Ee3 = [20.25]

Ef1 = [1.25]	Eg1 = [2.33]
Ef2 = [8]	Eg2 = [9.32]
Ef3 = [19.25]	Eg3 = [20.97]

When these were put into the Matlab program and the C program the following diffusion matrix was produced:

$$DT = \begin{bmatrix} 1.0017 & 0 & 0 \\ 0 & 1.9992 & 0 \\ 0 & 0 & 3.0004 \end{bmatrix} \tag{37}$$

The errors in these values are most likely due to computational rounding errors.

Chapter 5

FIELD WORK RESULTS

The earlier Earth's field NMR work carried out in 1995 and 1997 has shown that there tends to be a diffusion rate faster than that of water in the sea ice cores examined. With the improved equipment however, the ice core disturbance is greatly decreased and the number of experiments was greatly increased. The results will therefore be more accurate and precise than those obtained in the past. The experiments were conducted between the 20th and the 28th of October 1999. The average air temperature was -16^0C in the daytime and -30^0C in the evenings and early mornings. For further experimental information see section 3.1.1.

5.1 Ice core probe results

As soon as the probe was set up (as described in section 3.2) a free induction decay (FID) experiment was run to determine the brine content of the ice core. We did 8 scans in the experiment, which took approximately 1.5 minutes to run. A pulsed gradient spin echo (PGSE) experiment was then run without moving the probe. The PGSE experiment took approximately 21 minutes to complete an 8 scan run. After this another FID experiment was run. If this showed no significant increase in the water fraction of the sample then another PGSE experiment would be run. It was found that if more than two PGSE experiments were run on the same position of the same ice core the liquid content would significantly increase. The temperature profile within the ice sheet was also recorded daily.

5.1.1 Signal-to-noise measurements

These were done using a water sample the same size as the ice core. The noise was found to increase significantly when the probe was placed in the ice sheet. This was due to the coupling capacitance within the ice sheet. To reduce this coupling a sheet of metal foil was wrapped around the base of the probe and earthed. The results are shown in figure 66. The figure shows the digital output of the analogue-to-digital converter on the Tecmag system. The absolute value is proportional to the signal voltage presented at the input. For the purpose of the present analysis we refer to the value in arbitrary units. The root mean squared (rms) noise level was 304 units without the foil and 84 units with the foil.

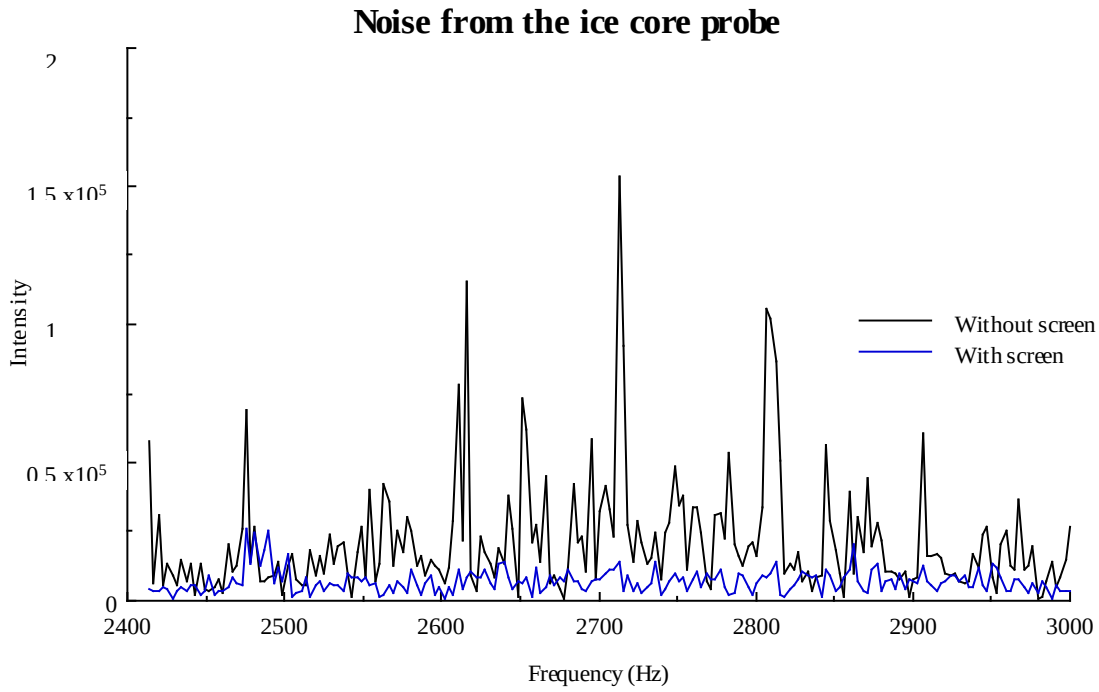

Figure 66 Noise from the ice-core probe in the ice sheet, with and without a metal foil screen.

5.1.2 Temperature measurements

A typical temperature profile through the ice sheet [54] is given in figure 67. This figure shows the actual temperatures measured at the experimental site on 26/10/99 at 4pm. The temperature at 750mm is -10.7^0C and the temperature at 1100mm is -7.7^0C.

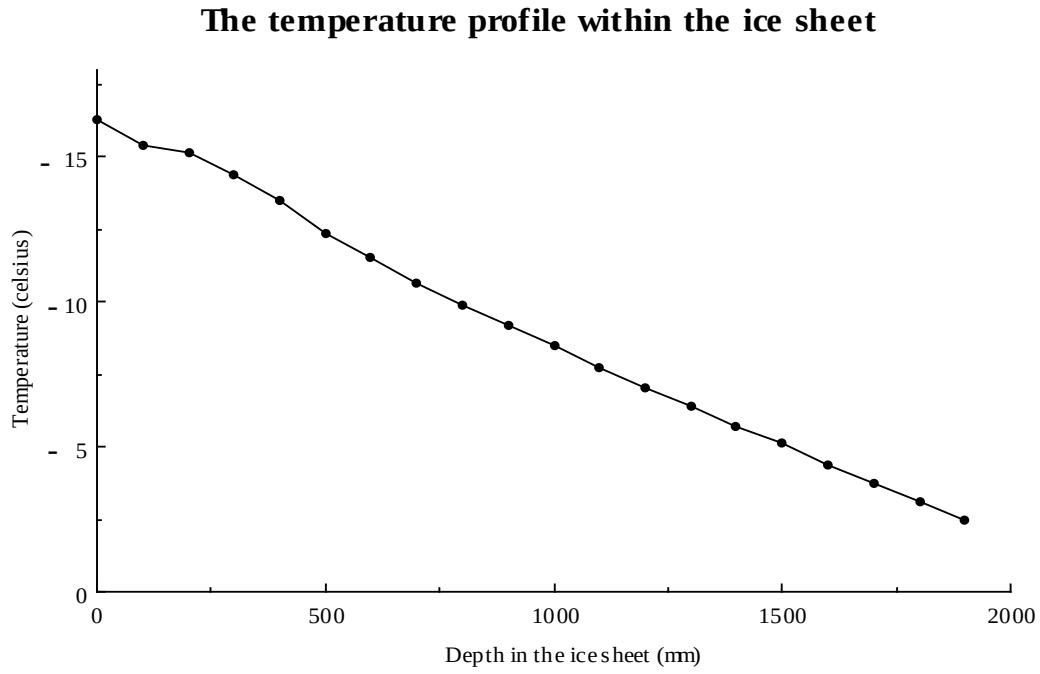

Figure 67 The temperature in the ice sheet at the experimental site at 4pm on 26/10/99.

5.1.3 Free Induction Decay (FID) results

The water content of the ice cores can be determined by comparing the magnitude of the signal received from a water sample to the magnitude of the signal from an ice sample of the same size. The magnitude of the signal is determined from the area under the peak in the frequency spectrum (see figure 68). The resultant water content was found to be approximately 4% at 750mm and 3% at 1100mm.

The signal magnitude for one scan on a water sample was 17.5 x 10^2 units giving a signal to noise value of 20.8.

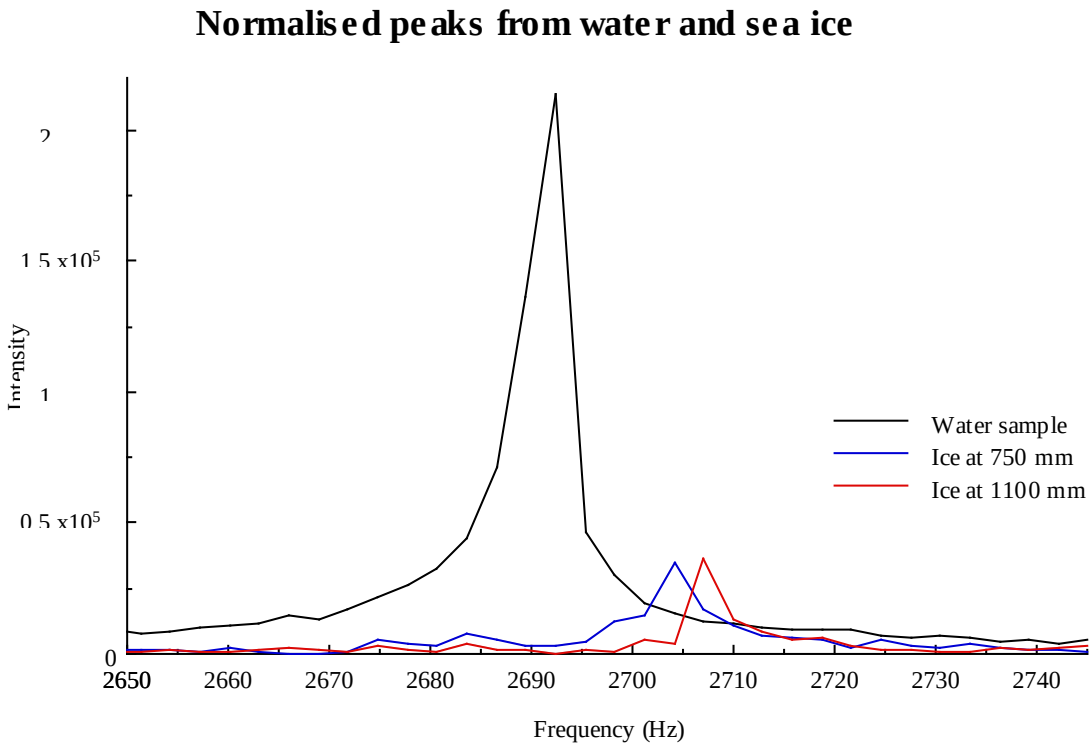

Figure 68 Normalised water peaks for water and sea ice samples.

The water content increase over the period of the experiments can be seen by the changing magnitudes of the water peak in figure 69. The average water content increased by approximately 6% from the beginning of the experiments to the end. Figure 69 shows the FIDs from one of the experiments at a depth of 1100 mm.

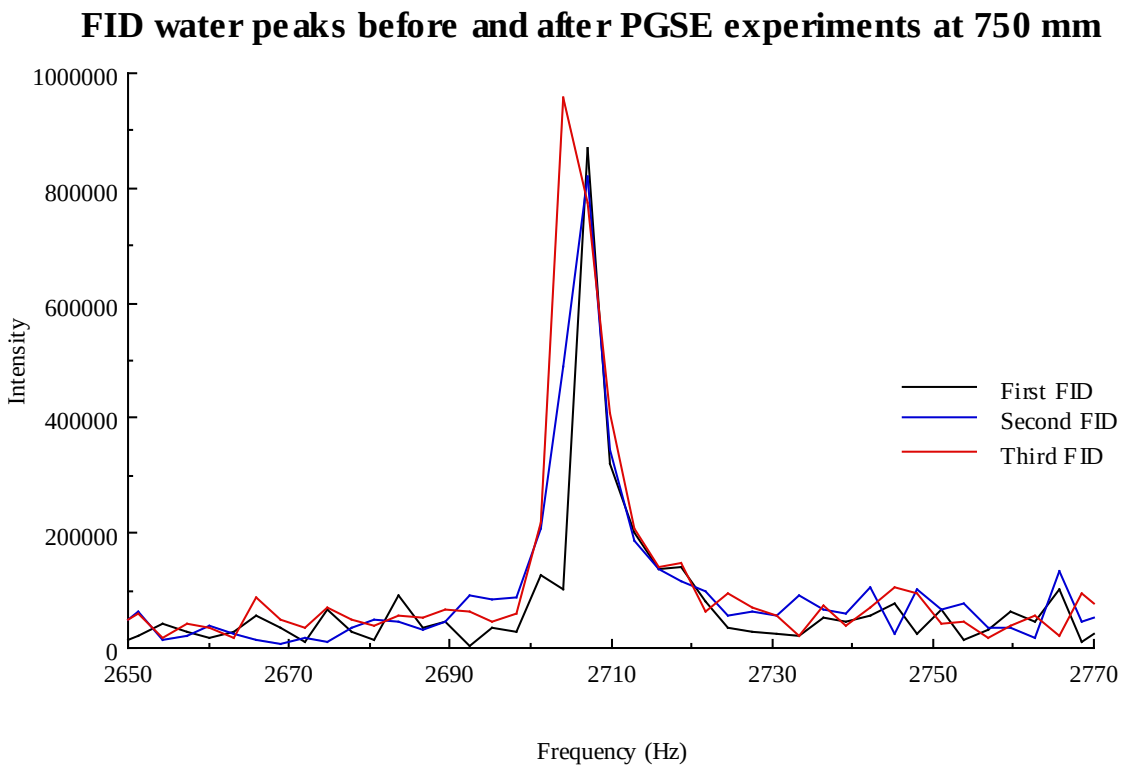

Figure 69 The increasing magnitude of the water peak over the period of the experiment.

5.1.4 FID discussion

The water content of the sea ice (4% at 750mm and 3% at 1100mm) correlates well with known results [55 & 56]. The theoretical calculations using the salinity found at similar depths and temperatures in earlier years, give a brine volume of approximately 3.5%. The liquid fraction of the samples is also similar to that found in earlier studies [12]. The FIDs shown in figure 69 indicate that there is only a small increase in water content over the period of the experiments. This implies that there is very little sample disturbance from the heating of the coils due to power dissipation.

5.1.5 Pulsed Gradient Spin Echo (PGSE) results

The PGSE experiments were first carried out at varying depths. However, initial results failed to obtain a satisfactory signal-to-noise ratio, so data from many experiments were combined. Two depths, 750mm and 1100mm, were chosen, and the data from all the experiments at these depths were combined.

Figure 70 shows the decay curve for pure water. If the gradient fields were homogenous this graph would be a straight line. The data is used to determine the gradient profile and so compensate for the gradient field inhomogeneities (see section 3.2.1). Figure 71 shows the gradient profile obtained, and figure 72 shows the diffusion rates obtained with two different water samples. The one labelled 'water' was the one used to determine the gradient profile.

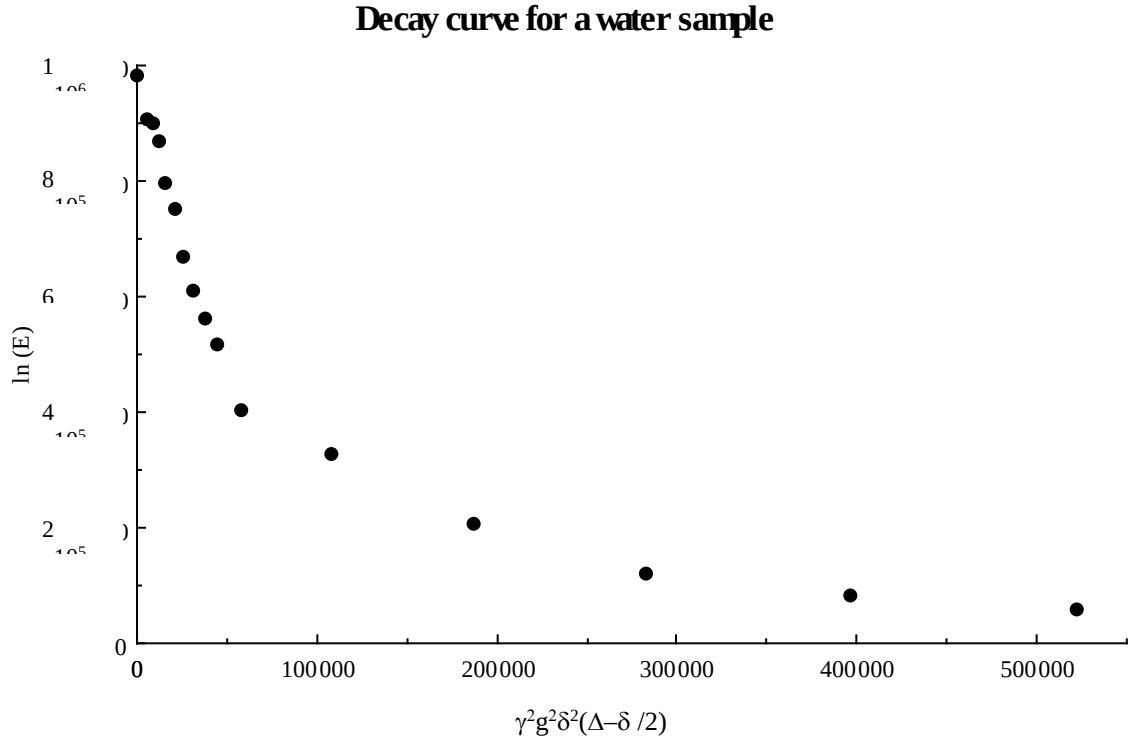

Figure 70 The decay curve for a water sample.

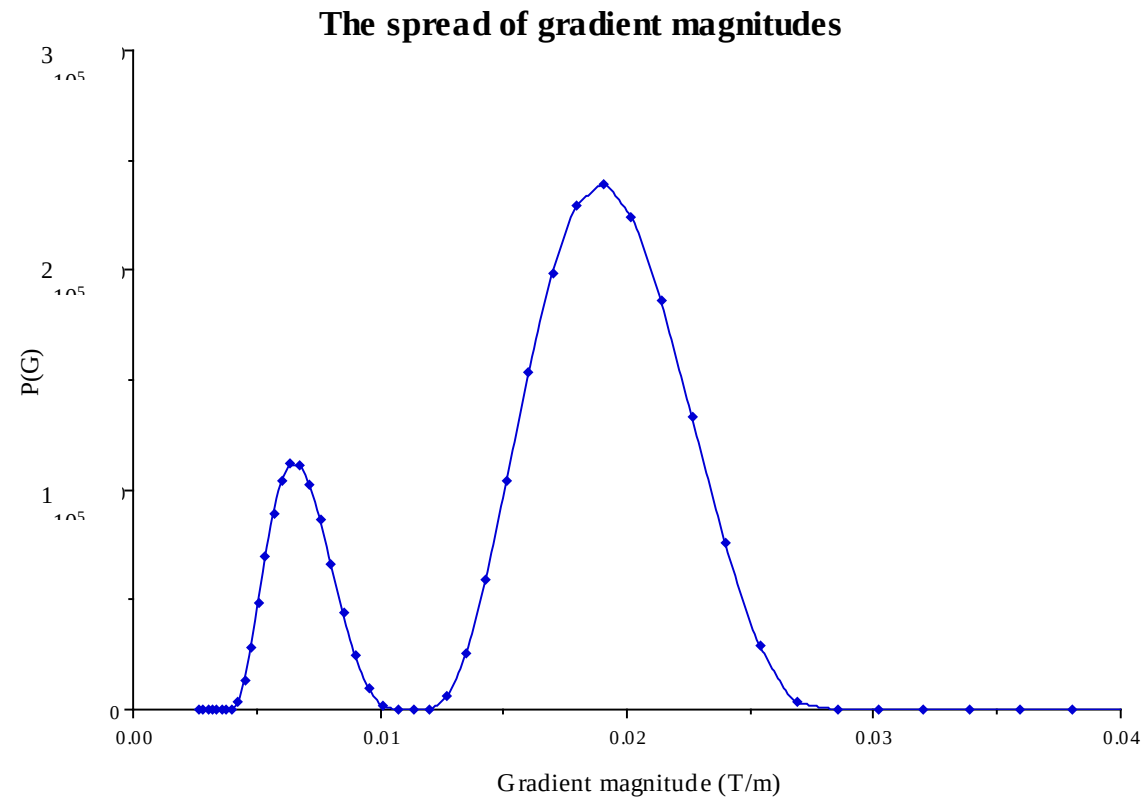

Figure 71 The coils' gradient profile (I=1.45A).

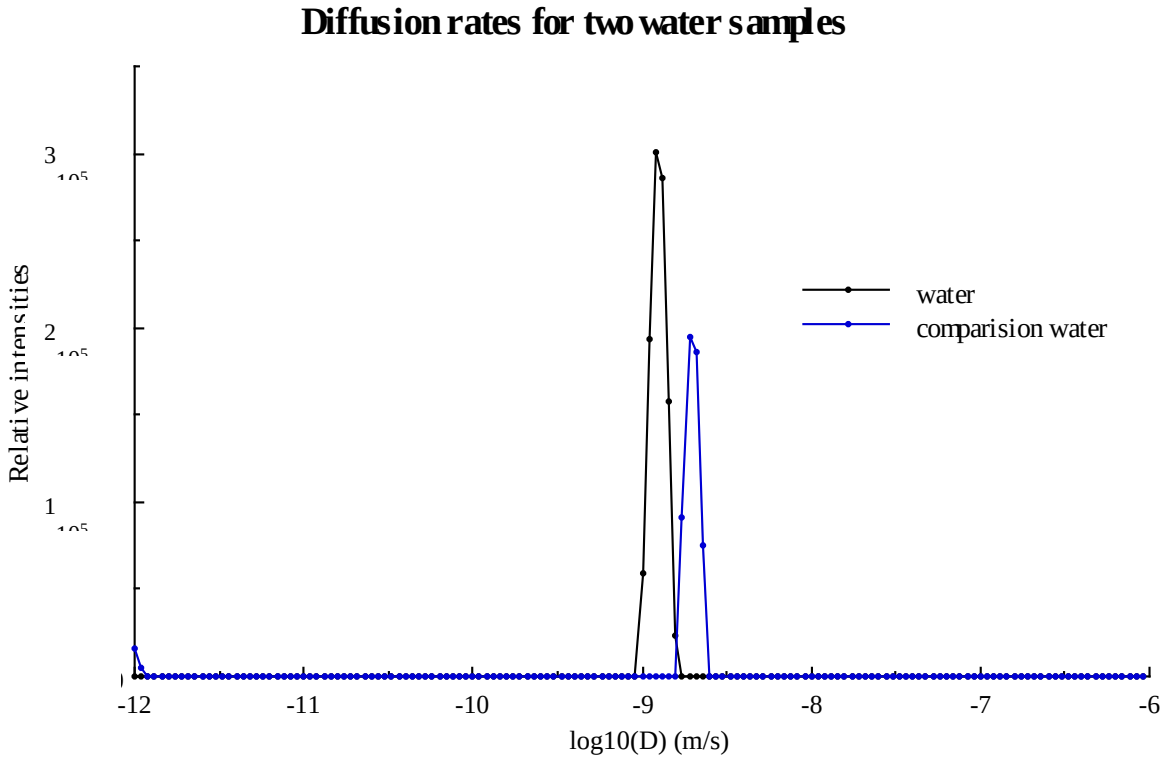

Figure 72 The diffusion rate for the water samples.

The single water peak at the expected diffusion rate for free water shows that the computer program accurately compensates for the inhomogeneous gradient field. The second water sample used as a further software test was at a different temperature to the first water sample. The water samples cooled and froze very rapidly in the Antarctic atmosphere, thus causing the temperature changes between experiments. This is the probable cause of the slight shift in peak position, as the natural diffusion rate of water decreases with a lowering of temperature [12].

Figure 73 shows the normalised decay curve of the water compared to the sea ice data. The faster original decay of the sea ice signals, indicate a faster diffusion rate than water, and the slower decay at the higher gradient values indicate a diffusion rate slower than water. Figure 74 shows the diffusion peaks calculated from this data, for the two different depths of ice cores and the water sample. The sea ice peak heights have been normalised. The graph clearly shows a diffusion rate faster than the self diffusion rate of water, and also a diffusion component slower than that of water.

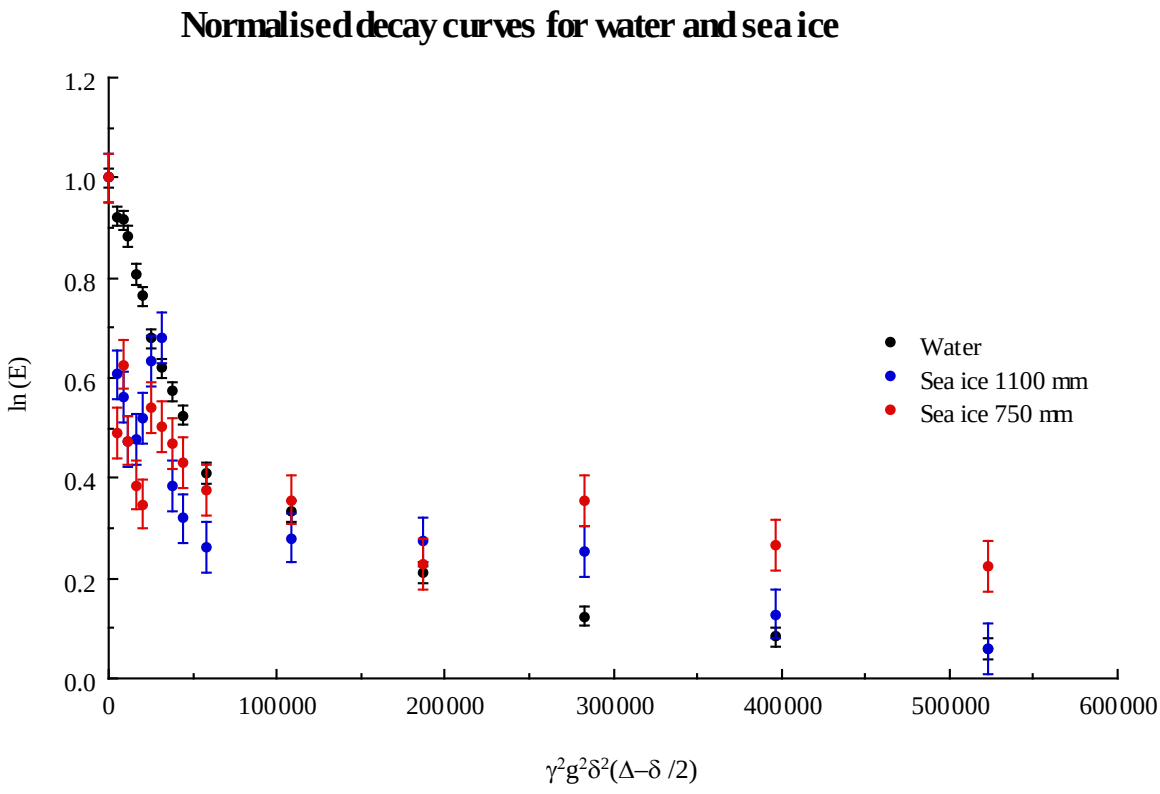

Figure 73 The normalised decay curves for sea ice and water.

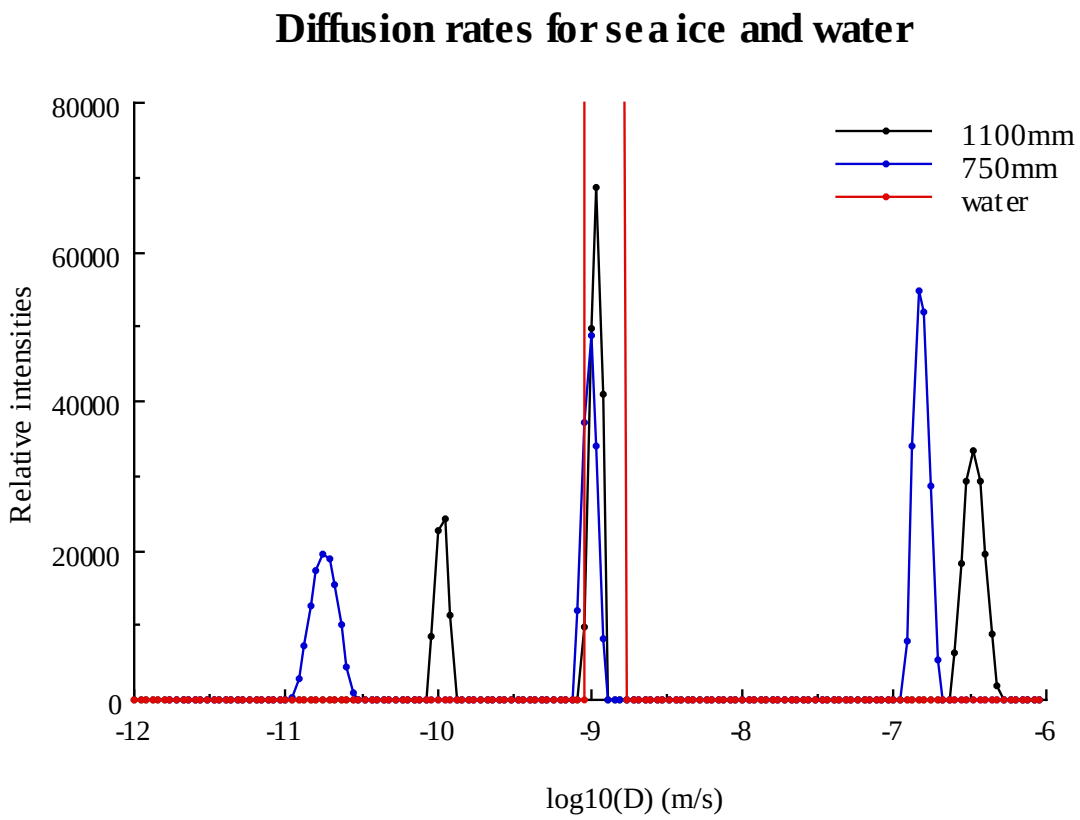

Figure 74 The diffusion rates for sea ice and water.

5.1.6 PGSE discussion

Although the decay curves for the ice samples are noisier than for the water sample, the initial decay is consistently faster than that of water, and levels out consistently faster than forwater. Thus indicating diffusion coefficients faster and slower than the self diffusion rate of water. These results are confirmed by figure 74 which clearly shows fast and slow diffusion peaks for both ice depths. Both ice depths have a liquid component that is diffusing at the known rate for water, as well as the fast component expected from the Raleigh convection, and a slow diffusion component, presumably caused by restricted diffusion in the very small brine pockets.

The diffusion rates which correspond to the self diffusion rate for water are slightly slower than that of the water sample. The colder ice (750 mm deep) has a slower self

diffusion rate than the warmer (1100mm deep) ice. This corresponds with known results [12], that show that the lower the temperature of the brine the slower the self diffusion rate.

The relative amount of brine with the self diffusion rate of water, is greater in the warmer, deeper sample. This follows predictions [3] that the ice crystal and pore sizes increase with depth into the ice sheet. The larger number of very small pores in the 750mm deep ice cause an increased amount of restricted diffusion compared to free self diffusion, within the ice.

5.2 Inside-out probe results

Due to unforseen time constraints, thorough testing of the inside-out probe was not completed in Antarctica. As the equipment had to be used away from the field camp (because of interference caused by the generator) the new portable NMR system had to be used. Unfortunately this equipment had not been used before and had many problems, including saving the data. Tests of the probe were therefore carried out back in New Zealand with water samples. The results of these tests were compared to results from the ice-core probe with a water sample, in the same conditions, and in the same geographic position, to enable a probe performance evaluation.

5.2.1 Signal-to-noise measurements

As the Earth's magnetic field strength varied a lot more in New Zealand than in Antarctica (due to the possible proximity of metal objects and geographical variations) a broader frequency spectrum filter was used. As can be seen in figure 75 however, the magnitude of the noise is very similar in New Zealand and in Antarctica. The root mean squared (rms) value of the noise in Antarctica is 985 units and in New Zealand is 1093 units.

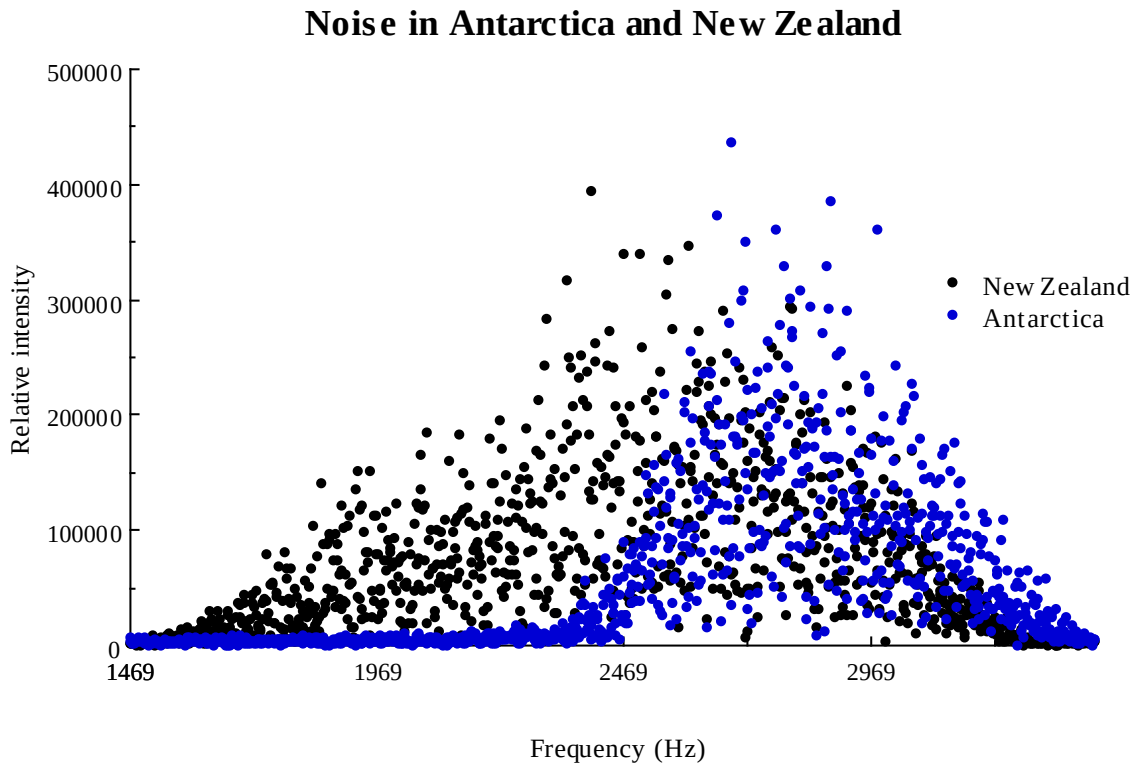

Figure 75 Noise in Antarctica and New Zealand.

The noise level for the inside-out probe was significantly higher than the noise level of the ice-core probe, as can be seen in figure 76. The experiments were carried out under the same conditions, in the same place, on the same day. The rms noise value was 555 units for the ice-core probe and 1093 units for the inside-out probe.

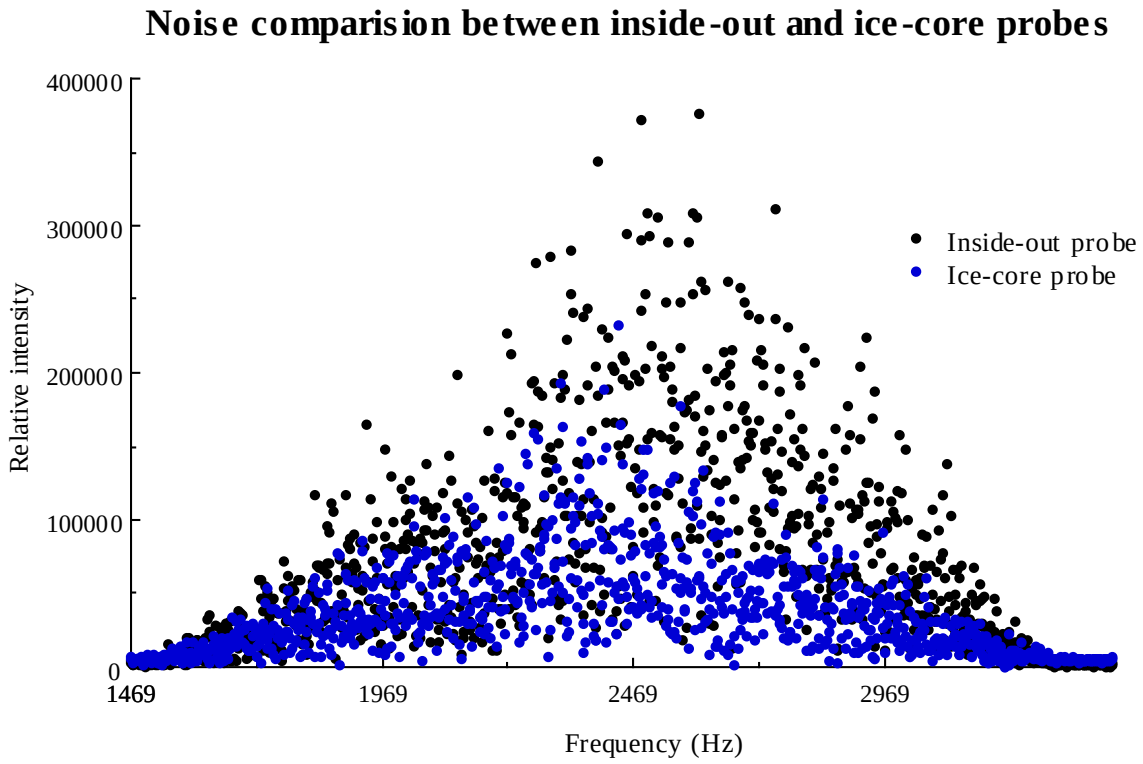

Figure 76 A noise comparison between the ice-core probe and the inside-out probe.

The experiments in New Zealand were carried out on two different days. The location was the same on both days. Both days were calm and fine but the second day had low cloud, whereas the first day had no cloud cover. The signal-to-noise ratio was significantly lower on the day with low cloud cover. While the background noise level did not change significantly, there were spikes in the time domain (see figure 79) that reduced the overall signal-to-noise ratio. This affected the inside-out probe to a much larger extent than the ice-core probe as can be see in figures 77 and 78.

For the inside-out probe the rms values were 1093 units on day one, and 2560 units on day two.

For the ice-core probe the rms values were 555 units on day one, and 767 units on day two.

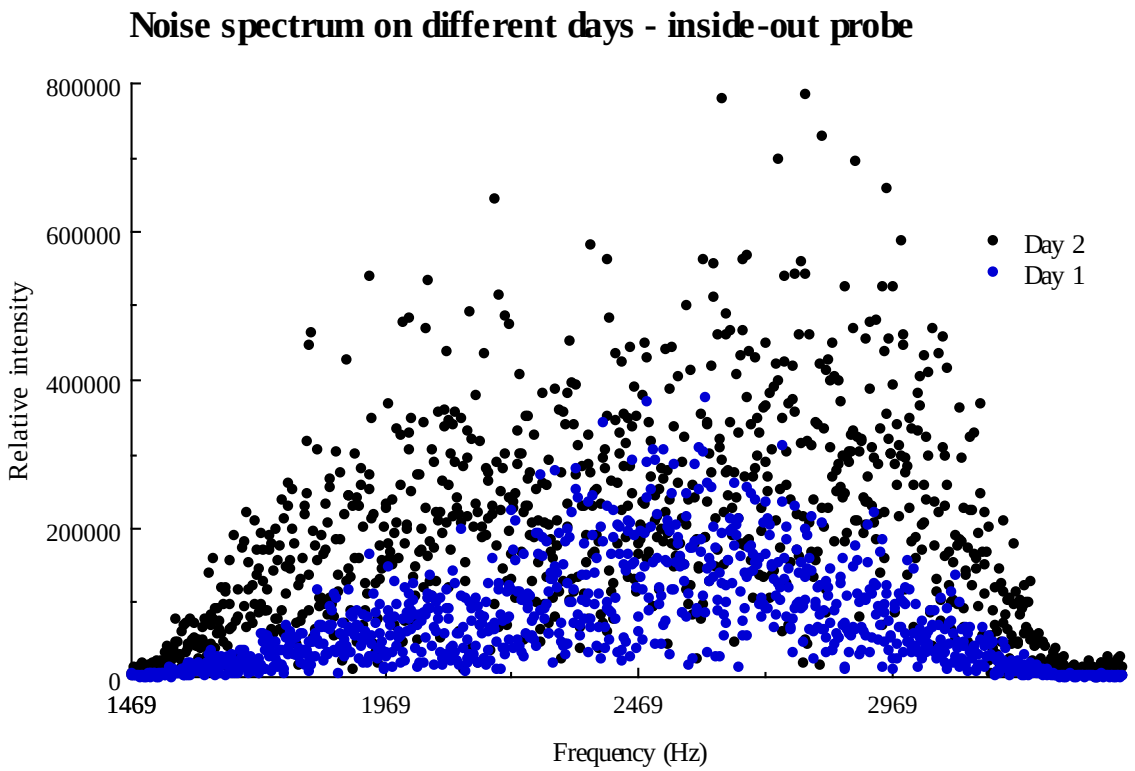

Figure 77 Noise from the inside-out probe on days one and two.

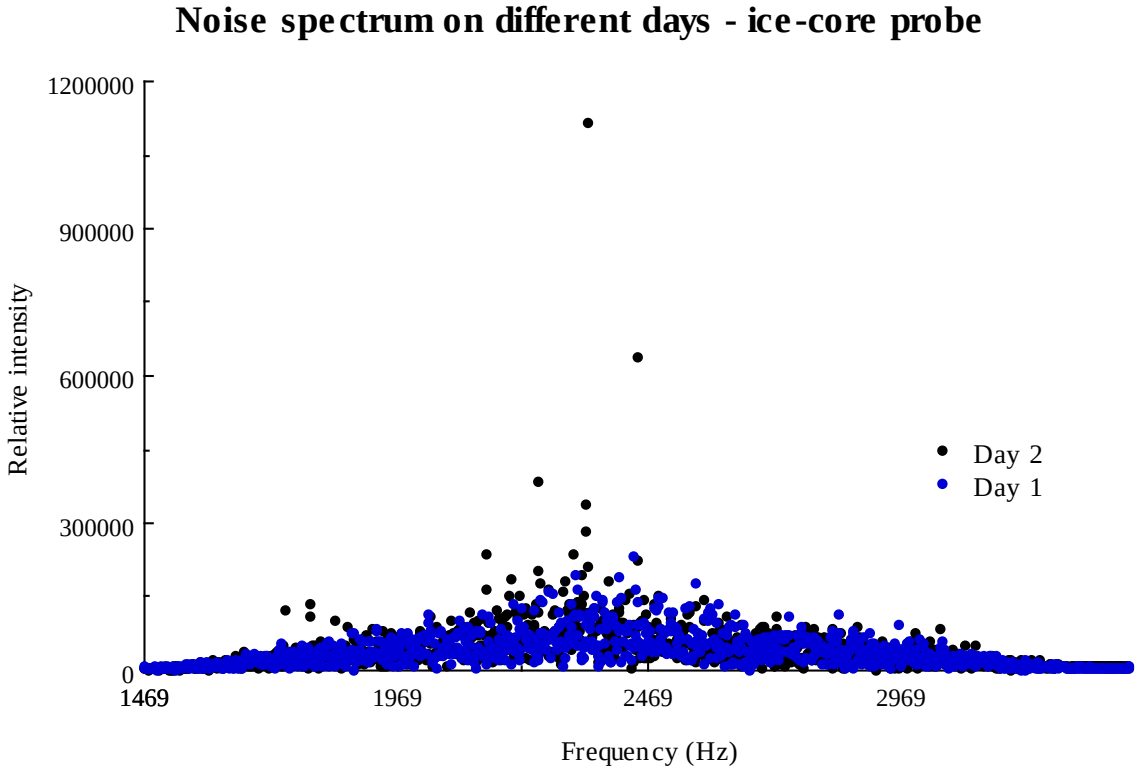

Figure 78 Noise from the ice-core probe on days one and two.

5.2.2 Noise comparison discussion

We managed to find a site in New Zealand that had external noise levels very similar to that experienced in the inside-out probe experimental site in Antarctica. On the first day of experiments it was found that the noise level observed by the inside-out probe was approximately twice as high as for the ice-core probe. The next day had a larger background noise level. This had a much greater effect on the inside-out probe than the ice-core probe, indicating that the inside-out probe is much more sensitive to external noise. The inside-out probe has a lower resistance at resonance (see section 3.3.4), and therefore will have a lower internal (Johnson) noise level. This implies that the inside-out probe can obtain similar noise levels to the ice-core probe if it is in a position with very low external noise. The experimental site used in Antarctica did not have very low external noise, it was in line-of-site of the field camp and McMurdo base, which was the probable source of this. Due to time constraints we were unable to try other sites (with an island between us and the field camp for example), to determine what the average background noise level in Antarctica was.

An observable difference in conditions between the two days of experiments in New Zealand was that the second day (which had much larger background noise) had low cloud cover while the first day had no clouds. We also noted that the last day of experiments in Antarctica was the only day with clouds, and we had higher noise values on that day. The cloud layer reflecting noise sources from other nearby areas could be a possible cause of the noise increase, and it would be interesting to test this theory.

5.2.3 FID experiments

A typical FID obtained from the inside-out probe with a water sample is shown in figure 79. The spikes were only present on the second day of experiments. Apart from these spikes the FIDs looked very similar from day to day.

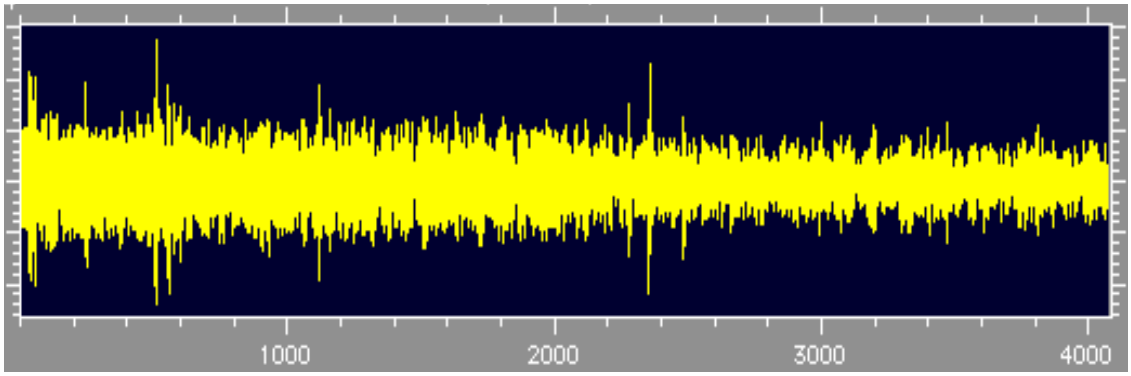

Figure 79 A typical FID obtained from the inside-out probe on day two (32 scans).

Two different sized water samples were used to determine where the majority of the signal was coming from. The small water sample filled the area between the probes legs (see figure 80), while the larger water sample surrounded the probe's legs (see figure 81). The results (see figure 82) show a signal strength of 2.4×10^4 units for the small water sample and 3×10^4 units for the large water sample. The shift in frequency of the water spike is due to a slight shift in position, and so magnetic environment, between experiments.

The rest of the experiments were conducted with large water samples.

Figure 80 The small water sample experiment set up.

Figure 81 The large water sample experiment set up, the copper drum is filled with water.

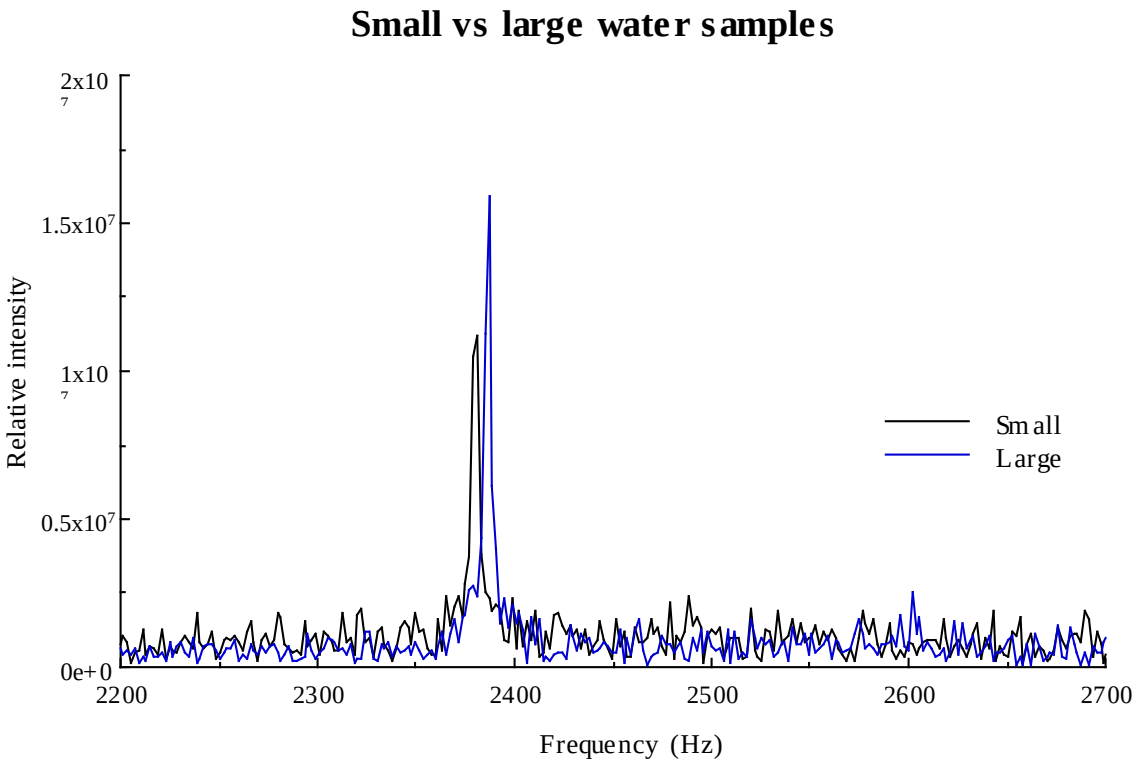

Figure 82 The water peaks from the small and large water samples

The results from using the alternative polarisation coils (see section 3.3.4) in the vertical and horizontal orientations are compared with the results obtained when using the probe's own polarising coils in figure 83. In each case there were 24 scans per experiment.

The signal strengths obtained were; 3 x 10^4 units for the probes own polarisation coils, 2 x 10^4 units for horizontal orientation of external polarisation coils, and 2.6 x 10^4 units for vertically orientated polarisation coils.

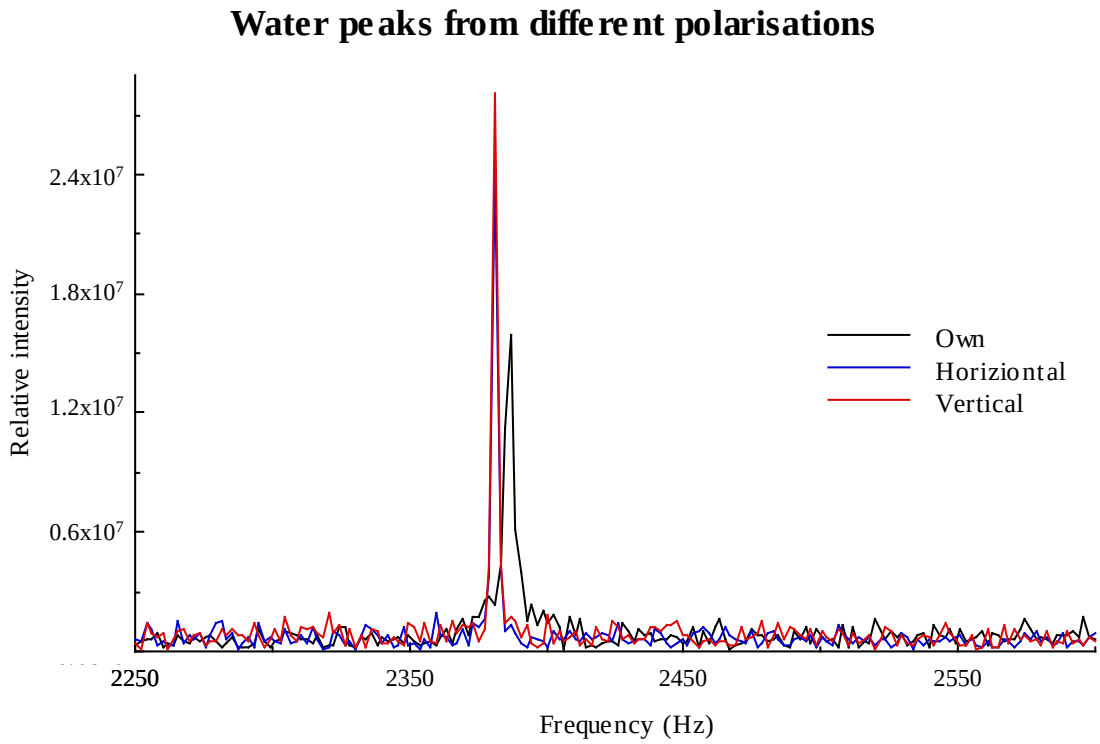

Figure 83 The water peaks in the frequency spectrum for the different polarisations.

The experiment using the probe's own polarisation coils was done in a slightly different position to the other experiments, thus resulting in the frequency shift of this water peak.

A typical spectrum from the ice-core probe after one scan is shown in figure 84. This has a signal magnitude of 1.6 x 10^4 units.

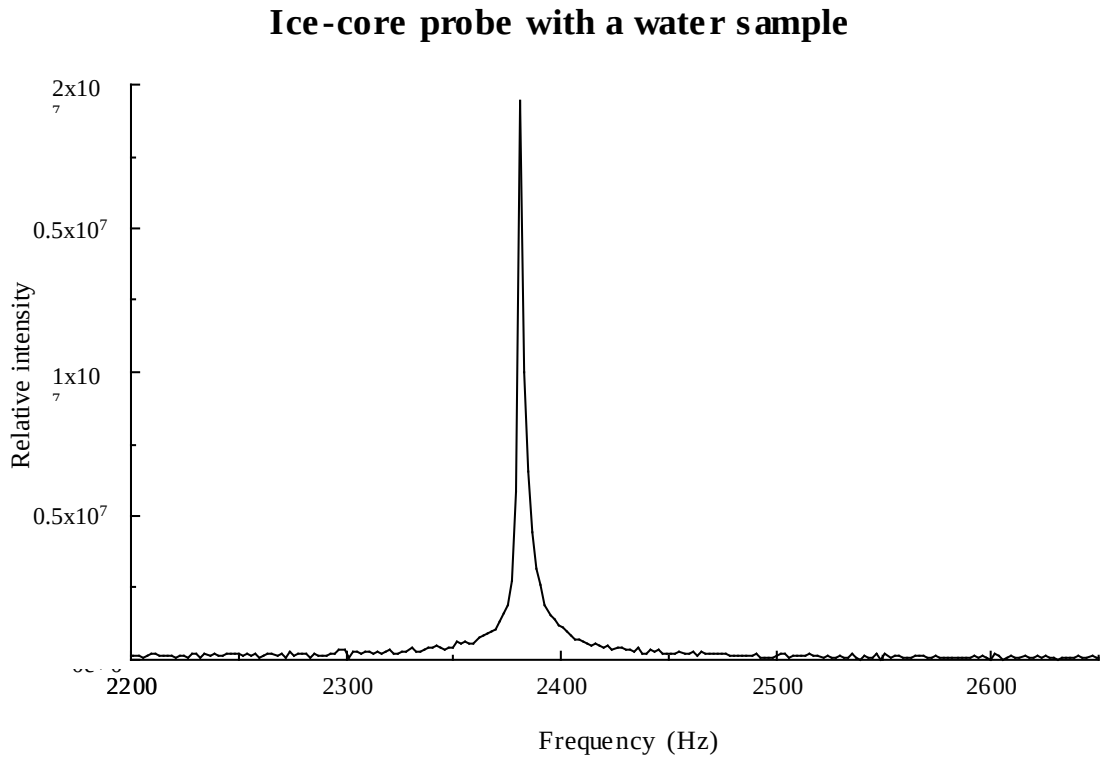

Figure 84 The frequency spectrum from the ice-core probe with a water sample (one scan).

Signal strength increases monotonically with the number of scans, while the noise power increases with the square root of the number of scans.

Thus to obtain the same signal strength from the inside-out probe as the ice-core probe has, we need 12.8 times as many scans. However, to obtain the same signal-to-noise power as we had in Antarctica with the ice-core probe, we would need 305 scans. ☹

5.2.4 Signal magnitude comparison discussion

The results from using the different sized water samples indicate that up to 80% of the signal comes from the region between the probe's legs.

The tests using different polarising coils and coil configurations, show that there is no improvement in signal strength resulting from having larger polarising coils on the surface of the ice, or parallel to the legs of the probe. The greatest signal strength was obtained when using the probe's own polarising coils. The best way to improve the polarisation therefore, would be to use two batteries instead of one, thus having twice the current in the polarising coils, and approximately double the signal strength. I do not believe that this would cause excessive heating of the coils. There was no significant heating of the coils when only one battery was used, and the air cooling system set up to direct cold air onto the polarising coils (see section 3.3), was not used.

To obtain the same signal-to-noise ratio as the ice-core probe, with the inside-out probe, we would need to use two batteries, and have a factor of 8.7 reduction in the background noise level. Alternatively, one could do ten tines as many scans and have a background noise reduction factor of 2.7. I believe that this is a realistic possibility.

Chapter 6

LAB WORK RESULTS

The sample used was a cylinder of ice with a height of 50 mm and a radius of 12 mm. The base of the ice was held at -10.0^0C and the top was varied from -11.2^0C to -12.2^0C. The images shown are 15 mm x 15 mm, with a resolution of 8.5 pixels/mm.

6.1 Image results

6.1.1 Two dimensional image results

The images showed clearly a wide range of brine pocket sizes as shown in figure 85. The small blue dots are small amounts of brine and not noise as they show up repeatedly in all the images.

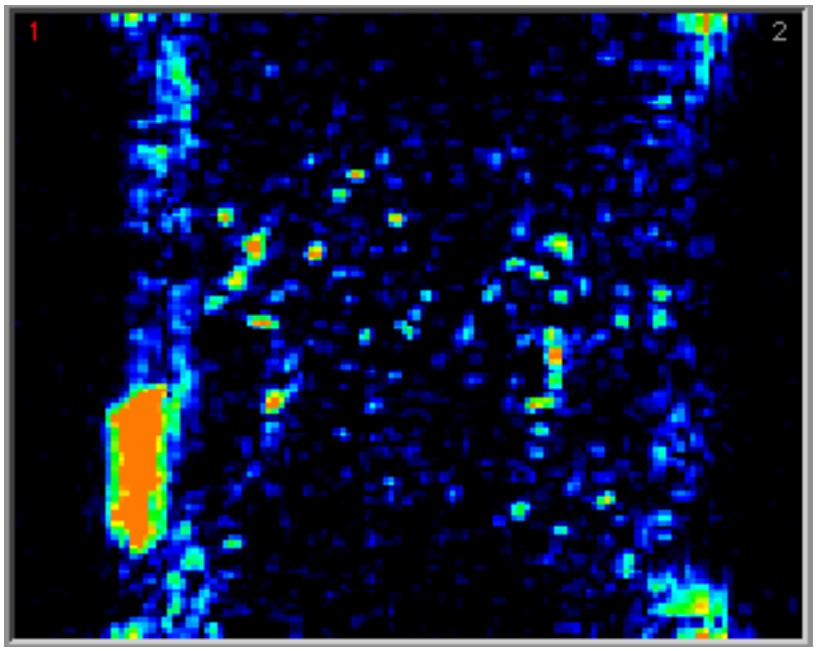

Figure 85 A 15mm x 15mm image of a slice vertically through the centre of the ice sample.

Individual pockets were mapped over a period of time to observe their translational motion. Three different temperature gradients were used 0.3^0C/cm, 0.4^0C/cm, and 0.5^0C/cm. An image was taken once the temperature gradient had reached equilibrium, and then again after 2 hours. Columns from the same position in consecutive images were compared to track the movement of individual brine pockets.

The rate of movement through the ice sample was, averaged over 21 brine pockets, 0.02mm per hour.

There was no significant change in rate of movement between different sized brine pockets.

Figures 86 and 87 show the movement of a large brine pocket, while figure 88 shows similar movement in a small brine pocket.

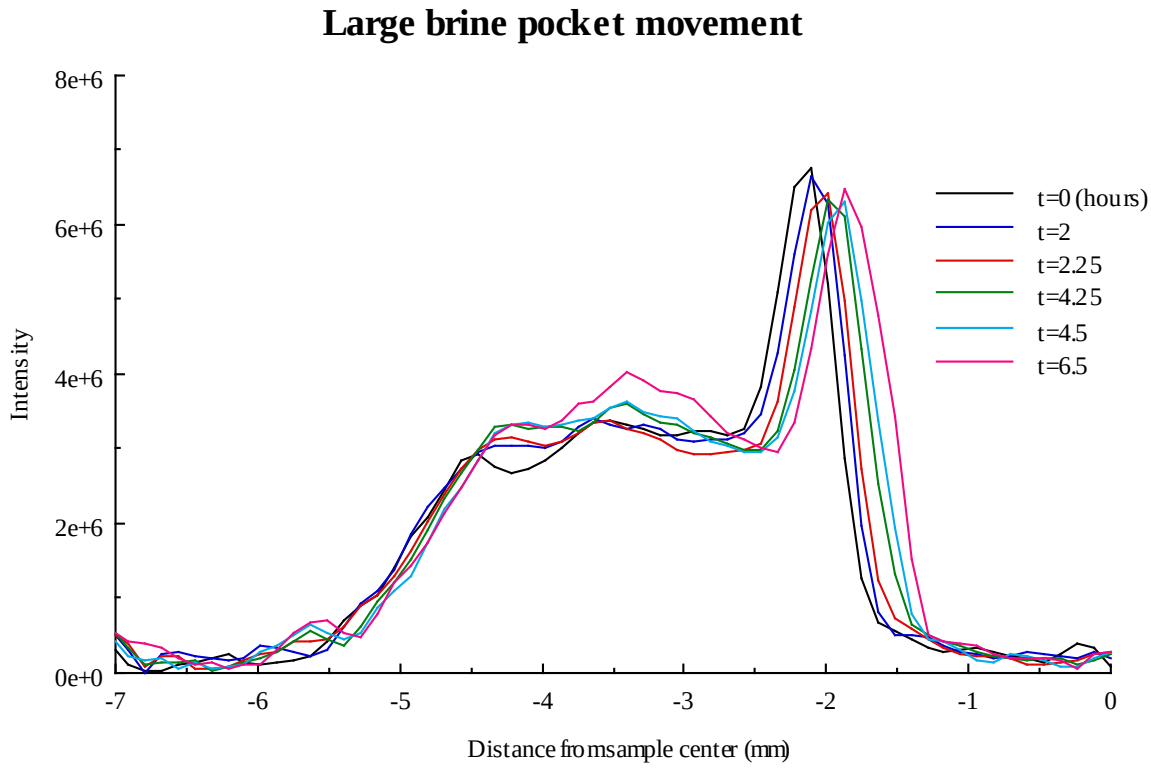

Figure 86 A large brine pocket's position over a period of 6.5 hours.

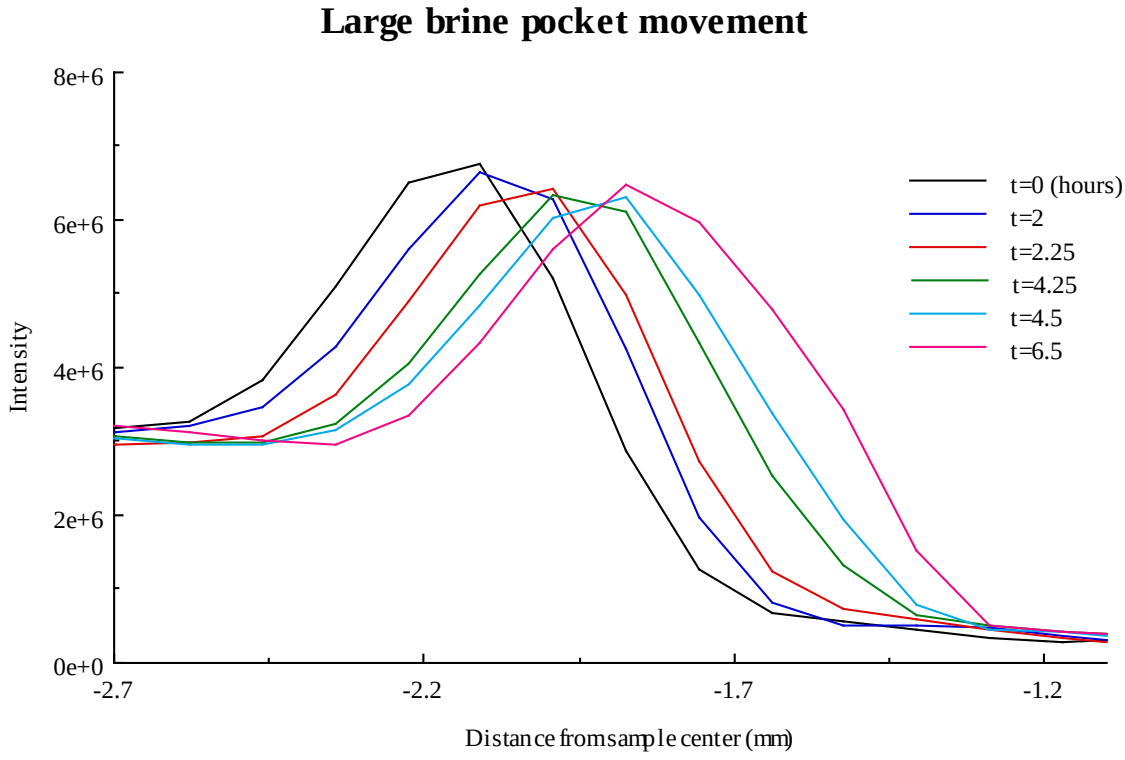

Figure 87 An enlarged portion of a large brine pocket's position over a period of 6.5 hours.

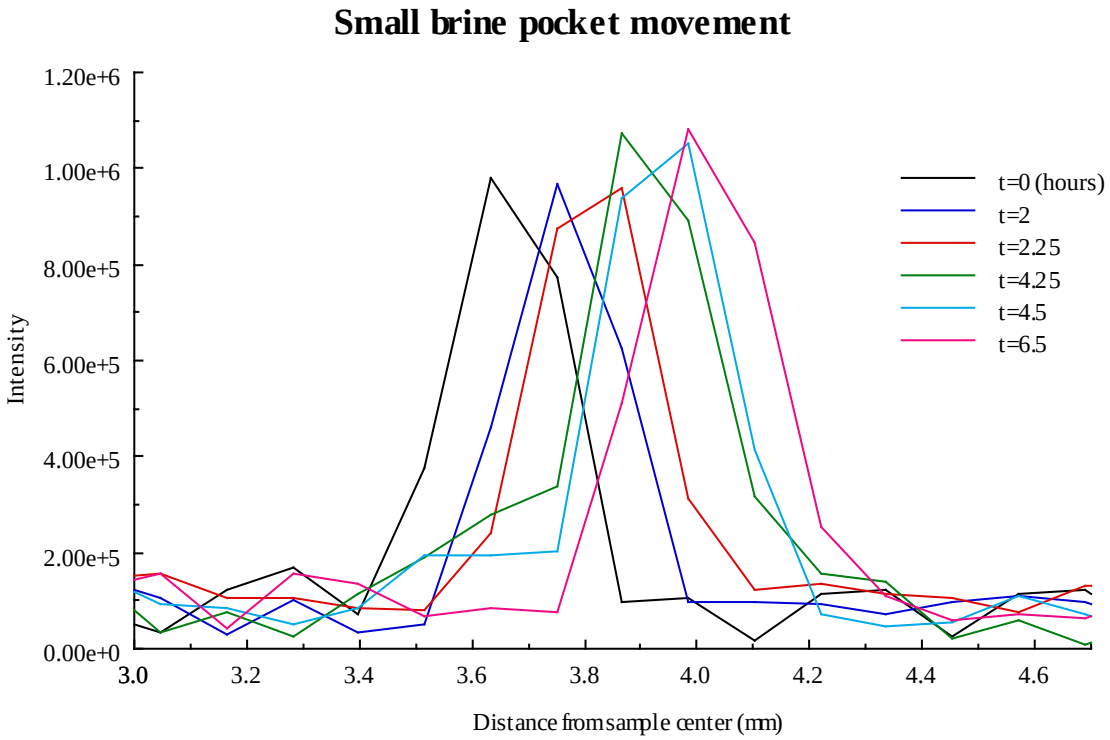

Figure 88 A small brine pocket's position over a period of 6.5 hours.

There was no significant difference in rate of movement for the different temperature gradients, this could have been due to the lack of resolution. As each peak generally only had four or five data points it was very difficult to determine the exact shift of each peak.

The brine pockets' movement can be seen on the series of images below (figure 89). The front image taken at time 0, the last 6.5 hours later, enables a small downward movement to be seen.

6.1.2 Three dimensional image results

The three dimensional image showed a range of brine pocket sizes relatively evenly distributed throughout the ice sample as can be seen in figures 90 and 91. There were some larger pockets near the edge of the sample, consistent with studies (see section 2) showing larger brine pockets in ice crystal boundaries.

The image was analysed in PROSPA [53] where it could be viewed in three dimensions and rotated to observe any particular area of the sample. This was done and showed that there were no unusual defects in the sample. The three dimensional image can be viewed in the demo for PROSPA.

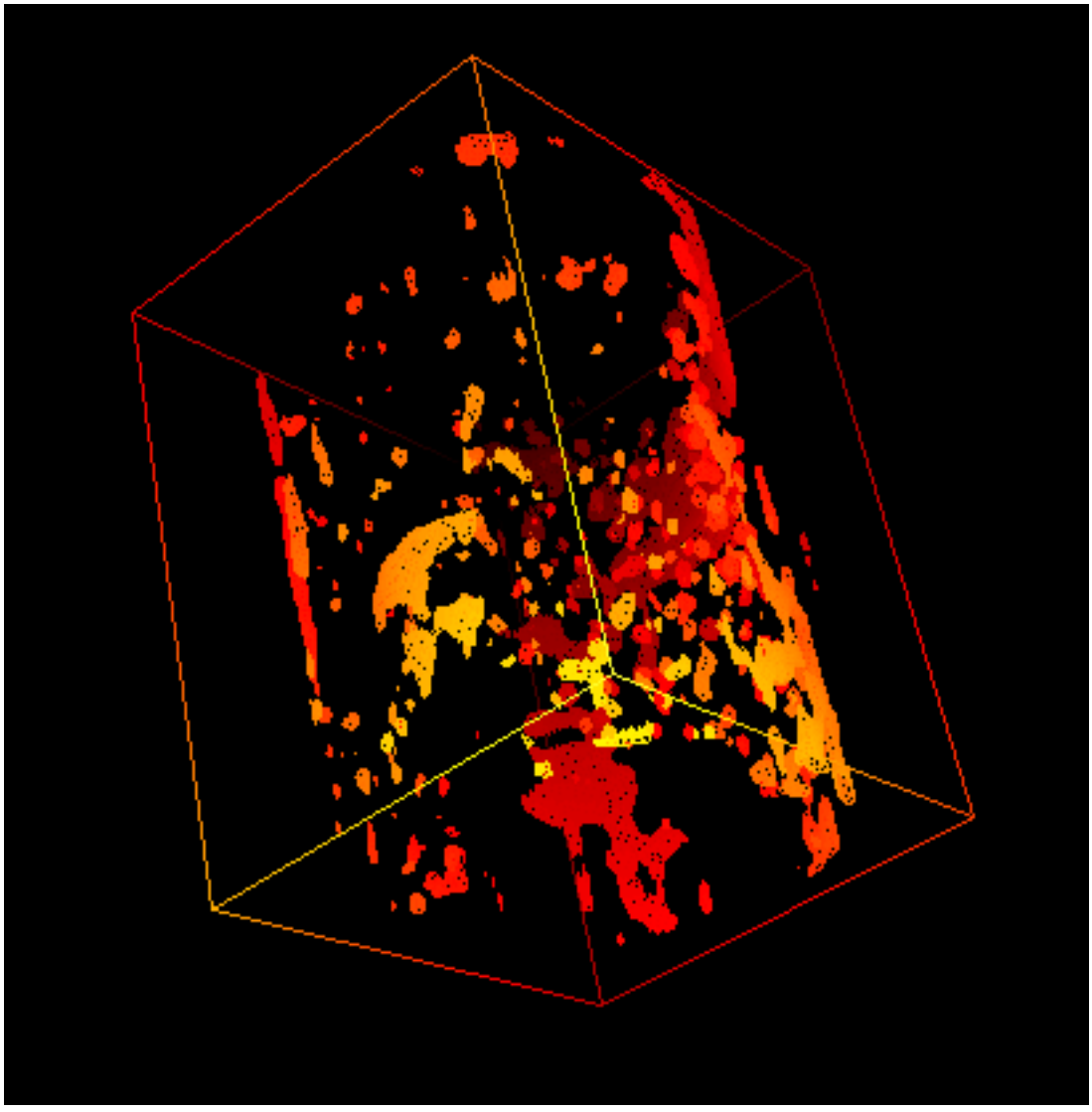

Figure 90 A three dimensional image of the ice sample, showing a variety of brine pocket shapes and sizes. The sample is tilted to enable the best view of the brine pockets.

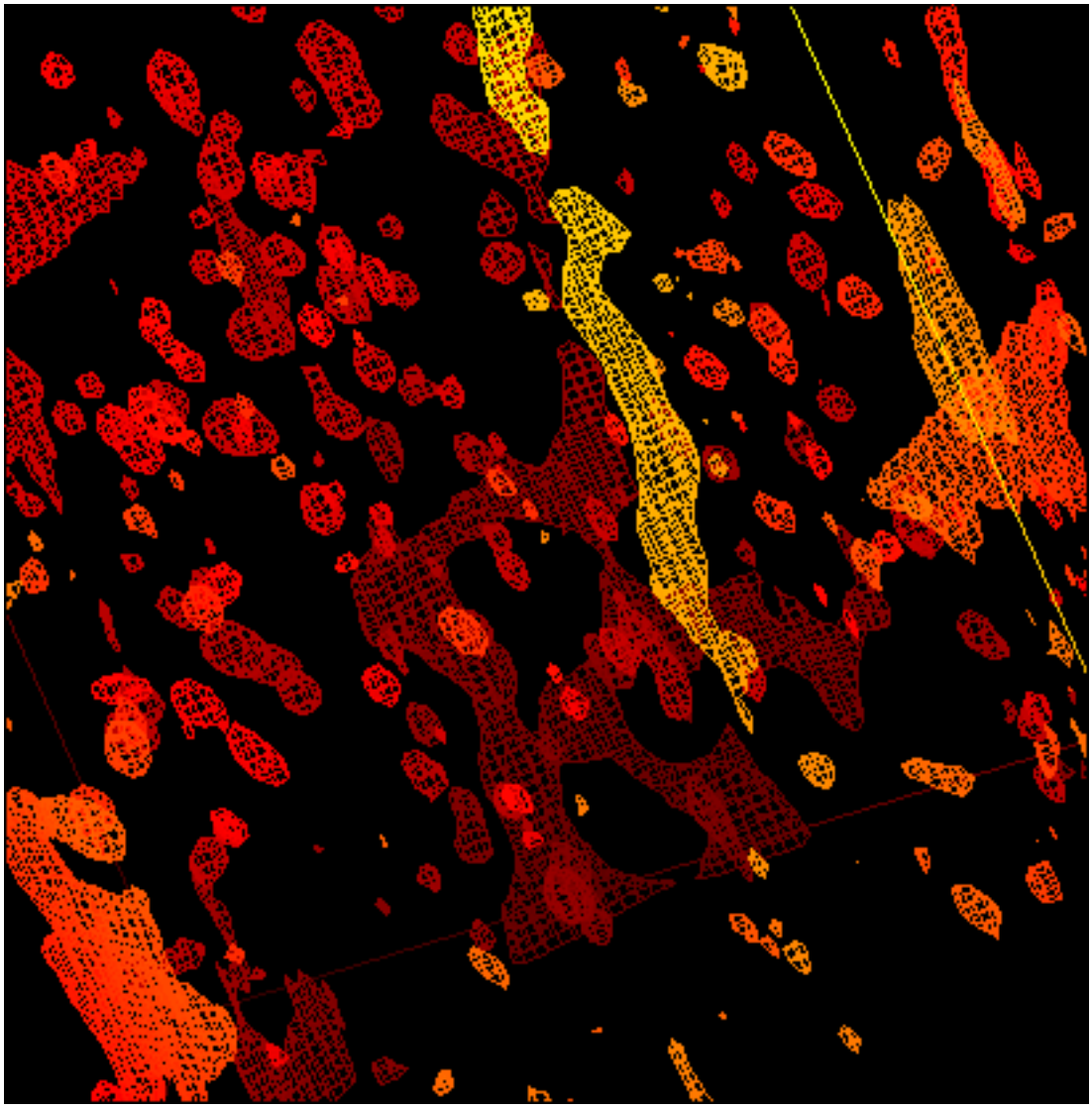

Figure 91 A close up picture of part of the ice sample, showing a variety of brine pocket shapes and sizes. NB the sample is tilted by the same angle as shown in figure 90.

It was noticed that throughout the whole sample the brine pockets that were elongated tended to be elongated in the z-direction.

The pictures above only show the larger brine pockets, to show smaller ones as well was too memory intensive for the computers used.

6.1.3 Image discussion

The brine pockets clearly shift in the direction of the temperature gradient, this is in good qualitative agreement with the theory as discussed in section 1.4. To determine the change in rate of movement, higher resolution data, over a longer time period, would be needed. I believe that the increase in resolution needed, would be a factor of four. This increase in resolution would need 16 times more data points and 16 times more scans to obtain the same signal level. However, as the noise level would also increase with the number of scans, to obtain the same signal to noise level 256 scans would be needed. The experiments need to be done as quickly as possible to prevent significant movement of the brine pockets while the image is being taken. Therefore a much smaller part of the ice sample would have to be imaged. A difficulty with doing experiments over a longer time period would be keeping the sample stable over the extended period of time. The dewar of liquid nitrogen needed for sample cooling only lasts for approximately 8 hours before it needs refilling, and during the refilling process the sample will start to warm up, causing possible configurational changes to the sample. If this is repeated often it may create difficulties drawing accurate comparisons between images.

The three dimensional image showed that the artificial sea ice grown was a realistic replica of natural sea ice. It had a good distribution of realistically sized brine pockets throughout the sample volume, most of which, if elongated, were orientated in the vertical direction, as in natural sea ice.

6.2 Diffusion results

6.2.1 Whole sample diffusion results

The results from the PGSE experiments showed a fast diffusion rate in the x-direction and a slower diffusion rate in the y- and z-directions. This was consistent for all three different temperature gradients. The z-direction was in the vertical direction, the temperature gradient was also in this direction. The results obtained are as follows:

Temperature gradient of 0.3^0C/cm

Diffusion matrix in local axis frame:

2.35	0.00	0.00
0.00	0.45	0.00
0.00	0.00	0.58

Rotation matrix:

0.99	0.16	-0.05
-0.17	0.91	-0.37
-0.01	0.37	0.93

Temperature gradient of 0.4^0C/cm

Diffusion matrix in local axis frame:

2.32	0.00	0.00
0.00	0.41	0.00
0.00	0.00	0.59

Rotation matrix:

0.98	0.17	-0.07
-0.19	0.91	-0.38
0.00	0.38	0.92

Temperature gradient of 0.5^0C/cm

Diffusion matrix in local axis frame:

2.06	0.00	0.00
0.00	0.41	0.00
0.00	0.00	0.59

Rotation matrix:

0.99	0.09	-0.08
-0.10	0.98	-0.16
0.07	0.17	0.98

6.2.2 Diffusion tensor results

The data obtained for the diffusion tensor images was not good. A series of 8 images, each with progressively stronger gradients, were taken. The expected result would be to observe the intensity of the diffusion image decreasing, with increasing gradient magnitude. The rate of decrease is determined by the brine diffusion coefficient.

The images we obtained did show this expected decrease in intensity, but also showed a twisting of the image with increasing gradient magnitude. An example of this is shown in figure 92, where the two main brine pockets clearly undergo a clockwise rotation around the centre of the image. All parts of the image appeared to undergo this rotation, which is much easier to see interactively on the computer. The image below shows the rotation observed with a y-direction gradient, the other gradient directions also produced apparent rotations of the image, but not always in the same plane.

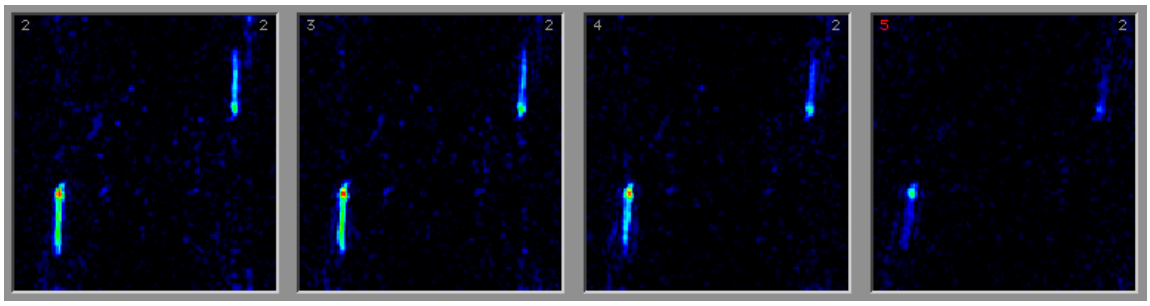

Figure 92 Each image is a 15mm x 15mm image of a slice vertically through the centre of the ice sample with progressively increasing y-direction gradients showing brine pocket rotation.

When the diffusion tensor analysis was done on the above images the result shown in figures 93 and 94 were obtained. The figures show intensity plots of the gradients in the local x- y- and z-directions (see section 4.5). I do not believe these results are valid. The twisting of the images would cause the intensity in some positions in the image to increase with gradient, and in other positions the brine pockets shifting would appear to be quickly decaying intensity, so giving an unrealistically fast diffusion rate.

The following images will therefore be showing a combination of diffusion rates and image rotation rates.

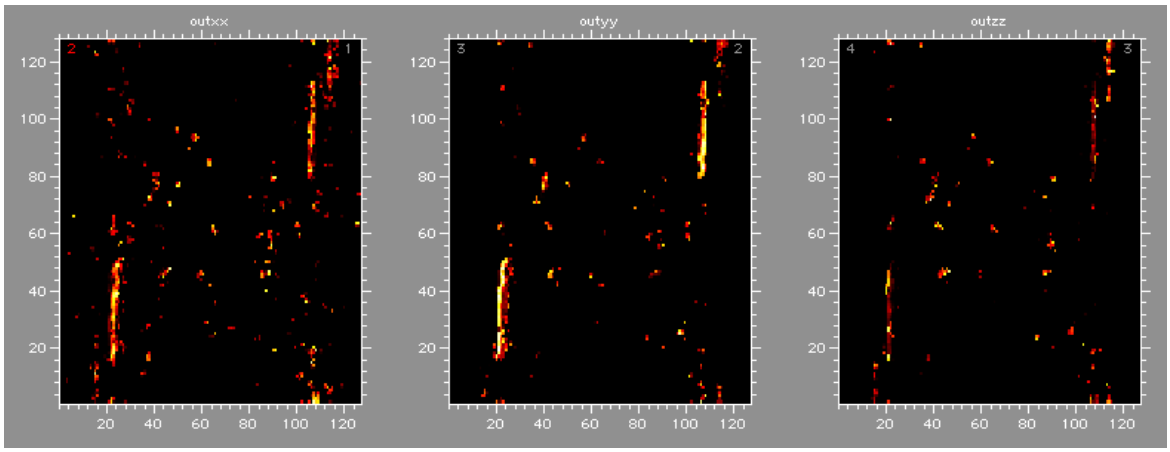

Figure 93 A diffusion intensity plot with the smallest applied temperature gradient.

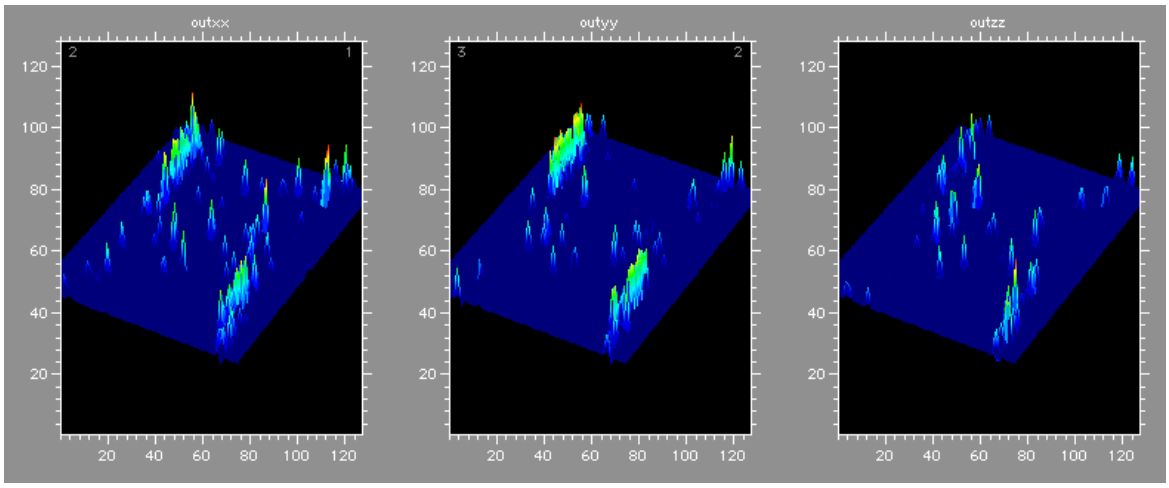

Figure 94 Another representation of the diffusion intensity plot shown in figure 91.

The images for all the different temperature gradients were similar, although the peak diffusion rates slightly increased with increasing temperature gradient. In all cases the y-direction had the highest diffusion rates, and the x-direction had the most brine pockets showing diffusion.

6.2.3 Diffusion discussion

The fast diffusion rate is in the x-direction in the PGSE results, yet the fastest diffusion rates appears to be in the y-direction in the diffusion weighted images. There are however, a lot more diffusion peaks showing up in the x-direction of the diffusion weighted images. This could indicate that the majority of the signal comes from very small brine pockets but it is hard to draw any definite conclusions without first confirming the experimental results.

A possible cause of the apparent rotation of the diffusion weighted image slice could be an artefact of the experiment's pulse sequence. If the gradient pulse is too close to the slice selection pulse the Eddy currents caused by the gradient pulse could add to the slice selection pulse, causing the observed slice position to change with varying gradient strengths.

Chapter 7

Conclusions

7.1 Field work

Earlier work in Antarctica has been done using probes that obtained a much clearer signal from the sample but at the expense of the sample quality. In general the better the signal the more disturbed the sample. The trick is to find the happy medium. In 1999 we took two probes to Antarctica. The ice-core probe's greater compactness required much less surrounding ice to be removed, and markedly decreased the amount of time for an experiment, thus reducing the sample disturbance, but requiring the inhomogeneous gradient field to be analytically compensated. The other (inside-out) probe had an almost totally undisturbed sample, but at significant expense of signal quality.

The ice-core probe's experimental results on pure water are used to determine the inhomogeneous gradient distribution. The distribution is in good agreement with that calculated by a Biot-Savart analysis taking into consideration the local B_1 sensitivity effect. When this gradient distribution is used to analyse the uniform diffusion rate of a water sample, a single diffusion coefficient with the expected value for free water (water with unrestricted diffusion) is obtained. This shows that the inhomogeneities of the gradient field were being accurately compensated. Using this analysis on data obtained at two depths of ice, three diffusion components were observed. They corresponded to a peak with the expected diffusion rate of free water, a faster than free water diffusion coefficient and a slower than free water diffusion coefficient. All the results obtained correlated well with those predicted by the theory and observed in past research.

I conclude therefore, that the data clearly shows a diffusion rate much faster than the self diffusion rate of water, correlating well with the expected diffusion rate from Rayleigh convection, while being consistent in all other ways with the results obtained in the 1995 and 1997 studies [12 & 24].

It would be valuable to continue this work doing experiments over a wide range of depths, to obtain a clear picture of the relationships between brine volume, temperature, pore size, and diffusion rates.

The testing of the inside-out probe showed that although good signal strength was obtained the probe was highly sensitive to external noise sources. The tests of external polarisation coil configurations and orientations showed that the internal polarising coils that I designed as part of the probe produced the best signal. The tests showed that with the power supplies used, and in the position that it was tested in in Antarctica, the signal-to-noise ratio was not high enough to do PGSE experiments. If however, a position with a lower external noise was found (possibly a site not in line-of-site of generators and broadcasting equipment) and an extra battery was used, I believe it would be possible to obtain a satisfactorily high signal-to-noise ratio to enable PGSE experiments to be conducted. If this was done it would be a useful confirmation of the accuracy of the ice-core probe results.

7.2 Lab work

It has been shown that it is possible to construct a special NMR probe incorporating temperature control, and temperature gradient control in which gradients of up to $\pm 2^0$C/cm could be maintained.

Both large and small brine pockets clearly shift in the direction of the temperature gradient in the observed sample. This result is in good agreement with Rayleigh convection theory described in section 1. ☺ To observe the change in rate of movement with a change in temperature gradient, further experiments would have to be done as discussed in section 6.1.3.

Tests showed that the diffusion tensor software written accurately determined the orientation of the ice samples local axes system, and converted the diffusion rates obtained in the machine's axes system, into the local axes.

Although there was some correlation between the diffusion-weighted images and the whole sample diffusion rate, no definite conclusions could be drawn. This was due to the probable unreliability of the raw data. From the appearance of the data obtained, a likely cause of the problem could be experimental artefacts due to a problem with the pulse sequence. To test this a dummy sample with known diffusion rates differing

between different directions would have to be used. If the gradient pulse was found to be effecting the slice selection pulse, the pulse program would have to be rewritten. The dummy sample could also be used to test the PGSE sequence to confirm the results. I believe that this is necessary before any definite conclusions about individual brine pockets diffusion rates can be drawn.

I believe that this testing would be good work to continue with, but unfortunately it is beyond the scope of this Masters due to time constraints.

References

[1] S Nickol and I Allison, *American Scientist*, **85**, p426-488, (1997)

[2] G. Savidge, J Priddle, L. Gilpin, U. Bathman, E. Murphy, N. Owens, R. Pollar, D. Turner, C.Veth, and P Boyd, *Antarctic Science*, **8**, p349-358, (1996)

[3] Y. Doronin, and D. Kheisin, *Sea Ice*, p31-70, (1977)

[4] D. Perovich, and A. Gow, *Journal of Geophysical Research*, **101**, p18,327-18,343, (1996)

[5] A. Gow, S. Ackley, W. Weeks, and J. Govoni, *Annals of Glaciology*, **3**, p113-117, (1982)

[6] M. Jefferies, R. Shaw, K. Morris, A. Veazey, and H. Krouse, *Journal of Geophysical Research*, **99**, p985-995, (1994)

[7] Y. Wei, M. Johnston, and J. Dempsey, *Cold Regions Science and Technology*, **23**, p367-375, (1995)

[8] D. Cole, and L. Shapiro, *Journal of Geophysical Research*, **103**, p21,739-21,750, (1998)

[9] N. Wu, *www.norbertwu.com*, http://scilib.ucsd.edu/sio/nsf/gallery/index.html (1999)

[10] R. Wooding, *Proc. Roy. Soc. Se.*, **252**, 120-134, (1959)

[11] P. Hoekstra, T. Osterkamp, and W. Weeks, *Journal of Geophysical Research*, **70**, p5035-5041, (1965)

[12] P. Callaghan, R. Dykstra, C. Eccles, T. Haskell, and J. Seymour, *Cold regions science and technology*, **29**, p153-171, (1999)

[13] A. Gow, and B.Tucker, *CRREL Monogr.*, **91**, (1991)

[14] E. Lewis, and W. Weeks, *Symposium on Antarctic Ice and Water masses*, (1971)

[15] R. Paige, *US Navy Civil Engineering Laboratory Technical report*, **494**, p1-31, (1966)

[16] A. Gow, and B.Tucker, *Polar Oceanography*, **A**, p47-121, (1991)

[17] M. Jefferies, W. Weeks, R. Shaw, and K. Morris, *Journal of Glaciology*, **39**, p223-238, (1993)

[18] M. Jefferies, K. Schwartz, K. Morris, A. Veazy, H. Krouse, and S. Cushing, *Journal of Geophysical Research*, **100**, p10,905-10,914, (1995)

[19] C. Eccles, *Introduction to NMR imaging – Lecture notes*, p7-24, (1999)

[20] P. Callaghan, *Principals of Nuclear Magnetic Resonance Microscopy*, (1993)

[21] P. Callaghan, C. Eccles, and J. Seymour, *Review of Scientific Instruments*, **68**, p4263-4270, (1997)

[22] P. Edwards, Massey University – Chemistry, Personal communication

[23] Part of the Antarctica 1:250,000 Reconnaissance Series of Topographical Maps

[24] P. Callaghan, and C. Eccles, *Bulletin of Magnetic Resonance*, **18**, p62-64, (1996)

[25] P. Callaghan, C. Eccles, T. Haskell, P. Langhorne, and J. Seymore, *Journal of Magnetic Resonance*, **133**, p148-154, (1998)

[26] C. Lawson, and R. Hansen, "Solving Least Square Problems" SIAM, Philadelphia (1995)

[27] K. Whittall, and A, MacKay, *Journal of Magnetic Resonance*, **84**, p134, (1989)

[28] S. Provencher, *Computer Physics Communications*, **27**, p213, (1982)

[29] G. Borgia, R. Brown, and P. Fantazzini, *Journal of Magnetic Resonance*, **132**, p65-77, (1988)

[30] P. Morris, Nuclear Magnetic Resonance Imaging in Medicine and Biology, (1986)

[31] E. Weber, *Electromagnetic Fields – Theory and Applications*, **1**, (1950)

[32] D. Hoult, *Concepts in magnetic resonance*, **12(4)**, p173-187, (2000)

[33] E. Tanner, *Review of Scientific Instruments*, **36**, p1086, (1965)

[34] P. Lorrain, D. Corson, F. Lorrain, *Electromagnetic fields and waves*, **3**, p328-347, (1987)

[35] Matlab, a Numeric computation and Visualisation software package, The Math Works Incorporated, (1994)

[36] C. Zafiratos, *Physics*, p731-783, (1976)

[37] Data recorded in the 1997 Antarctic trip log book

[38] Oliver and Boyd, *Science Data Book*, **8**, p64-65, (1983)

[39] M. Ward, *Introduction to Electrical Engineering*, p184-186, (1978)

[40] R. Dykstra, Electrical Engineer, Personal communication

[41] D. Martonson, *Journal of Geophysical Research*, **95**, p11,641-11,654, (1990)

[42] C. Richardson, *Journal of Glaciology*, **17**, p507-519, (1976)

[43] RS Catalogue, p785 an p1073-1074, April 2000

[44] RS Data sheet number 240-0070 (1999) on N-type thermocouples

[45] Data booklet from Corning Incorporated, entitled MACOR

[46] N. Ashcroft, and N. Mermin, *Solid State Physics*, (1976)

[47] RS Data sheet number 232-3052 (1999) on Peltier effect heat pumps

[48] Robin Dykstra, Massey University – Physics, Personal communication

[49] D. Ginsberg, and M. Melchner, *Review of Scientific instruments*, **41**, p122, (1970)

[50] P. Wiles, *Brine Inclusions Within Sea Ice,* Summer research project report 1997-1998

[51] P. Basser, J. Mattiello, and D. LeBihan, *Biophysical Journal*, **66**, p259-267, (1994)

[52] P. Basser, J. Mattiello, and D. LeBihan, *Journal of Magnetic Resonance*, **103**, p247-254, (1994)

[53] PROSPA, Data analysis software developed by C. Eccles, Massey University, (2000)

[54] H. Trodahl, Victoria University – Physics, Data obtained from a probe in the ice sheet at the field camp (S 77^0 40.685' E 166^0 26.829') (1999)

[55] G. Frankenstein, and R. Garner, *Journal of Glaciology*, **6**, p943-944, (1967)

[56] G. Cox, and W. Weeks, *CRREL Report*, **82-30**, (1982)

Appendix 1

This contains the Matlab computer programs used for the B_1 and gradient field modelling for the ice-core probe, as described in sections 3.2.2 and 3.2.3.

The function hierarchy is as follows:

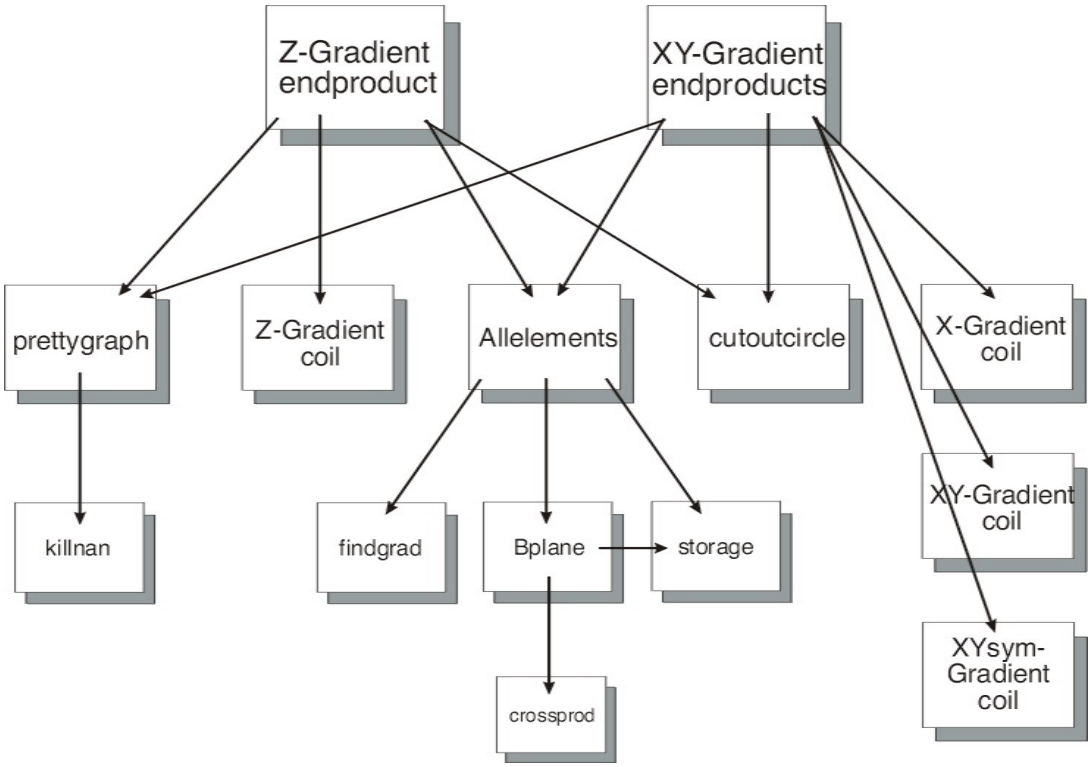

The actual programs are on the CD in page 120, in the folder called ‘Computer Programs’.

Appendix 2

This contains the Matlab computer programs used for the B_1 and gradient field modelling for the inside-out probe, as described in section 3.3.2.

The function hierarchy is as follows:

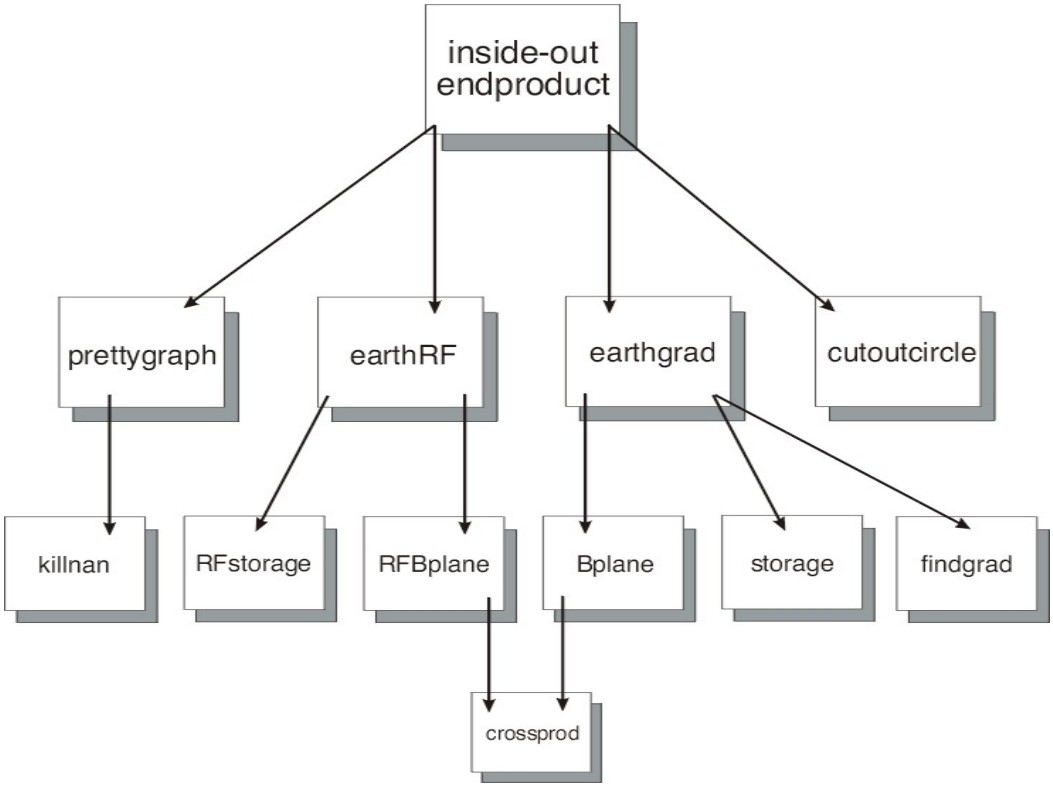

The actual programs are on the CD in page 120, in the folder called ‘Computer Programs’.

Appendix 3

This contains the Matlab and C computer programs used for the diffusion tensor analysis, as described in section 4.5.2.

The function hierarchy for the Matlab programs is as follows:

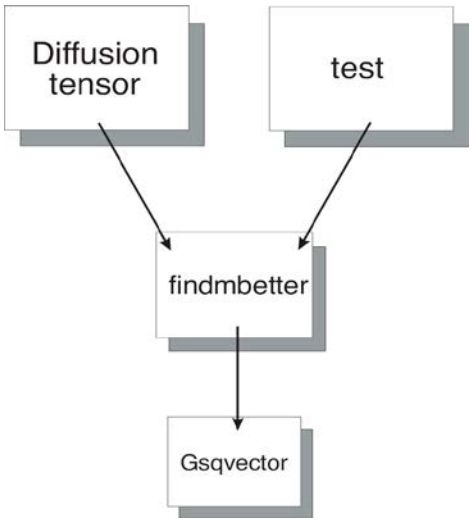

The function hierarchy for the C programs is as follows:

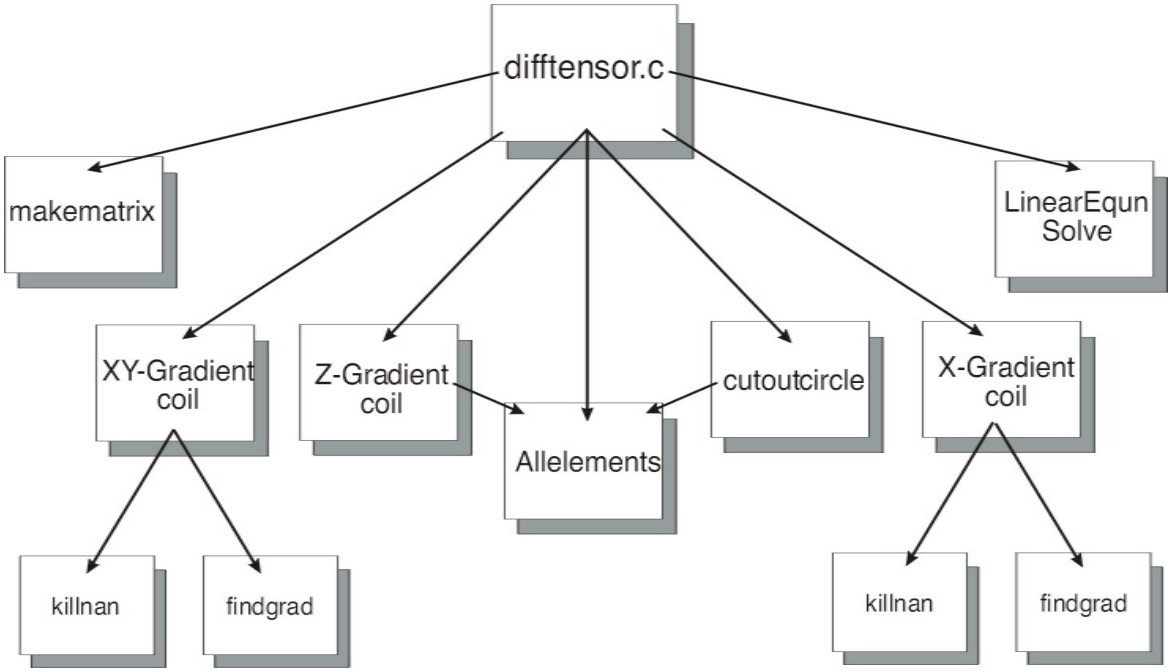

The actual programs are on the CD in page 120, in the folder called ‘Computer Programs’.

This CD contains a copy of my entire thesis, including some extra photos from the field trip in Antarctica. The computer programs that are described in the three appendices are found in the folder called ‘Computer Programs’.